Solar zenith angle-based calibration of Himawari-8 land surface temperature based on MODIS spatiotemporal characteristics

Yi Yu[1,2], Luigi J. Renzullo[1,3], Tim R. McVicar[4], Thomas G. Van Niel[4], Dejun Cai[4], Siyuan Tian[1,3], and Yichuan Ma[4,5]

[1]Fenner School of Environment & Society, The Australian National University, Canberra, ACT 2601, Australia
[2]CSIRO Agriculture and Food, Canberra, ACT 2601, Australia
[3]Bureau of Meteorology, Canberra, ACT 2600, Australia
[4]CSIRO Environment, Canberra, ACT 2601, Australia
[5]Hubei Key Laboratory of Quantitative Remote Sensing of Land and Atmosphere, School of Remote Sensing and Information Engineering, Wuhan University, Wuhan 430079, China

November 27, 2023

Abstract

The geostationary Himawari-8 satellite offers a unique opportunity to monitor sub-daily thermal dynamics over Asia and Oceania, and several operational land surface temperature (LST) retrieval algorithms have been developed for this purpose. However, studies have reported inconsistency between LST data obtained from geostationary and polar-orbiting platforms, particularly for daytime LST, which usually shows directional artefacts and can be strongly impacted by viewing and illumination geometries and shadowing effects. To overcome this challenge, Solar Zenith Angle (SZA) serves as an ideal physical variable to quantify systematic differences between platforms. Here we presented an SZA-based Calibration (SZAC) method to operationally calibrate the daytime component of a split-window retrieved Himawari-8 LST (referred to here as the baseline). SZAC describes the spatial heterogeneity and magnitude of diurnal LST discrepancies from different products. The SZAC coefficient was spatiotemporally optimised against highest-quality assured (error < 1 K) pixels from the MODerate-resolution Imaging Spectroradiometer (MODIS) daytime LST between 01/Jan/2016 and 31/Dec/2020. We evaluated the calibrated LST data, referred to as the Australian National University LST with SZAC ($\mathrm{ANU_{SZAC}}$), against MODIS LST and the Visible Infrared Imaging Radiometer Suite (VIIRS) LST, as well as *in-situ* LST from the OzFlux network. Two peer Himawari-8 LST products from Chiba University and the Copernicus Global Land Service were also collected for comparisons. The median daytime bias of $\mathrm{ANU_{SZAC}}$ LST against Terra-MODIS LST, Aqua-MODIS LST and VIIRS LST was 1.52 K, 0.98 K and -0.63 K, respectively, which demonstrated improved performance compared to baseline (5.37 K, 4.85 K and 3.02 K, respectively) and Chiba LST (3.71 K, 2.90 K and 1.07 K, respectively). All four Himawari-8 LST products showed comparable performance of unbiased root mean squared error (ubRMSE), ranging from 2.47 to 3.07 K, compared to LST from polar-orbiting platforms. In the evaluation against *in-situ* LST, the overall mean values of bias (ubRMSE) of baseline, Chiba, Copernicus and $\mathrm{ANU_{SZAC}}$ LST during daytime were 4.23 K (3.74 K), 2.16 K (3.62 K), 1.73 K (3.31 K) and 1.41 K (3.24 K), respectively, based on 171,289 hourly samples from 20 OzFlux sites across Australia between 01/Jan/2016 and 31/Dec/2020. In summary, the SZAC method offers a promising approach to enhance the reliability of geostationary LST retrievals by incorporating the spatiotemporal characteristics observed by accurate polar-orbiting LST data. Furthermore, it is possible to extend SZAC for LST estimation by using data acquired by geostationary satellites in other regions, e.g., Europe, Africa and Americas, as this could improve our understanding of the error characteristics of overlapped geostationary imageries, allowing for targeted refinements and calibrations to further enhance applicability.

Keywords

Land surface temperature; Geostationary; Himawari-8; Diurnal temperature cycle; Calibration; Solar zenith angle; MODIS; VIIRS

1. Introduction

Land surface temperature (LST) plays an important role in the Earth's surface energy budget, and is widely used in hydrology, meteorology and climatology (Li et al., 2013; Cao et al., 2019). LST undergoes rapid fluctuations over time, exhibiting distinct diurnal and seasonal patterns. The increasing quantity of LST observations obtained from various satellite missions has been important to comprehend the spatiotemporal dynamics of longwave radiation (Hu et al., 2020a). Such observations have been utilised in numerous scientific fields, including but not limited to agriculture (e.g., Ekinzog et al., 2022), drought monitoring (e.g., Zhang et al., 2017; Hu et al., 2020b), evapotranspiration estimation (e.g., Semmens et al., 2016) and ecology (e.g., Jiménez-Muñoz et al., 2013).

Remotely sensed LST can be routinely retrieved using data provided by polar-orbiting and geostationary satellite missions (Yu et al., 2009). Some well-known polar-orbiting platforms that provide LST retrievals include the Advanced Very High Resolution Radiometer (AVHRR; Kerr et al., 1992), the MODerate-resolution Imaging Spectroradiometer (MODIS; Wan and Li, 1997), the Advanced Spaceborne Thermal Emission and Reflection Radiometer (ASTER; Gillespie et al., 1998) and the Visible Infrared Imaging Radiometer Suite (VIIRS; Islam et al., 2016). They have a global coverage and relatively fine spatial resolution (e.g., 1 km for MODIS and VIIRS) but low temporal frequency, e.g., 4 times per day maximum for MODIS (less when considering cloud; Wilson and Jetz, 2016). As a comparison, geostationary platforms acquire LST over the complete diurnal cycle, with so-called 'new generation' geostationary instruments acquiring imagery at sub-hourly frequency (e.g., every 10 or 15 minutes), but with relatively coarse spatial resolution (usually equivalent to, or coarser than, 2 km). Examples of geostationary satellites include Himawari-8 (Bessho et al., 2016), the Geostationary Operational Environmental Satellite (GOES-R; Schmit et al., 2008), the Meteosat Second Generation (MSG; Schmetz et al., 2002), the Feng Yun meteorological satellites (FY-4A; Yang et al., 2017), the Indian National Satellite (INSAT-3D; Singh et al., 2016) and the Russian meteorological satellites (Elektro-L; Uspenskii et al., 2015). However, each geostationary satellite only observes a longitudinally defined hemisphere. To overcome this limitation, Freitas et al. (2013) fused data from multiple geostationary satellites to generate a global-coverage LST product with hourly frequency, known as the Copernicus Global Land Service (CGLS) project, but with a spatial resolution that is coarser than the individually retrieved geostationary LST products.

Over the past decades, there have been marked efforts to develop LST retrieval algorithms (Wan and Dozier, 1996; Sobrino et al., 2004; Yamamoto et al., 2018). Provided that land surface emissivity (LSE) is known *a priori* , the retrieval algorithms can be mainly classified by three categories, including (i) single-channel methods; (ii) multi-channel methods; and (iii) multi-angle methods (Li et al., 2013). Firstly, the single channel method, alternatively known as the model emissivity method (Hook et al., 1992), utilises radiance measured by the sensor in a single thermal infrared channel. An accurate estimation of LST through this approach requires a high-fidelity atmospheric transmittance/radiance code, extensive familiarity with the channel LSE, an accurate atmospheric profile, and an appropriate consideration of the topographic impacts (Sobrino et al., 2004). Secondly, due to the inherent challenges in either pre-establishing radiative transfer models or accurately estimating atmospheric profiles, linear split-window (SW) algorithms have been devised for the retrieval of sea surface temperature (SST; Barton et al., 1989; Niclòs et al., 2007). These algorithms leverage data from two adjacent channels centred at ~ 11 and 12 μ m. This linear approach serves as a typical multi-channel method and has been subsequently extended to LST studies, which was shown to be highly effective (e.g., Price, 1984; Coll et al., 1994; Wan and Dozier, 1996). Due to the SW algorithm's versatility and compatibility with almost all geostationary sensors, it is a popular choice for geostationary satellite products (Yu et al., 2007; Yu et al., 2009; Freitas et al., 2013; Li et al., 2020), with the exception of GOES 13/15 imagers, which have only one thermal band. Multi-channel methods can also employ nonlinear terms (Atitar and Sobrino, 2008) or utilise more than two adjacent channels (Yamamoto et al., 2018). Thirdly and finally, similar to the underlying principle of the multi-channel method, the multi-angle method relies on differential atmospheric absorption resulting from distinct path-lengths, which occurs when the same object is viewed from varying angles in a particular channel (Sobrino et al., 2004; Li et al., 2013). The outcomes of this method may surpass those of the SW algorithm, provided that the spectral and angular characteristics of LSE are well-determined (Li et al., 2013). However, a crucial concern in the multi-angle method is the angular dependence of LSE as the angular behaviour of natural surfaces (e.g., soils and rocks) is typically not well understood at the spatial scale of satellite observations (Sobrino and Jiménez-Muñoz, 2005). As a result, multi-angle methods are generally limited to homogeneous areas (e.g., sea surface or densely vegetated forests) under optimal atmospheric conditions, hence there has been limited use of multi-channel methods in most scenarios, particularly in heterogeneous environments.

Regardless of the specific retrieval algorithms utilised, studies have reported inconsistencies between LST obtained from geostationary and polar-orbiting missions. Trigo et al. (2021) demonstrated a difference of approximately ± 1 K between LST products from the AVHRR sensor onboard Metop polar-orbiting satellites and the Spinning Enhanced Visible and Infrared Imager (SEVIRI) onboard the MSG geostationary platform. Pérez-Planells et al. (2023) reported that Terra- and Aqua-MODIS LST products (i.e., MOD11 and MYD11, respectively) were around 2 K cooler than the LST datasets from the European Space Agency's Climate Change Initiative (ESA CCI) across all land cover classes. Similarly, Li et al. (2020) found MYD11 LST generally showed lower values than their SW algorithm-retrieved Himawari-8 LST over southeast China and Australia. Comparatively, their product displayed better agreement with MYD21 LST, a successor to MYD11 LST, which Hulley et al. (2017) developed using a Temperature and Emissivity Separation (TES) algorithm. The pronounced discrepancy between MYD11 and MYD21 LST was attributed to the differences in the emissivity calculation methods used in the retrievals (Hulley et al., 2017).

The discrepancy between polar-orbiting and geostationary LST can be particularly high during the daytime (Wang and Liang, 2009; Li et al., 2014; Li et al., 2021; Trigo et al., 2021; Yamamoto et al., 2022), due to variations in viewing and illumination angles (Ermida et al., 2017; Trigo et al., 2021). For example, daytime LST derived from polar-orbiting (i.e., MODIS) and geostationary (i.e., SEVIRI) platforms can have a difference of up to 12 K due to directional effects (Guillevic et al., 2013). This demonstrates that daytime geostationary LST measurements require further recalibration to better align with ground observations. Researchers have directed their investigations towards the conspicuous directional characteristics of LST and have developed correction and harmonisation methodologies, in which the solar zenith angle (SZA) plays a pivotal role (Vinnikov et al., 2012; Ermida et al., 2017; Ermida et al., 2018; Jiang et al., 2021).

SZA represents the angle formed between the Sun's rays and the vertical direction. It is important in various meteorological and climatological calculations, including the determination of radiant temperature (Di Napoli et al., 2019; Vanos et al., 2021), and in the computation of thermal and heat indices such as the Universal Thermal Climate Index (UTCI; Di Napoli et al., 2021). SZA has also found extensive utility in rectifying and harmonising discrepancies in daytime LST acquired from different platforms. Specifically, Vinnikov et al. (2012) introduced an LST anisotropy model that incorporates an SZA-based kernel, representing the influence of directional heterogeneity on observed LST, in conjunction with isotropic and emissivity kernels, which showed improved agreements with ground-based observations. Ermida et al. (2017) calibrated this model against satellite-observed LST acquired at varying viewing angles, and derived spatially varying coefficients for the SZA-based kernel, which encapsulated the characteristics of terrain and vegetation cover. The application of this model ameliorated disparities in LST observed by different satellites, as well as between satellite observations and ground measurements, offering utility to harmonise LST products (Vinnikov et al., 2012; Ermida et al., 2017). Furthermore, Duan et al. (2014) used SZA as a predictor to normalise Terra-MODIS LST during daylight hours, ensuring consistency with local solar time and facilitating the generation of temporally consistent LST products. To normalise the temporal effects of MODIS LST, Zhao et al. (2019) estimated cumulative incident solar radiation by incorporating the cosine value of the SZA, while also considering atmospheric transmittance and path length. Their normalised LST showed reduced uncertainty against MSG-SEVIRI LST. Jiang et al. (2021) compared the performances of 11 kernel-driven models in simulating daytime urban thermal radiation directionality (UTRD), where SZA was used to assess the impact of city latitude and to simulate parametric kernels for UTRD. They found that dual-kernel models achieved a best performance against forward-modelling and satellite data. Wang et al. (2023) also employed the SZA as a key parameter to establish an angular normalisation model to convert MODIS off-nadir LST values to nadir values, which yielded better consistencies with Sentinel-3A nadir LST. As summarised in Table 1, these diverse applications of SZA underscore its effectiveness in rectifying LST discrepancies arising from multiple observational platforms.

Reference	Satellite platforms	Summary of key objective(s)	Usage of SZA	Key results	Potential limitations
Vinnikov et al. (2012)	GOES-EAST and GOES-WEST	Proposed a statistical model for evaluation and adjustment of angularity of LST.	SZA was used to simulate a solar kernel that represents directional inhomogeneity of LST.	Evaluations against observations from 5 SURFRAD stations showed bias within ±0.5 K and RMSE of 1.2-1.4 K.	All 5 SURFRAD stations are located within limited range of VZA between 43 ° and 66 °. The study also lacked observations of SZA ¡ 10.75 °.
Duan et al. (2014)	Terra-MODIS and MSG-SEVIRI	Proposed a temporal normalisation method of daytime LST.	SZA was used as a regression predictor to estimate the slope of LST versus local solar time.	Difference between Terra-MODIS and MSG-SEVIRI LST reduced from 1.5 K to 0.5 K after normalisation.	The regression was established using data from only 4 months (January, April, July, and October) in 2010. No ground-based evaluations were performed.
Ermida et al. (2017)	Terra-, Aqua-MODIS and MSG-SEVIRI	Calibrated Vinnikov et al. (2012) model with LST acquired at different view angles to characterise LST anisotropy.	Same with Vinnikov et al. (2012).	Cross-validation showed the RMSE between SEVIRI and MODIS daytime (nighttime) reduced from 3.5 K (1.5 K) to 2.3 K (1.3 K). Evaluations against in-situ daytime LST showed a reduced RMSE from 4.6 K (2.0 K) to 3.8 K (1.9 K) for MODIS (SEVIRI).	Seasonal variations of vegetation-shaded fraction may impact the values of SZA-based kernel but was not considered. There was no observation of azimuth angles from north but was expected to have minor impacts as SZA-based kernel is symmetric to relative azimuth angles.
Zhao et al. (2019)	Terra-MODIS and MSG-SEVIRI	Normalised the temporal effects of MODIS LST using a random forest regression.	SZA was used to estimate the cumulative incident solar radiation, with the consideration of atmospheric transmittance and path length.	Normalised LST showed reduced bias (RMSE) of 1.66 K (1.23 K) against MSG-SEVIRI LST compared to the original MODIS LST.	The estimation of solar radiation factor may be affected by the simplification of spatial variability of atmospheric transmittance. No ground-based evaluations were performed.
Jiang et al. (2021)	Quasi-simultaneous multi-angle MODIS LST produced by Hu et al. (2016)	Simulated daytime urban thermal radiation directionality (UTRD) using 11 kernel-driven models.	SZA was used to assess the impact of city latitude and to simulate parametric kernels for UTRD.	Dual-kernel models achieved a best performance of RMSE against forward-modelling and satellite data, being 0.49 K and 0.77 K, respectively.	All models used herein were originally developed for vegetated surfaces, without considerations of urban surface types and environmental conditions. No ground-based evaluations were performed.
Wang et al. (2023)	Terra-, Aqua-MODIS and Sentinel-3A	Developed an angular normalisation method for converting global	SZA was used to estimate sensor-object-solar geometry and kernel functions.	Normalised daytime LST showed bias (RMSE) of 0 K (1.57 K) against in-situ LST, and bias (RMSE) of -1.2 K (2.26 K) against	This study only focused on the vegetated surfaces. The cross-platform validation (i.e., against Sentinel-3A) was only

Based on the summary of previous studies presented in Table 1, it is evident that certain limitations exist within the body of research, such as a lack of cross-platform validation, absence of ground-based evaluations, and focus on a limited range of land cover types. These factors collectively suggest that the full potential of SZA has not been explored to maximise the consistency of LST across multiple platforms. Additionally, to enhance the synchronisation of daytime and nighttime observations, it is imperative to gain a comprehensive understanding of the diurnal patterns of LST (Sharifnezhadazizi et al., 2019; Azarderakhsh et al., 2020). While some studies have employed multi-parameter models to simulate the diurnal cycle patterns of LST using sparsely sampled observations from polar-orbiting satellites (Duan et al., 2012; Hu et al., 2020a; Lu and Zhou, 2021), there have been minimal efforts to quantify the diurnal characteristics of error performance of geostationary LST products (Vinnikov et al., 2008; Holmes et al., 2015). Hence, there is a need to address this scientific gap and to investigate the diurnal error dynamics of geostationary LST products, thus further improving accuracy of geostationary LST products.

Accordingly, our objectives were to: (i) calibrate the daytime component of an SW algorithm-retrieved Himawari-8 LST product using an SZA-based calibration approach that incorporates the spatiotemporal characteristics of polar-orbiting MODIS LST; (ii) evaluate the diurnal error characteristics of calibrated LST and collected Himawari-8 LST peer products against *in-situ* LST across different seasons; and (iii) compare the spatial pattern and derive pixelwise metrics of calibrated LST and Himawari-8 LST peer products against VIIRS LST.

2. Data and study area

The remotely sensed data and ground measurements used herein are itemised in Table 2. The Himawari-8 brightness temperature (T_B) was used as input, along with the emissivity, to retrieve LST through an SW algorithm. Two peer Himawari-8 LST products (i.e., (i) Chiba and (ii) Copernicus) were used for evaluations against *in-situ* LST derived from ground-based longwave radiation and polar-orbiting LST products. The MOD11A1 and MYD11A1 LST products (Collection 6) were employed for pixelwise calibration of SW retrieved Himawari-8 LST and assessment of model performance. The VNP21A1D LST acquired by the VIIRS mission was used for spatiotemporal evaluations of multi-sourced Himawari-8 LST through pixelwise metrics. The longwave radiation obtained from the OzFlux network was used to derive *in-situ* LST for ground-based evaluation. The MOD13A1 enhanced vegetation index (EVI), MCD15A2H leaf area index (LAI) and MCD43A3 albedo products (all Collection 6) were used for evaluations of the spatial patterns of the calibration coefficient of Himawari-8 LST.

Categories	Datasets	Spatial resolution	Temporal frequency	Period	References
Input	Himawari-8 TB	2 km	10-min	01/Jan/2016 – 31/Dec/2020	Bureau of Meteorology (2021)
	UW baseline fit emissivity	5 km	Long-term monthly	01/Jan/2003 – 31/Dec/2016	Seemann et al. (2008)
Himawari-8 LST products	Chiba	2 km	Hourly	01/Jan/2016 – 31/Dec/2020	Yamamoto et al. (2018)
	Copernicus	4.5 km	Hourly	01/Jan/2016 – 31/Dec/2020	Freitas et al. (2013)
Polar-orbiting LST products	MOD11A1 and MYD11A1	1 km	Daily	01/Jan/2016 – 31/Dec/2020	Wan (2014)
	VNP21A1D	1 km	Daily	01/Jan/2016 – 31/Dec/2020	Islam et al. (2016)
Ground measurements	OzFlux Longwave radiation	Point	30-min	01/Jan/2016 – 31/Dec/2020	Beringer et al. (2016)
Surface reflectance products	MOD13A1	500 m	16-day	01/Jan/2016 – 31/Dec/2020	Huete et al. (2002)
	MCD15A2H	500 m	8-day	01/Jan/2016 – 31/Dec/2020	Myneni et al. (2002)
	MCD43A3	500 m	Daily	01/Jan/2016 – 31/Dec/2020	Schaaf et al. (2002)

Table 2: Summary of data used herein. The spatial resolution of OzFlux measurements is not strictly a point, rather an aggregation of local area fluxes in the vicinity of the flux tower. This means the values of flux towers are representative of a specific region, while the area depends on localised settings in the vicinity of each flux tower station. The contribution from flux tower can range from meters to kilometres and can be considered comparable to remotely sensed data (Chu et al., 2021; Qin et al., 2022). UW denotes University of Wisconsin.

2.1 UW baseline fit emissivity

The University of Wisconsin (UW) Baseline Fit Emissivity Database is a global database of infrared land surface emissivity derived using an operational MODIS product (MOD11) (Seemann et al., 2008). The database fills in the spectral gaps of MOD11 and provides emissivity at 10 wavelengths, ranging from 3.6 to 14.3 μ m, with 0.05 degree spatial resolution (~ 5 km at the equator). We acquired the emissivity at 10.8 and 12.1 μ m wavelengths (selected to match the wavelengths used in baseline LST retrieval, see Section 3.1) for each month over 2003-2016 and calculated monthly values by averaging them over the 14-year period.

2.2 Himawari-8 LST

The Himawari-8 geostationary satellite was launched by the Japan Meteorological Agency in October 2014 and has been operational since July 2015 (Bessho et al., 2016). It carries the Advanced Himawari Imager (AHI) with capabilities comparable to the Advanced Baseline Imager (ABI) on board GOES-R (Schmit et al., 2005; Schmit et al., 2008). Himawari-8 is located above the equator at longitude of 140.7 °E and observes east/southeast Asia and Oceania. The AHI has 16 observation bands, including 3 visible bands at wavelengths centred at 0.47, 0.51 and 0.64μ m (B1 – B3), 3 near-infrared (NIR) bands at wavelengths centred at 0.86, 1.61, and 2.25 μ m (B4 – B6), and 10 infrared (IR) bands with central wavelengths ranging from 3.9

to 13.3 μ m (B7 – B16). The resolution of observation bands ranges from 0.5 to 2 km at the sub-satellite point. The observation cycle occurs every 10 min for the full disk. Himawari-8 data are available through the collection of Australian Bureau of Meteorology Satellite Observations (Bureau of Meteorology, 2021).

2.1.1 Chiba LST

The LST retrieval from Chiba University, Japan, uses a three-band algorithm developed by Yamamoto et al. (2018), herein denoted as the YAM algorithm, which employs several nonlinear terms to improve the LST estimation accuracy over a wide temperature range (Yamamoto et al., 2022). It requires 3 bands of Himawari-8 T_B, 3 bands of LSEs and precipitable water (PW) as inputs. The wavelengths of 3 required TIR bands (T_{B13}, T_{B14} and T_{B15}) are 10.4, 11.2 and 12.4 μ m, respectively. LSEs (ε_{B13}, ε_{B14}, and ε_{B15}) are estimated using an NDVI threshold approach developed by Yamamoto and Ishikawa (2018), while PW are total column water vapour values from the European Centre for Medium-Range Weather Forecasts (ECMWF) ReAnalysis version 5 (ERA5; Hersbach et al., 2020). We collected Chiba LST for 01/Jan/2016 – 31/Dec/2020 with a spatial resolution of 2 km and an hourly frequency (i.e., on the hour mark). The Chiba LST data are distributed by the Center for Environmental Remote Sensing (CEReS), Chiba University, Japan, and are freely available at ftp://modis.cr.chiba-u.ac.jp/yyamamoto/AHILST/v0/ (Accessed 05/Oct/2023).

2.1.2 Copernicus LST

The Copernicus LST dataset is a global-coverage LST product using input data from various geostationary satellites, including MSG, GOES and Himawari-8 (Freitas et al., 2013). It employs a generalised SW algorithm to accommodate different characteristics from each geostationary satellite imager, which utilises two adjacent channels within the thermal infrared domain to retrieve LST. We collected Copernicus LST covering 01/Jan/2016 – 31/Dec/2020 with a spatial resolution of ˜ 4.5 km at an hourly frequency (i.e., on the hour mark). We acquired the Copernicus LST data from the CGLS project (https://land.copernicus.eu/global/products/lst; accessed 05/Oct/2023).

2.3 MODIS LST

MODIS is aboard the Terra and Aqua satellites launched by the National Aeronautics and Space Administration (NASA) in 1999 and 2002, respectively (Justice et al., 1998). These satellites are in sun-synchronous orbits, where Terra has a nominal descending node at approximately 10:30 local solar time, while Aqua has an ascending node at approximately 13:30 local solar time. The MODIS LST is retrieved through a generalised SW algorithm with a reported accuracy of approximately 2.0 K (Wan, 2014). We collected the MOD11A1 (Terra) and MYD11A1 (Aqua) datasets (both Collection 6) covering 01/Jan/2016 – 31/Dec/2020 with a spatial resolution of 1 km and daily temporal frequency. These data were acquired from the NASA Earthdata Search platform (https://search.earthdata.nasa.gov/search; accessed 05/Oct/2023).

2.4 VIIRS LST

VIIRS is a scanning radiometer on the Suomi National Polar-orbiting Partnership (Suomi-NPP) satellite launched by NASA in October 2011 (Islam et al., 2016). It operates in a sun-synchronous orbit, with an equatorial crossing time at the ascending node of approximately 13:30 local solar time. The VIIRS LST & Emissivity (LST&E) product (VNP21) is retrieved using a physics-based Temperature and Emissivity Separation (TES) algorithm, providing the simultaneous retrieval of LST and emissivity from the thermal infrared bands. We obtained the VNP21A1D dataset (Collection 1) for 01/Jan/2016 to 31/Dec/2020 with a spatial resolution of 1 km and daily temporal frequency. The data were acquired from the NASA Earthdata Search platform (https://search.earthdata.nasa.gov/search; accessed 05/Oct/2023).

2.5 Study area and *in-situ* measurements

The observation area of Himawari-8 covers the longitude of 85 °E – 155 °W and latitude of 60 °S – 60 °N (Fig. 1a). We chose a subset (112 °E – 154 °E and 45 °S – 10 °S) covering the Australian continent as the study area. Fig. 1 (b) shows the land cover of Australia (Lymburner et al., 2015) and locations of 20 flux tower sites from the OzFlux network (Beringer et al., 2016). Table 3 provides the details of the 20 flux tower sites.

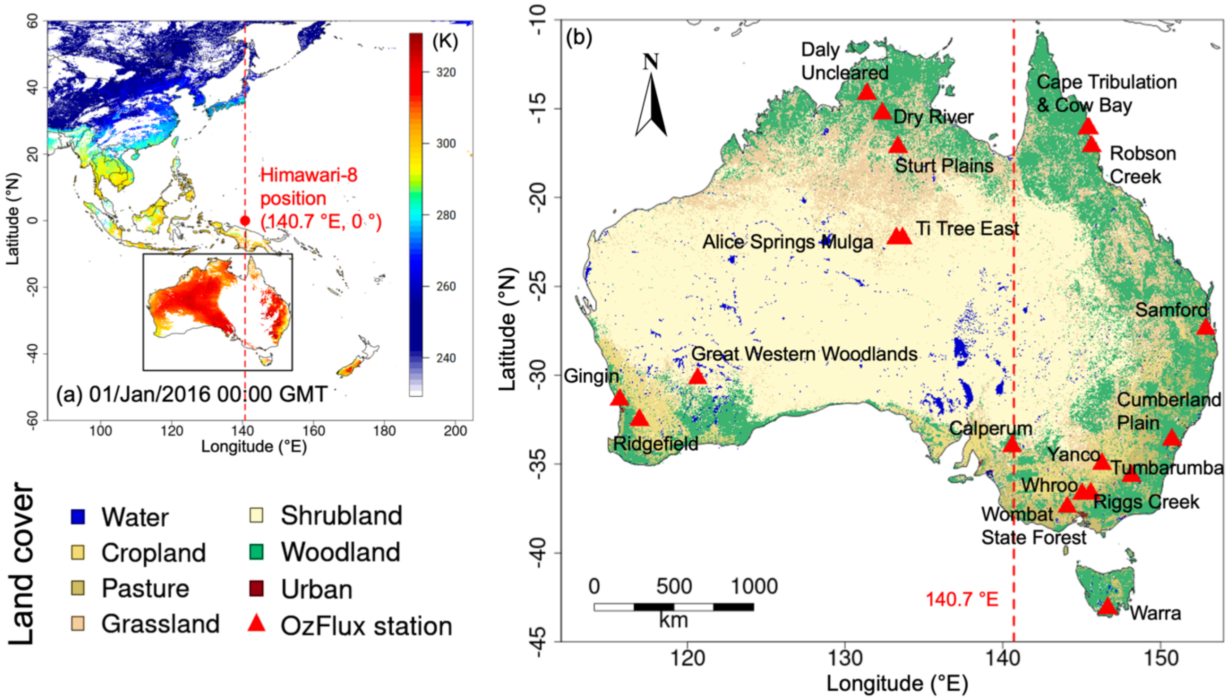

Figure 1: (a) LST of the full-disk Himawari-8 observation area on 01/Jan/2016 00:00 GMT with clouds and oceans masked out; and (b) the land cover map of Australia (Lymburner et al., 2015) and the distribution of 20 OzFlux sites. The study site is provided by the black rectangle bounding Australia in (a).

Site name	Latitude (°N)	Longitude (°E)	Land cover	Annual rainfall (mm/year)	Standard time zone
Alice Springs Mulga	-22.28	133.25	Semi-arid mulga	306	ACST
Calperum	-34.0	140.59	Recovering woodland	240	ACST
Cape Tribulation	-16.11	145.38	Tropical rainforest	5700	AEST
Cow Bay	-16.1	145.45	Complex mesophyll vine forest	4000	AEST
Cumberland Plain	-33.62	150.72	Dry sclerophyll	800	AEST
Daly Uncleared	-14.16	131.39	Woodland savanna	1170	ACST
Dry River	-15.26	132.37	Open forest savanna	895	ACST
Gingin	-31.38	115.71	Coastal health woodland	641	AWST
Great Western Woodlands	-30.19	120.65	Temperate woodland, shrubland and mallee	240	AWST
Ridgefield	-32.51	116.97	Dryland agriculture	446	AWST
Riggs Creek	-36.65	145.58	Dryland agriculture	650	AEST
Robson Creek	-17.12	145.63	Complex mesophyll vine forest	2236	AEST
Samford	-27.39	152.88	Improved pasture	1102	AEST
Sturt Plains	-17.15	133.35	Low lying plain dominated by grass	640	ACST
Ti Tree East	-22.29	133.64	Grassy mulga woodland and savanna	305	ACST
Tumbarumba	-35.66	148.15	Wet temperate sclerophyll eucalypt	1000	AEST
Warra	-43.1	146.65	Eucalyptus obliqua forest	1700	AEST
Whroo	-36.67	145.03	Box woodland	558	AEST
Wombat State Forest	-37.42	144.09	Dry sclerophyll eucalypt forest	650	AEST
Yanco	-34.99	146.29	Various soils and cropland	465	AEST

Table 3: Summary of 20 sites from the OzFlux network. The land cover and annual rainfall information are from https://ozflux.org.au/ (Accessed 05/Oct/2023). The following abbreviations are used in the 'standard time zone' column: ACST (Australian Central Standard Time; GMT+9.5); AEST (Australian Eastern Standard Time; GMT+10); AWST (Australian Western Standard Time; GMT+8).

We estimated the *in-situ* LST using the ground-level upwelling and downwelling longwave radiation (Level 3) data observed at the OzFlux stations. By manipulating the traditional equation governing longwave radiation balance (Allen et al., 1998; Trebs et al., 2021) an approximation of the *in-situ* LST was derived as:

$$LST_{in-situ} = \left(\frac{F^{\uparrow} - (1-\varepsilon_{\mathrm{b}})F^{\downarrow}}{\sigma\varepsilon_{\mathrm{b}}}\right)^{1/4} \# (1)$$

where $LST_{in-situ}$ is *in-situ* LST (K), $F^{\uparrow}$ is the upwelling longwave radiation (W/m^2), $F^{\downarrow}$ is the downwelling longwave radiation (W/m^2), ε_b is the surface broadband emissivity (unitless), and σ is the Boltzmann constant (5.67×10^{-8} W m^{-2}K^{-4}).

2.6 MODIS surface reflectance-derived indices

We collected three MODIS surface reflectance-derived products, including the 500 m resolution 16-day MOD13A1 EVI (Huete et al., 2002), the 500 m resolution 8-day MCD15A2H LAI (Myneni et al., 2002) and the 500 m resolution daily MCD43A3 albedo (Schaaf et al., 2002) products (all Collection 6), covering 01/Jan/2016 – 31/Dec/2020. We calculated the pixelwise median values of each product for the Australian continent throughout the 5-year period. These data were acquired from the NASA Earthdata Search platform (https://search.earthdata.nasa.gov/search; accessed 05/Oct/2023).

3. Methodology

Fig. 2 presents the experimental design employed herein, comprising three key steps. Firstly, we retrieved the baseline LST through an SW algorithm (Yu et al., 2012) using Himawari-8 T_B and emissivity from the UW Baseline Fit Emissivity Database (Section 3.1 Baseline algorithm). Secondly, we conducted the Solar Zenith Angle-based Calibration (SZAC) using all available scenes of Terra- and Aqua-MODIS daytime LST for the Australian continent between 01/Jan/2016 and 31/Dec/2020. To ensure the highest data quality, we applied quality assurance (QA) flags to select MODIS LST pixels with an expected retrieval error of less than 1.0 K (Wan, 2013). We selected MODIS QA flags with numeric values of 0, 5, 17 and 21. By using the time series of both MODIS best-quality LST and baseline LST, we derived a spatial distribution of optimised coefficient of SZAC for Australia, which allowed us to calibrate the daytime component of baseline LST. This step is denoted as Section 3.2 Solar Zenith Angle-based Calibration (SZAC). Thirdly and finally, we evaluated the performance of calibrated LST, referred to as the Australian National University LST with SZAC (ANU_{SZAC} LST), against *in-situ* LST and all available pixels from MODIS and VIIRS LST data between 01/Jan/2016 and 31/Dec/2020, while utilising the performances of three Himawari-8 LST datasets (baseline, Chiba, and Copernicus) as comparisons (Section 3.3 Multi-platform evaluation).

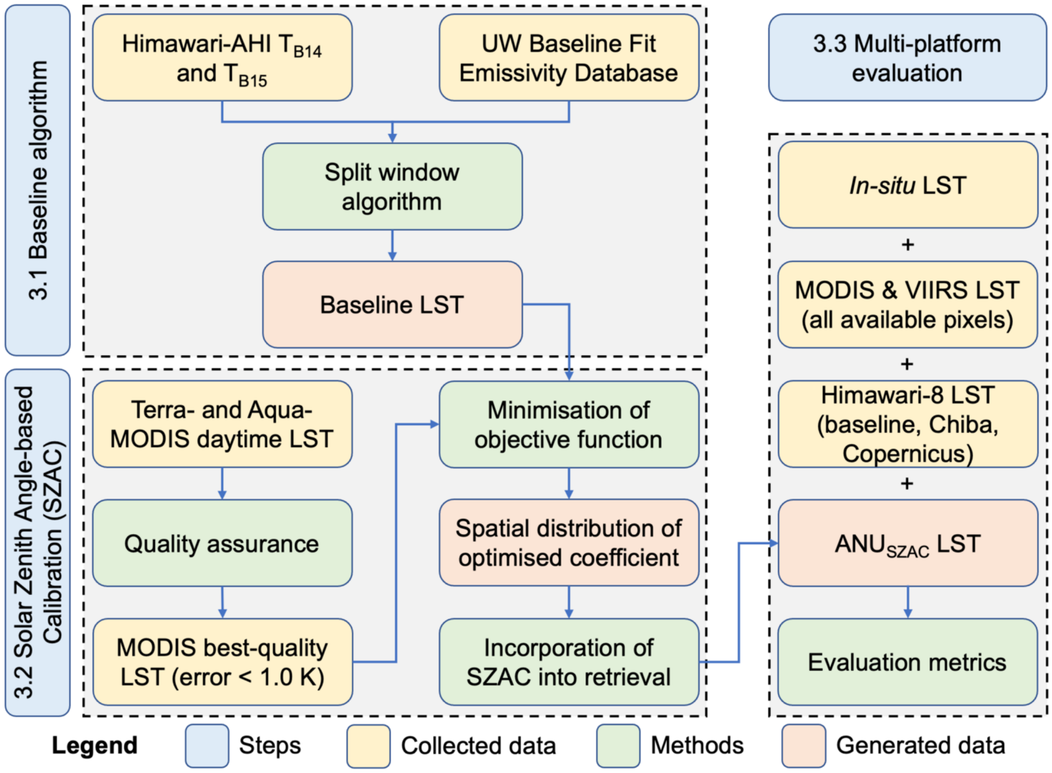

Figure 2: Experimental design for this research. The SZAC process was conducted using the time series of every 2 × 2 km pixel throughout the Australian continent.

3.1 Baseline algorithm

We employed an SW algorithm (Yu et al., 2009) with coefficients from Yu et al. (2012) to retrieve LST, referred to as the baseline Himawari-8 LST retrieval herein, taking the following forms:

$$LST_{\text{day}} = 30.022546 + 1.018212 T_{11} + 1.263787 (T_{11} - T_{12}) - 39.387858\varepsilon$$
$$+0.609744 (T_{11} - T_{12}) (\sec\theta_{\text{view}} - 1) \#(2)$$

$$LST_{\text{night}} = 36.160667 + 1.012895 T_{11} + 1.022203 (T_{11} - T_{12}) - 38.909505\varepsilon$$
$$+0.669541 (T_{11} - T_{12}) (\sec\theta_{\text{view}} - 1) \#(3)$$

where LST_{day} and LST_{night} represent LST (K) during daytime and nighttime, respectively, which are defined as when SZA (°) is lower/higher than 85 °; T_{11} and T_{12} are T_B (K) at ~ 11 and ~ 12 μ m wavelength (i.e., Himawari-8 bands 14 and 15, respectively); ε is broadband emissivity (unitless); θ_{view} is the viewing zenith angle (VZA; °) of Himawari-8. The Yu et al. (2012) LST coefficients were originally developed for GOES-ABI and with Himawari-AHI having essentially identical spectral and radiometric characteristics at bands 14 and 15 (Schmit et al., 2008; Bessho et al., 2016) they were applied to Himawari-8 data.

3.2 Solar Zenith Angle-based Calibration (SZAC)

SZA has underscored its effectiveness in rectifying LST discrepancies arising from multiple observational platforms (see Table 1). SZA can serve as a proxy for the amount of solar energy that reaches the ground surface, and its consequent impact on LST can be analysed through statistical approaches (Cresswell et al., 1999). Theoretically, SZA should remain consistent across all platforms, serving as an ideal bridging parameter to quantify systematic differences between them. This is preferable to VZA, as the scanning strategies of polar-orbiting and geostationary platforms are fundamentally distinct. This facilitates a spatially coherent approach for achieving the necessary spatiotemporal calibration.

Here we introduce the concept of SZAC to calibrate the daytime component of Himawari-8 baseline LST using an empirical function of SZA on a pixelwise basis. In SZAC, a fundamental assumption is that the diurnal variations of clear-sky LST are continuous and can be simulated using discrete observations (Duan et al., 2012; Lu and Zhou, 2021). SZAC is a calibration factor (K) to be subtracted from daytime baseline LST, which involves the application of a logarithm on the cosine of SZA and is given as:

$$SZAC(x_i, y_i, t) = Coeff(x_i, y_i) \times log\left(\cos\theta_{\text{solar}}(x_i, y_i, t) + 1\right) \# (4)$$

$$\cos\theta_{\text{solar}}\left(x_i, y_i, t\right) = \sin\Phi\left(x_i, y_i\right)\sin\delta\left(x_i, y_i, t\right) + \cos\Phi\left(x_i, y_i\right)\cos\delta\left(x_i, y_i, t\right)\cos h\left(x_i, y_i, t\right) \# (5)$$

where $(x_i,\ y_i)$ is the geolocation of a given pixel i; t is the given time; SZAC is the calibration factor (K); Coeff is an empirical coefficient (K) to be optimised; θ_{solar} is SZA (°); Φ is the latitude; δ is the current declination of Sun; and h is the hour angle in local solar time.

SZAC can be conceptualised as the magnitude of LST disparities between different platforms during the heating period of surface. The cosine of SZA represents the diurnal variations of shadowed area in relation to the total surface area, serving as an effective measure of the solar radiance (not considering topographic adjustment) reaching the Earth's surface (Yeom et al., 2012), with the application of a logarithmic filter to attenuate potential overfitting of regression. Additionally, this filtering ensures the curve approaches near-zero values during the day-night transition and not adversely affect nighttime LST retrievals. We employed LST from both Terra- and Aqua-MODIS as reference for optimising the coefficient of SZAC. Fig. 3 (a) provides a scatterplot example illustrating the baseline-MODIS difference plotted against SZA at the Wombat State Forest site during 1/Jan/2016-31/Dec/2020. The majority of samples cluster within the range of 20 - 70 ° SZA, which corresponds to the MODIS overpass times of approximately 10:30 am and 1:30 pm local solar time for Terra and Aqua, respectively. Fig. 3 (b) shows the temporal variation of SZAC throughout a day. SZAC attains its maximum value when SZA is lowest (i.e., around midday) and reaches its minimum value when SZA is approximately 85 ° (i.e., sunrise or sunset). This ensures that SZAC has minimal impact on the day-night transition and does not affect the nighttime LST retrievals.

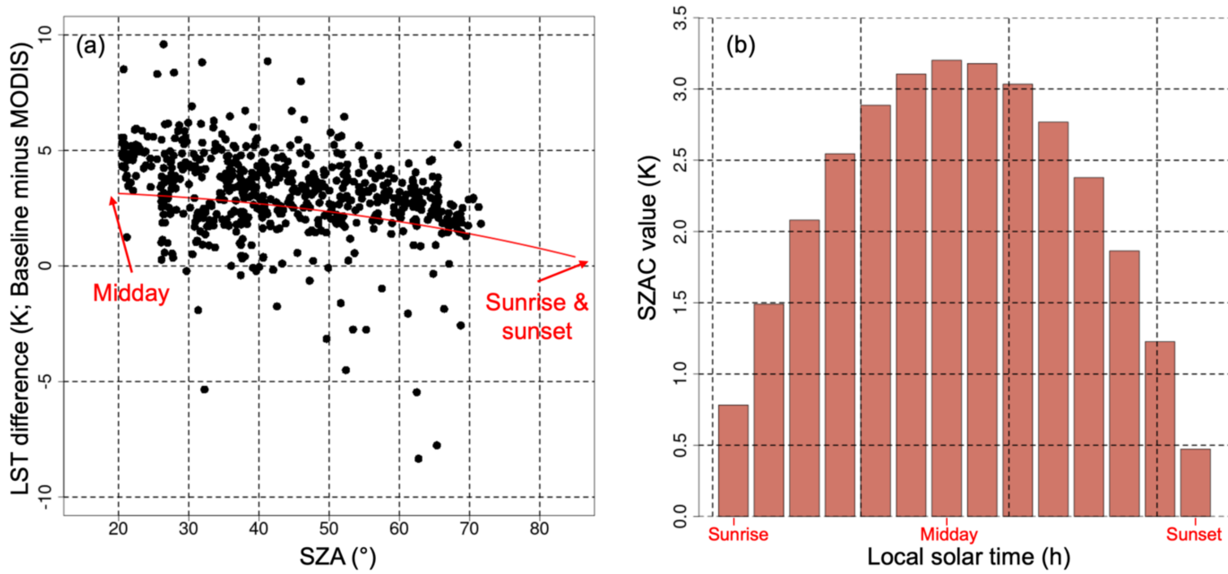

Figure 3: (a) Schematic of SZAC at the Wombat State Forest site and; (b) an example to show the temporal variation (using a bin size of 60 minutes) of SZAC during daytime on 02/Jan/2016. The location of Wombat State Forest is shown on Fig. 1. (b) with additional details provided in Table 3.

We employed the Brent (2013) local optimisation approach to determine the coefficient of SZAC for each matched cloud-free baseline-MODIS LST time series during 1/Jan/2016-31/Dec/2020 on a pixelwise basis. This minimised the difference between all coincident baseline Himawari LST and MODIS LST observations over the full 5-year period on a pixelwise basis. The objective function was the root mean square error (RMSE) between the baseline LST and MODIS LST. Then the daytime baseline LST for each pixel was calibrated using the single coefficient along with the temporal variations of SZA, which was denoted as the calibrated LST (i.e., $\mathrm{ANU_{SZAC}}$):

$$LST_{day,ZAC}(x_i, y_i, t) = LST_{day}(x_i, y_i, t) - SZAC(x_i, y_i, t)\#\,(6)$$

where $LST_{day,ZAC}$ is the calibrated daytime LST and LST_{day} is the baseline daytime LST.

3.3 Multi-platform evaluation

3.3.1 Cross-satellite matching strategy

Geostationary and polar-orbiting satellites have different surface scanning strategies. The Terra, Aqua and Suomi-NPP satellites do not have a constant overpass time, e.g., the data acquisition time of Terra ranges from 10:00 to 12:10 local solar time (Hu et al., 2014). To standardise the acquisition times of MODIS and VIIRS LST records and make them comparable with those of Himawari-8 LST, we converted the MODIS and VIIRS 'view time' layer, which is expressed in local solar time, to the GMT format, which is given as:

$$T_{polar,GMT}(x_i, y_i, t) = T_{polar,solar}(x_i, y_i, t) - Lon/15\#\,(7)$$

where $T_{polar,GMT}$ is the MODIS or VIIRS view time in GMT format, $T_{polar,solar}$ is the MODIS or VIIRS view time in local solar time, and Lon is the longitude in decimal of a given pixel. Then we utilised a one-hour temporal window (i.e., ± 30 minutes) to match Himawari-8 time (GMT) and MODIS time (GMT) on a pixelwise basis:

$$T_{H8,GMT}(x_i, y_i, t) - 30\ min \leq T_{polar,GMT}(x_i, y_i, t) \leq T_{H8,GMT}(x_i, y_i, t) + 30\ min\# \ (8)$$

where $T_{H8,GMT}$ is the time stamp of Himawari-8 in GMT format. This matching strategy allowed us to derive comparable LST records from Himawari-8 and polar-orbiting satellites (MODIS or VIIRS).

3.3.2 *In-situ* matching strategy

We employed the *in-situ* LST derived from OzFlux longwave radiation to evaluate Himawari-8 LST. Flux towers from the OzFlux network (see Fig. 1 (b) for locations and Table 3 for additional information) measure longwave radiation at half-hour intervals. We also implemented a one-hour temporal window (i.e., ± 30 minutes) strategy, similar to Eq. 8, to match Himawari-8 time (GMT) and *in-situ* time (converted to GMT). We calculated the mean in cases where two *in-situ* records are present within the hour. By adopting this approach, direct comparisons between Himawari-8 LST observations and corresponding ground-level measurements were made, disregarding individual time zones of flux towers.

3.3.3 Evaluation metrics

We utilised bias and unbiased root mean square error (ubRMSE) to evaluate the performance of Himawari-8 LST data against the corresponding reference LST:

$$Bias = \frac{\sum(LST_{H8} - LST_{ref})}{N}\# \ (9)$$

$$ubRMSE = \sqrt{\frac{\sum((LST_{H8} - \mu(LST_{H8})) - (LST_{ref} - \mu(LST_{ref})))^2}{N}}\# \ (10)$$

where LST_{H8} is the time series of Himawari-8 (i.e., baseline, Chiba, Copernicus or $\mathrm{ANU_{SZAC}}$) LST; LST_{ref} is the time series of reference (i.e., *in-situ*, MODIS or VIIRS) LST; N is the number of individual observations in each reference time series.

4. Results

4.1 Assessment of MODIS-based SZAC's performance

Fig. 4 (a) shows the spatial distribution of SZAC coefficient for the Australian continent. Lower values of the coefficient (less than 4 K) were observed over the eastern edge, whereas higher values (exceeding 8 K) were concentrated in central and northern Australia. This means that the Himawari-8 baseline LST was more consistent with MODIS LST in Australia's eastern coastal regions, yet tended to overestimate LST in central and northern Australia when compared to MODIS LST. Notably, the area of Lake Eyre, the largest salt-lake in inland Australia, exhibited the lowest coefficient value (˜2 K), which could be attributed to the absence of canopies within these highly reflective salt-lake regions. A more detailed analysis of the spatial pattern of SZAC coefficient is elucidated in Fig. 15. The distribution of the SZAC coefficient was also influenced by the scanning strategy employed by the MODIS instrument during its orbit which resulted in MODIS-induced strips in the SZAC coefficient. Nevertheless, as SZAC functions as a calibration factor to be subtracted from the Himawari-8 baseline LST, it introduces certain offsets associated with the emissivity artifacts within the baseline LST. This phenomenon is further elucidated in Fig. 5.

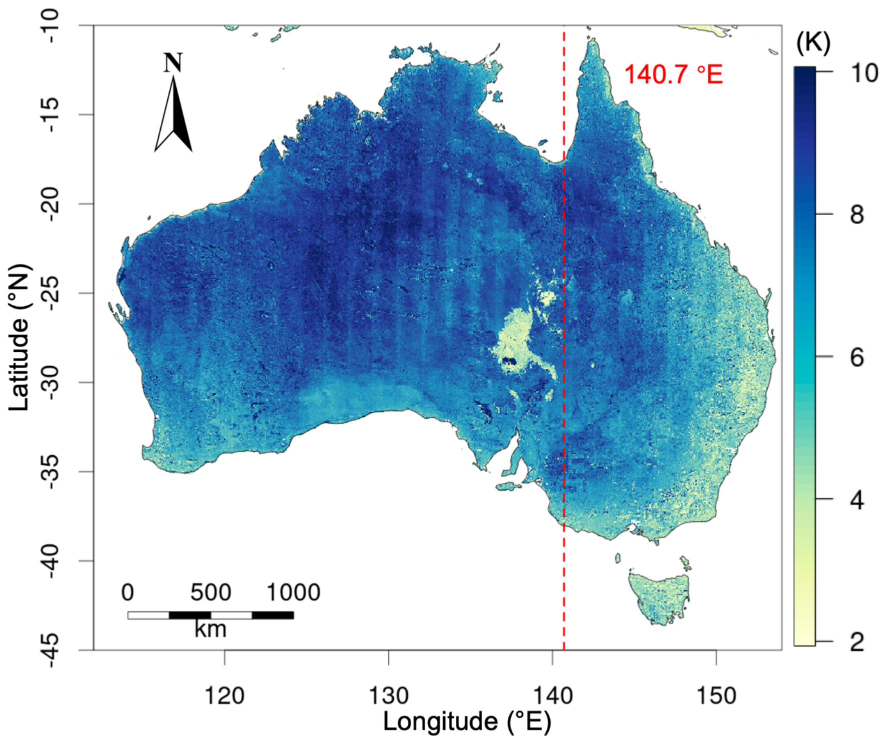

Figure 4: (a) Spatial distribution of the SZAC coefficient for the Australian continent during 01/Jan/2016 – 31/Dec/2020. The 'light-green / yellow' region just west of Himawari's longitude (140.7 °E represented by the red dashed line) exhibiting the lowest coefficient values of ˜ 2 K, is associated with Lake Eyre and other salt lakes within inland Australia.

Fig. 5 presents the spatial distribution of input emissivity, SZAC values, baseline and $\mathrm{ANU_{SZAC}}$ LST at 02:00 GMT (i.e., 12:00 AEST) on (a-d) 20/Mar/2016 (austral autumn equinox); (e-h) 21/Jun/2016 (austral winter solstice); (i-l) 23/Sep/2016 (austral spring equinox); and (m-p) 21/Dec/2016 (austral summer solstice). The SZAC values showed seasonal variations, being highest at the summer solstice (Fig. 5 n), moderate and comparable at the spring and autumn equinoxes (Fig. 5 b and j), and lowest at the winter solstice (Fig. 5 f). This variation signifies that the disparities between the baseline LST and MODIS LST were most pronounced in the summer, a period when incoming radiation peaks and necessitate a stronger correction. The systematic differences between the Himawari-8 baseline and MODIS LST in inland and northern Australia were always higher than other regions. Furthermore, both input emissivity (Fig. 5; first column) and SZAC values (Fig. 5; second column) exhibited artefacts associated with MODIS scanning effects. However, these artefacts were effectively removed by the calibration process as seen in both baseline (Fig. 5; third column) and $\mathrm{ANU_{SZAC}}$ LST (Fig. 5; fourth column).

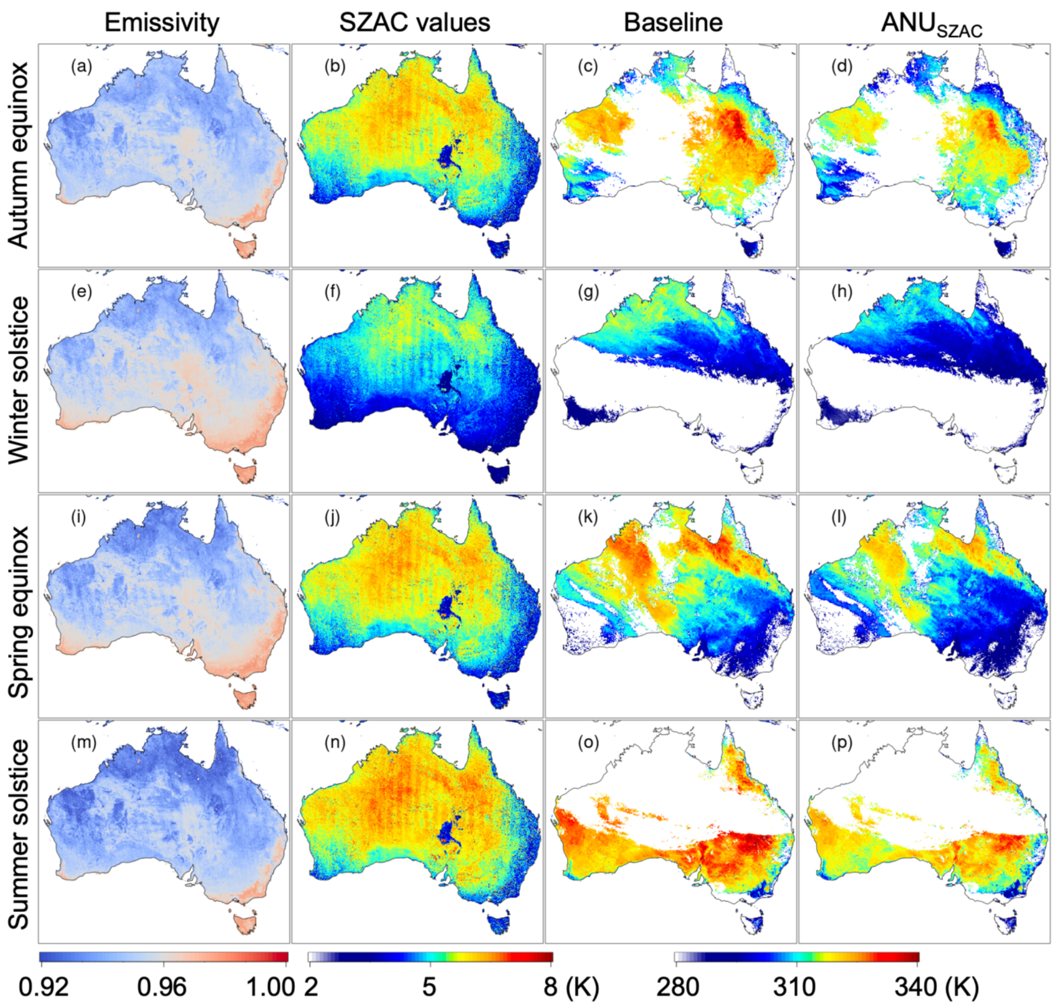

Figure 5: Respective spatial distribution of emissivity, SZAC values, baseline and ANU$_{SZAC}$ LST at 02:00 GMT on (a-d) 20/Mar/2016 (austral autumn equinox); (e-h) 21/Jun/2016 (austral winter solstice); (i-l) 23/Sep/2016 (austral spring equinox); and (m-p) 21/Dec/2016 (austral summer solstice). The oceans and seas surrounding Australia are white in all parts, with Himawari cloud contaminated pixels being white over land in the two columns on the right.

Fig. 6 presents the spatial distribution of bias (a-b) and ubRMSE (c-d) of baseline and ANU$_{SZAC}$ LST against best-quality MODIS LST for the Australian continent between 01/Jan/2016 and 31/Dec/2020. This evaluation assesses the fitting performance of ANU$_{SZAC}$ LST by comparing to the training set. The median bias of baseline LST against MODIS$_{best}$ LST for the Australian continent is 5.09 K while the median bias of ANU$_{SZAC}$ LST was reduced to 1.07 K. Both baseline and ANU$_{SZAC}$ LST demonstrated comparable levels of ubRMSE performance, being 2.50 K and 2.53 K, respectively. In general, both LST products exhibited the lowest ubRMSE values (ranging from 1 to 2 K) for much of inland Australia. However, over coastal regions, the ubRMSE increased to 2 to 3 K for both products (Fig. 6 b and e). The evaluation based on the training set demonstrated that SZAC could reduce the bias performance while maintaining a similar ubRMSE level.

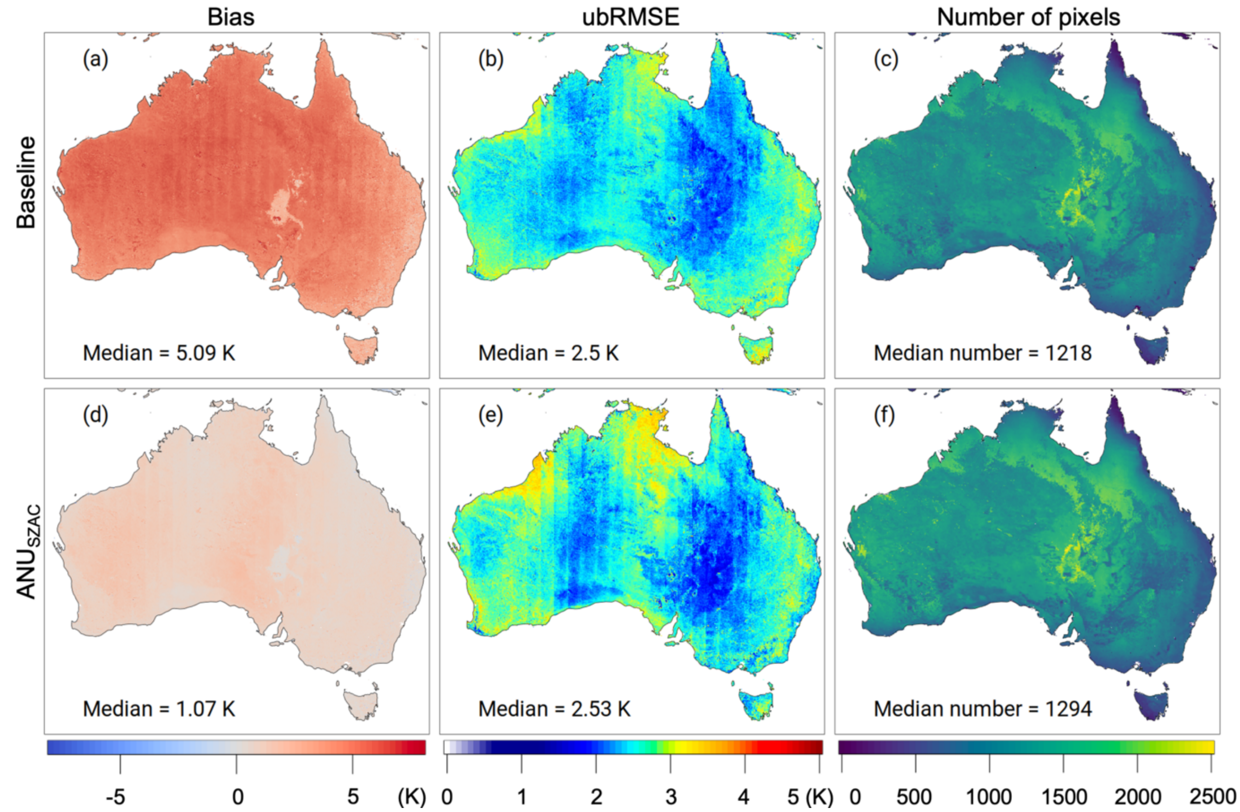

Figure 6: Spatial distribution of bias and ubRMSE of baseline and $\mathrm{ANU_{SZAC}}$ LST against best-quality (i.e., expected error < 1 K) MODIS (both MOD11A1 and MYD11A1) LST for the Australian continent between 01/Jan/2016 and 31/Dec/2020. The oceans and seas surrounding Australia are white in all parts.

Fig. 7 presents the spatial distribution of bias (a-d) and ubRMSE (e-h) of baseline, Chiba, Copernicus and $\mathrm{ANU_{SZAC}}$ LST against all available LST pixels from Terra-MODIS (i.e., MOD11A1) for the Australian continent at ˜ 10:30 local solar time between 01/Jan/2016 and 31/Dec/2020. The median bias of baseline, Chiba, Copernicus LST against Terra-MODIS LST for the Australian continent was 5.37, 3.71, 3.25 K, respectively, while the median bias of $\mathrm{ANU_{SZAC}}$ LST was only 1.52 K, less than half of the second-best other result (i.e., Copernicus LST). This indicates that $\mathrm{ANU_{SZAC}}$ LST outperformed the other LST products in terms of bias, demonstrating an improved agreement against the ˜ 10:30 local solar time Terra-MODIS LST. The median ubRMSE of baseline, Chiba, Copernicus LST was 2.47, 2.56 and 2.55 K, respectively, while the ubRMSE of $\mathrm{ANU_{SZAC}}$ LST was 2.75 K and showed more spatial variability.

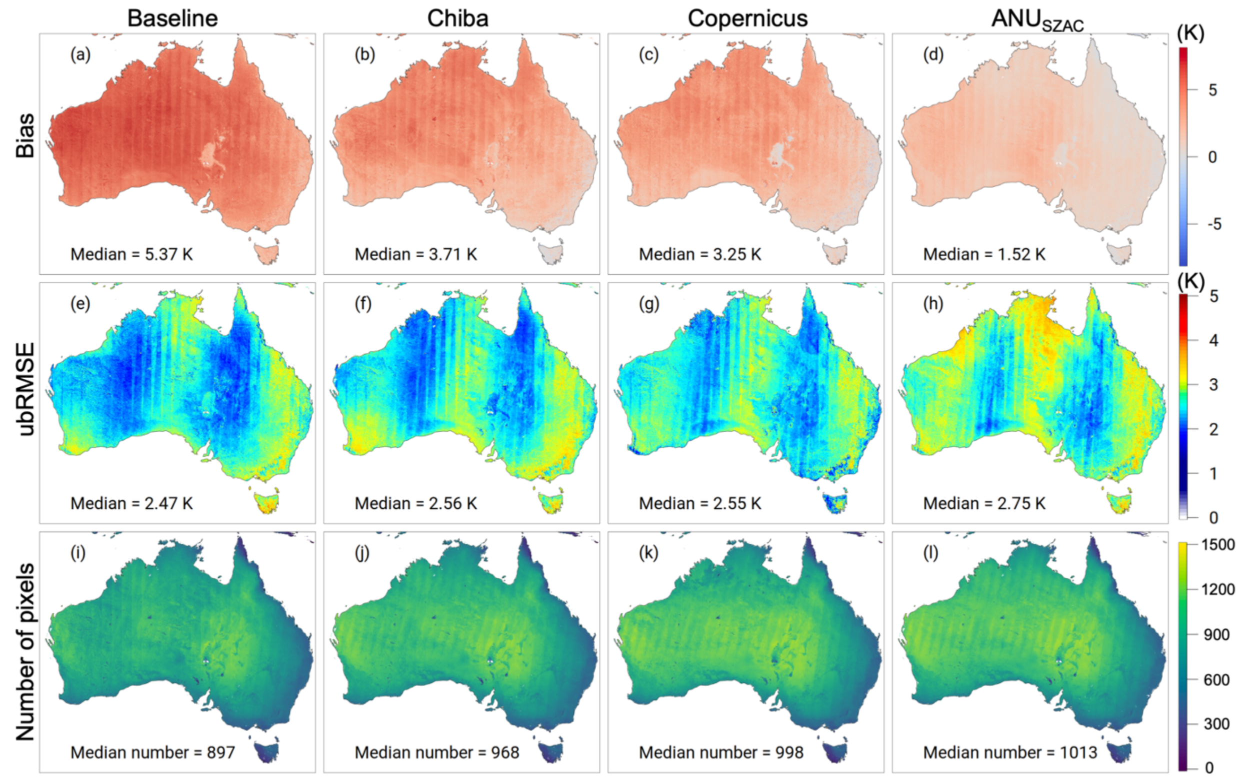

Figure 7: Spatial distribution of bias and ubRMSE of baseline, Chiba, Copernicus and ANU$_{\mathrm{SZAC}}$ LST against all available LST pixels from Terra-MODIS (i.e., MOD11A1) for the Australian continent at ~ 10:30 local solar time between 01/Jan/2016 and 31/Dec/2020. The oceans and seas surrounding Australia are white in all parts.

Fig. 8 presents the spatial distribution of bias (a-d) and ubRMSE (e-h) of baseline, Chiba, Copernicus and ANU$_{\mathrm{SZAC}}$ LST against all available LST pixels from Aqua-MODIS (i.e., MYD11A1) for the Australian continent at ~ 13:30 local solar time between 01/Jan/2016 and 31/Dec/2020. The median bias of baseline, Chiba, Copernicus LST against Aqua-MODIS LST for Australian was 4.85, 2.90 and 2.28 K, respectively. In contrast, ANU$_{\mathrm{SZAC}}$ LST exhibited a reduced median bias of 0.98 K, which was less than half of the second-best other result (i.e., Copernicus LST). This indicated that all Himawari-8 LST products showed better agreement in the afternoon (~ 13:30 local solar time) than the morning (~ 10:30 local solar time), while ANU$_{\mathrm{SZAC}}$ LST had a superior bias performance compared to the three other LST products in both the morning and afternoon. The median ubRMSE of baseline, Chiba, Copernicus and ANU$_{\mathrm{SZAC}}$LST was 2.42, 2.37, 2.48 and 2.44 K, respectively. Both baseline and ANU$_{\mathrm{SZAC}}$ LST displayed relatively lower ubRMSE values (~ 2 K) for inland regions with relatively higher values (~ 3 K) in the north. The differences in the direction of strips seen in Fig. 8 compared to Fig. 7 are attributed to the differences of orbits of Terra (descending at ~ 10:30 local solar time) and Aqua (ascending at ~ 13:30 local solar time) satellites.

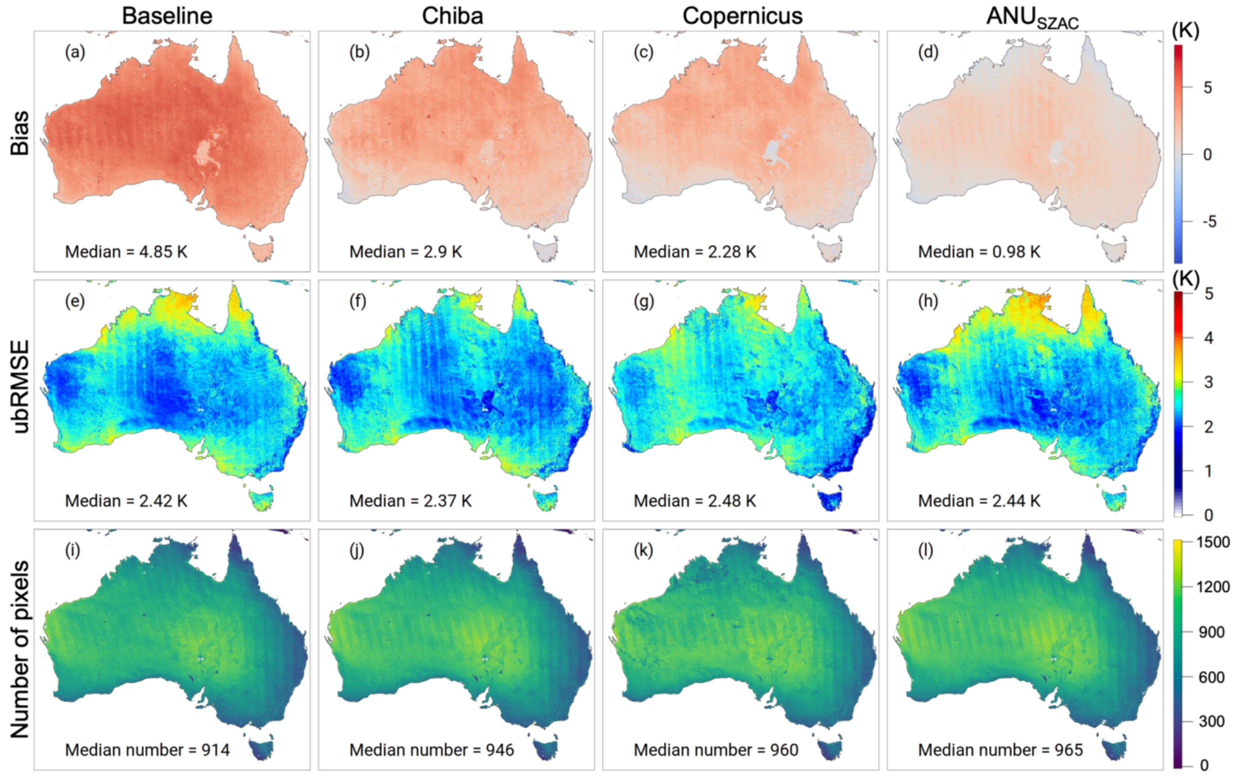

Figure 8: Spatial distribution of bias and ubRMSE of baseline, Chiba, Copernicus and ANU$_{SZAC}$ LST against all available LST pixels from Aqua-MODIS (i.e., MYD11A1) for Australia at ˜ 13:30 local solar time between 01/Jan/2016 and 31/Dec/2020. The oceans and seas surrounding Australia are white in all parts.

4.2 Evaluation against *in-situ* LST during 2016-2020

Fig. 9 presents the annual and seasonal boxplots of bias of baseline, Chiba, Copernicus and ANU$_{SZAC}$ LST against the *in-situ* LST derived at the 20 OzFlux sites (see Fig. 1 (b) for their locations) at different times (i.e., all day, daytime and nighttime) between 01/Jan/2016 and 31/Dec/2020. Regarding the all-day metrics (Fig. 9 a), the overall mean values of bias of baseline, Chiba, Copernicus and ANU$_{SZAC}$ LST were 1.87 K, -0.29 K, -0.57 K and 0.60 K, respectively. For the daytime evaluation (Fig. 9 b), the overall mean values of bias of baseline, Chiba, Copernicus and ANU$_{SZAC}$ LST were 4.23 K, 2.16 K, 1.73 K and 1.41 K, respectively. ANU$_{SZAC}$ LST exhibited better performance than baseline LST and outperformed Chiba and Copernicus in almost all seasons during daytime; while ANU$_{SZAC}$ LST was comparable with Copernicus LST in winter. For the nighttime evaluation (i.e., Fig. 9 c), the overall mean values of bias of baseline, Chiba, Copernicus and ANU$_{SZAC}$ LST against *in-situ* LST were 0.06 K, -2.29 K, -2.45 K and -0.06 K, respectively. As no SZAC was applied at the night, the baseline and ANU$_{SZAC}$ LST exhibit identical performance during nighttime. Both baseline and ANU$_{SZAC}$ LST consistently outperformed Chiba and Copernicus LST in all seasons during nighttime evaluations. It is notable that the superior all-day bias metrics of Chiba and Copernicus LST were due to the daytime and nighttime bias metrics essentially cancelling each other out. For detailed metrics of the individual 20 OzFlux sites, see Table S1 in the Supplementary material.

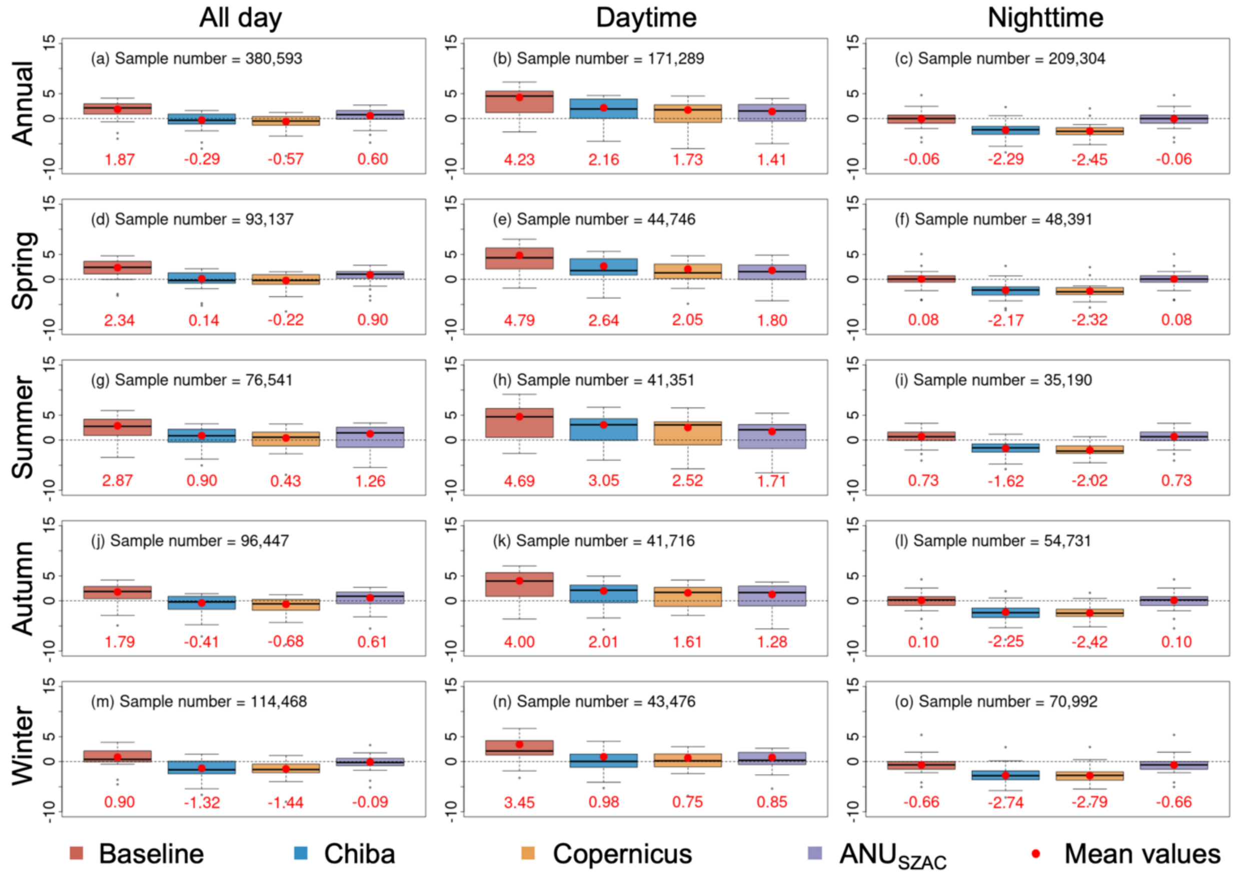

Figure 9: Annual and seasonal boxplots of bias of baseline, Chiba, Copernicus and $\mathrm{ANU_{SZAC}}$ LST against in-situ LST at different times (i.e., all day, daytime and nighttime) between 01/Jan/2016 and 31/Dec/2020. For the southern hemisphere spring is from September to November, summer from December to February, autumn from March to May, and winter from June to August. The dark horizontal line within the boxplots represents the median value; the upper and lower lines defining the coloured rectangle are the interquartile range (i.e., the 75% and 25% values) respectively; the upper and lower whiskers extend from the box represent the maximum and minimum values excluding any outliers. The red numbers at the bottom of each plot are the overall mean values of bias. The unit of bias is K.

Fig. 10 presents the annual and seasonal boxplots of ubRMSE of baseline, Chiba, Copernicus and $\mathrm{ANU_{SZAC}}$ LST against *in-situ* LST at different times (i.e., all day, daytime and nighttime) between 01/Jan/2016 and 31/Dec/2020 for the 20 OzFlux sites. Regarding the all-day metrics (Fig. 10 a), the overall mean values of ubRMSE of baseline, Chiba, Copernicus and $\mathrm{ANU_{SZAC}}$ LST were 3.98 K, 3.89 K, 3.69 K and 3.24 K, respectively. $\mathrm{ANU_{SZAC}}$ LST displayed a narrowed spread of ubRMSE in all seasons, which indicated that $\mathrm{ANU_{SZAC}}$ LST had the best overall agreement with *in-situ* LST. For the daytime evaluation (Fig. 10 b), the overall mean values of ubRMSE of baseline, Chiba, Copernicus and $\mathrm{ANU_{SZAC}}$ LST were 3.74 K, 3.62 K, 3.31 K and 3.24 K, respectively. $\mathrm{ANU_{SZAC}}$ LST demonstrated narrowed spread than baseline throughout all seasons. For the nighttime evaluation (Fig. 10 c), the overall mean values of ubRMSE of baseline, Chiba, Copernicus and $\mathrm{ANU_{SZAC}}$ LST against *in-situ* LST were 2.77 K, 2.57 K, 2.54 K and 2.77 K, respectively. The nighttime measurements of all four LST products were generally comparable across all seasons, with Copernicus LST showing a slightly greater uncertainty in the spread of ubRMSE. For detailed metrics of the individual 20 OzFlux sites, see Table S2 in the Supplementary material.

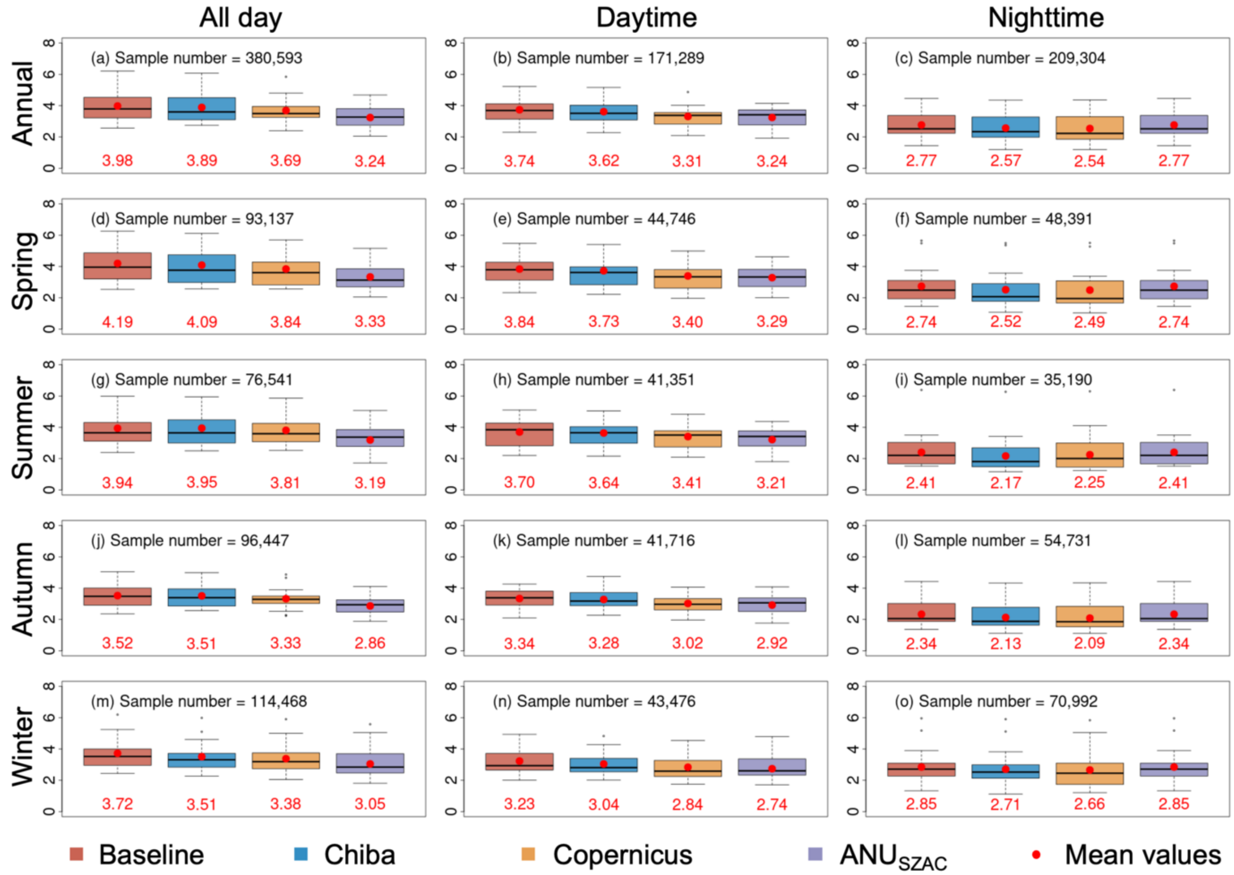

Figure 10: Annual and seasonal boxplots of ubRMSE of baseline, Chiba, Copernicus and ANU$_{\mathrm{SZAC}}$ LST against in-situ LST at different times (i.e., all day, daytime and nighttime) between 01/Jan/2016 and 31/Dec/2020. The explanation of seasonal division and boxplot features are the same as in the Fig. 9 caption. The red numbers at the bottom of each plot are the overall mean values of ubRMSE. The unit of ubRMSE is K.

Fig. 11 presents the hourly boxplots over the diurnal cycle of bias of baseline, Chiba, Copernicus and ANU$_{\mathrm{SZAC}}$ LST against *in-situ* LST in local standard time zone between 01/Jan/2016 and 31/Dec/2020. During the daytime, ANU$_{\mathrm{SZAC}}$ LST showed smaller bias values compared to baseline LST. This was evident as the bias of ANU$_{\mathrm{SZAC}}$ LST was closer to the zero-bias line, indicating a reduced systematic error. Additionally, the spread of boxplots representing the variation of bias at different sites was also narrowed for ANU$_{\mathrm{SZAC}}$ LST. The biggest improvement in bias of ANU$_{\mathrm{SZAC}}$ LST was observed around midday (i.e., 10:00-12:00 local standard time), corresponding to the time when the SZAC coefficients reach their maximum thus the calibration had the strongest effects (see Fig. 3 a). On the other hand, both Chiba and Copernicus LST showed better bias performance than baseline during the daytime. However, both Chiba and Copernicus LST exhibited negative bias during the nighttime, indicating an underestimation of LST values compared to *in-situ* measurements. In contrast, during the nighttime the median values of baseline and ANU$_{\mathrm{SZAC}}$ LST were close to the zero-bias line. Overall, the calibration process applied to ANU$_{\mathrm{SZAC}}$ LST effectively mitigated most systematic errors, resulting in improved accuracy during daytime hours.

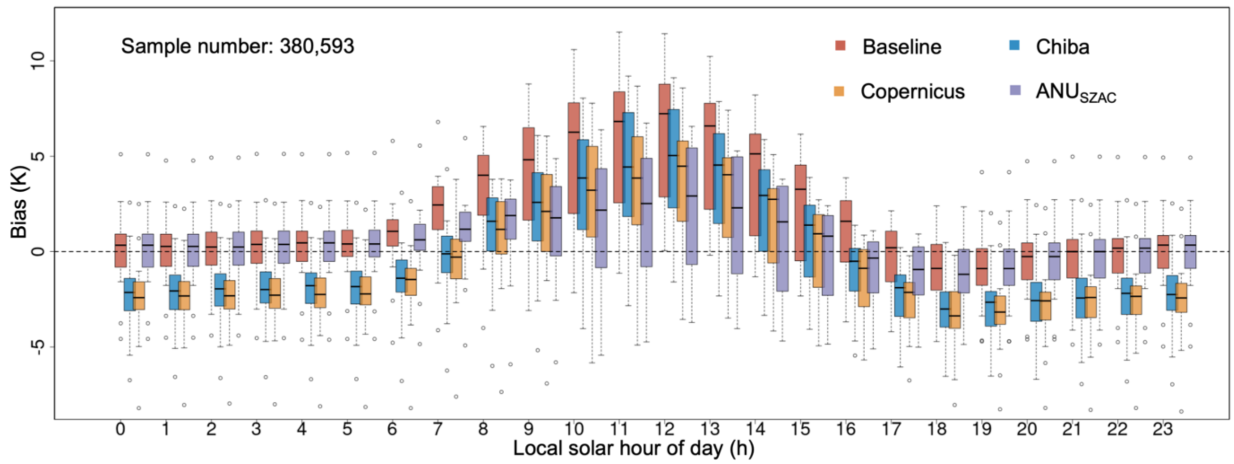

Figure 11: Hourly boxplots over the diurnal cycle of bias of baseline, Chiba, Copernicus and ANU$_{\mathrm{SZAC}}$ LST against in-situ LST in local standard time zone between 01/Jan/2016 and 31/Dec/2020. The boxplot features are fully explained in the Fig. 9 caption.

Fig. 12 presents four examples of temporal variation of baseline, Chiba, Copernicus, ANU$_{\mathrm{SZAC}}$ and *in-situ* LST in local standard time zone at (a) Cumberland Plain, (b) Daly Uncleared, (c) Gingin and (d) Tumbarumba sites within a 150-hour temporal window (see Fig. 1 (b) for the locations of these OzFlux sites). All four Himawari-8 LST products showed consistent diurnal cycles with *in-situ* LST measurements. Among them, the baseline LST was generally overestimated during daytime (a-c), which has been effectively resolved in ANU$_{\mathrm{SZAC}}$ LST. As a comparison, ANU$_{\mathrm{SZAC}}$LST exhibited similar temporal patterns with Chiba and Copernicus LST during daytime, aligning more closely with their diurnal cycles. However, ANU$_{\mathrm{SZAC}}$ LST retained the nighttime component of baseline LST, which generally demonstrates better agreement with *in-situ* LST during nighttime, aligning more closely with the observed LST values in most cases.

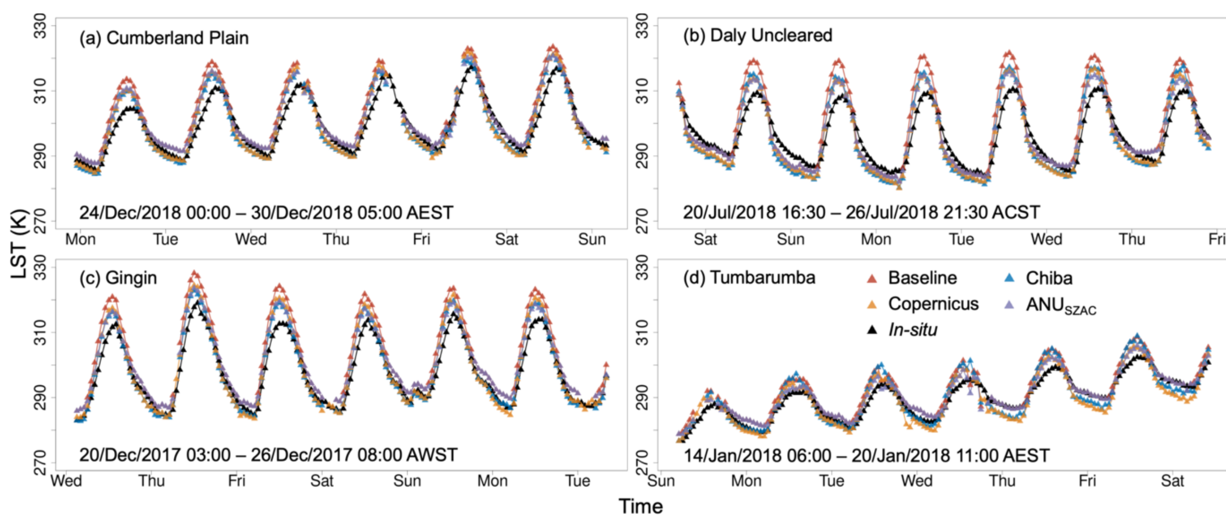

Figure 12: Four examples of temporal variation of baseline, Chiba, Copernicus, ANU$_{\mathrm{SZAC}}$ and in-situ LST in local standard time zone at (a) Cumberland Plain, (b) Daly Uncleared, (c) Gingin and (d) Tumbarumba OzFlux sites within a 150-hour window. The legend in (d) applies to all other parts. The locations of the four sites are shown in Fig. 1 (b) with additional site information provided in Table 3.

4.3 Spatial comparison against VIIRS LST during 2016-2020

Fig. 13 presents the spatial distribution of bias and ubRMSE of baseline, Chiba, Copernicus and ANU_{SZAC} LST against all available LST pixels from VIIRS (i.e., VNP21A1D) for the Australian continent at ˜ 13:30 local solar time between 01/Jan/2016 and 31/Dec/2020. The median bias of baseline, Chiba, Copernicus and ANU_{SZAC} LST against VIIRS LST was 3.02, 1.07, 0.33 and -0.63 K, respectively. This indicates that all Himawari-8 LST products demonstrated less bias when compared against VIIRS LST than when compared against Aqua-MODIS LST (which was 4.85, 2.90, 2.28 and 0.98 K, respectively; see Fig. 8). Notably, both VIIRS and Aqua-MODIS have an overpass time of ˜ 13:30 local solar time making this comparison essentially free of diurnal cycle influences. The median ubRMSE of baseline, Chiba, Copernicus and ANU_{SZAC} LST against VIIRS LST was 3.07, 2.84, 2.92 and 2.94 K, respectively. ANU_{SZAC} LST exhibited reduced values of ubRMSE in northern and mid-eastern regions of Australia compared to the baseline LST. In general, ANU_{SZAC} LST was more comparable to Copernicus LST than the two other products in terms of bias and ubRMSE metrics. However, ANU_{SZAC} offered the additional advantage of higher spatial resolution (i.e., 2 km for ANU_{SZAC} and ˜ 4.5 km for Copernicus) and better temporal frequency (i.e., 10 min for ANU_{SZAC} and 1 hour for Copernicus); see Table 2.

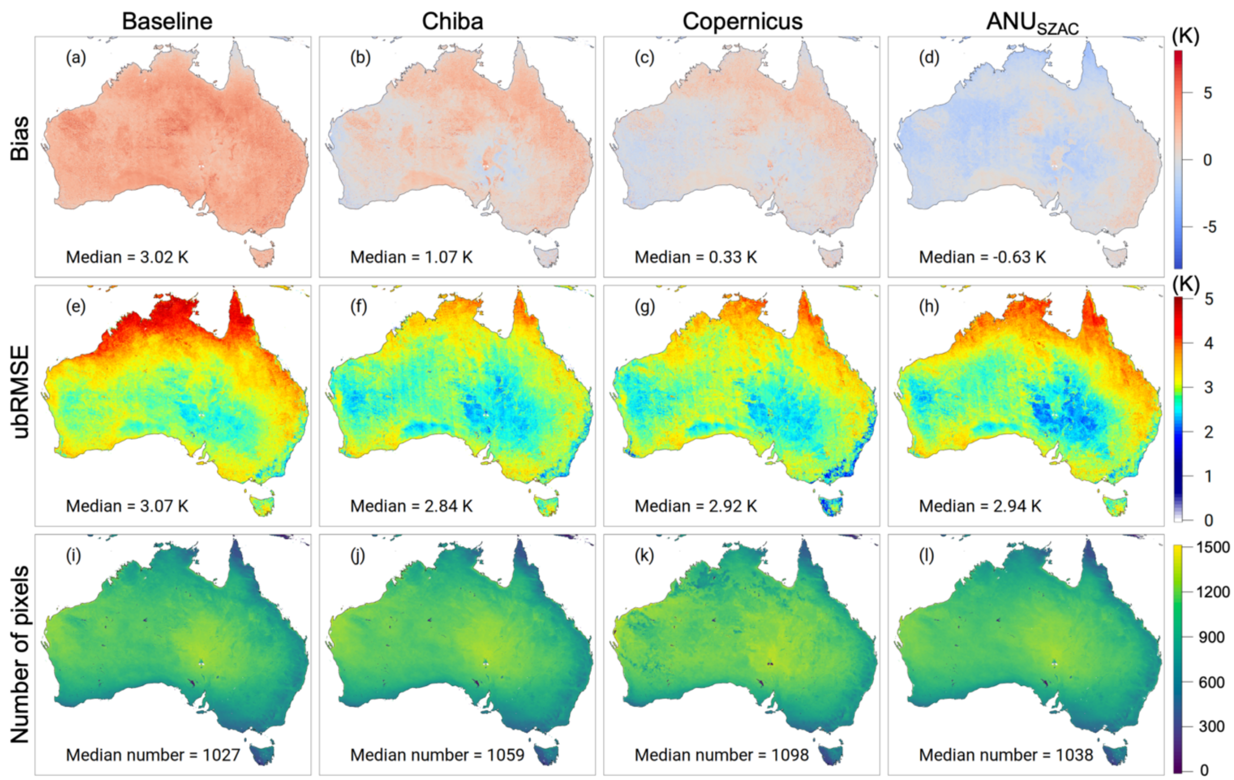

Figure 13: Spatial distribution of bias and ubRMSE of baseline, Chiba, Copernicus and ANU_{SZAC} LST against all available LST pixels from VIIRS (i.e., VNP21A1D) for Australia at ˜ 13:30 local solar time between 01/Jan/2016 and 31/Dec/2020. The oceans and seas surrounding Australia are white in all parts.

Fig. 14 presents two examples of spatial pattern comparison of baseline, Chiba, Copernicus and ANU_{SZAC} LST against VIIRS LST at 04:00 GMT (i.e., equivalent to 14:00 AEST, 13:30 ACST or 12:00 AWST) on 20/Jun/2019 (austral winter) and 20/Dec/2019 (austral summer), respectively. On both days, the four Himawari-8 LST products exhibit similar spatial patterns, though differences are observed. On 20/Jun/2019, the baseline LST generally showed higher values in the north-western regions; while on 20/Dec/2019, the baseline LST displayed higher values in eastern regions. In contrast, ANU_{SZAC}LST demonstrated more similarity with Chiba, Copernicus on both days, showing reduced discrepancies with the reference VIIRS LST product. On 20/Jun/2019, the differences of Chiba, Copernicus and ANU_{SZAC} LST against VIIRS were visually similar (Fig. 14, second column from left). On 20/Dec/2019, Chiba LST showed slightly higher values while ANU_{SZAC} LST exhibited slightly lower values compared to VIIRS LST (Fig. 14, right most column). The spatial comparisons presented in Fig. 14 were consistent with the pixelwise metrics indicated in Fig. 13.

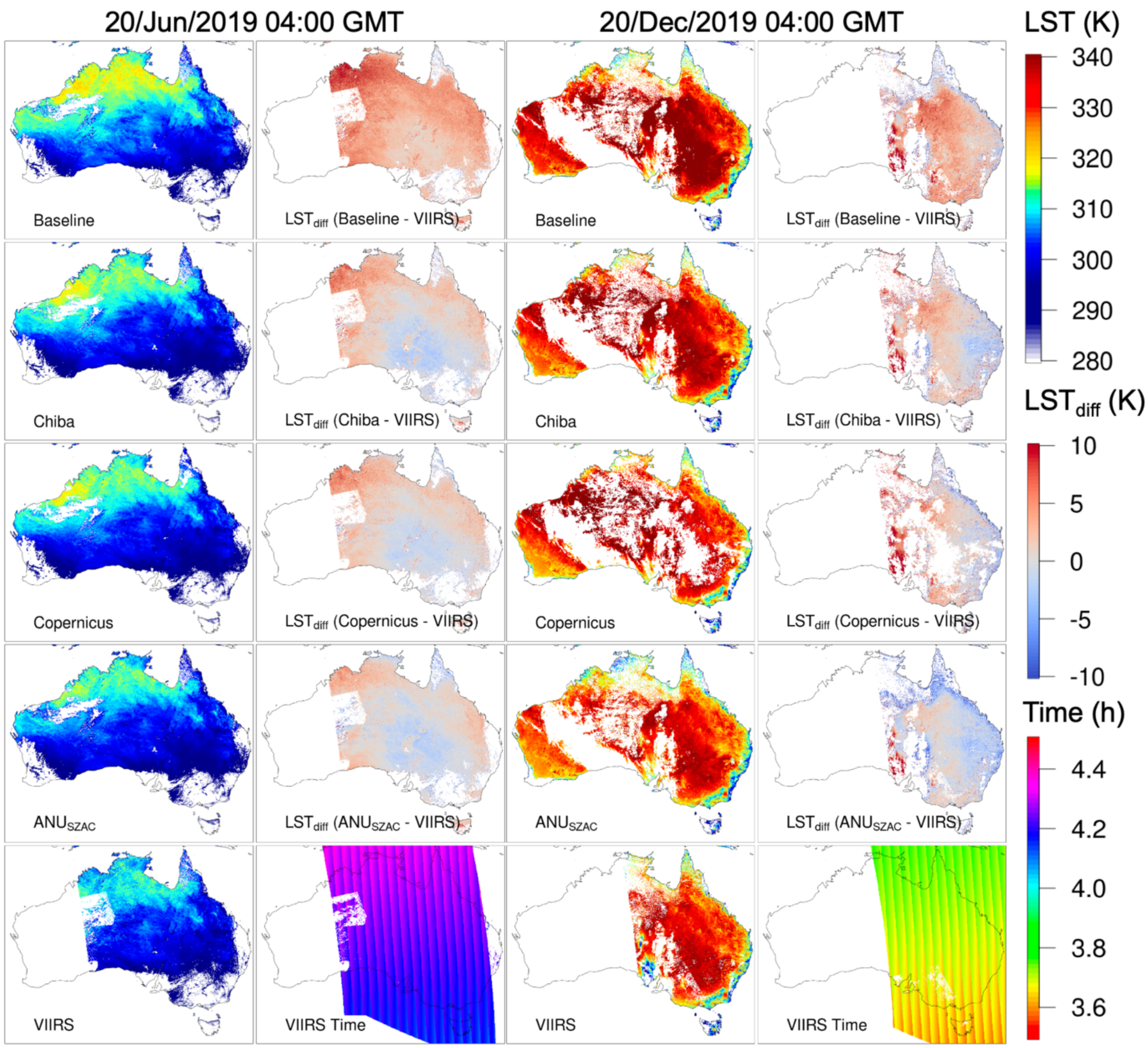

Figure 14: Two examples of spatial comparison of baseline, Chiba, Copernicus and ANU_{SZAC} LST against VIIRS LST at 04:00 GMT on 20/Jun/2019 and 20/Dec/2019, respectively. The first and third columns from the left are LST from the four Himawari products with VIIRS being the bottom row. The first four rows of the second and fourth columns from the left are differences (denoted 'LST_{diff}' in the legend) between each Himawari-8 LST product (in turn) and the VIIRS LST. The last rows of the second and fourth columns from the left are the VIIRS view time strips (in GMT). The oceans and seas surrounding Australia, cloud contaminated pixels and areas beyond the VIIRS swath are white in all parts.

5. Discussion

5.1 Distribution of SZAC coefficient and its physical implications

Numerous studies have noted discrepancies between LST acquired at essentially the same time from both geostationary and polar-orbiting platforms (e.g., Li et al., 2020; Trigo et al., 2021; Pérez-Planells et al., 2023). Nighttime LST products exhibit good agreement across various viewing configurations, whereas daytime observations have discrepancies attributed to the influence of shadows and temperature gradients within the landscape cover (Guillevic et al., 2013). As a result, SZA in conjunction with emissivity has been extensively applied to rectify the angular effects and enhance agreement of LST products acquired from different platforms (Vinnikov et al., 2012; Ermida et al., 2017; Ermida et al., 2018). Herein, we examined the diurnal patterns of baseline LST errors and proposed the SZAC approach, which leverages the dynamics of SZA (which mainly changes as a function of latitude, time-of-day and day-of-year) to spatiotemporally correct the daytime component of baseline LST measurements. There are four insights gleaned from this research.

Firstly, the effectiveness of SZA as an input for spatial correction lies in its cosine value, which is associated with the ratio of shadowed area to the total surface area. This property makes SZA a representative measure of the solar radiance reaching the Earth's surface (Yeom et al., 2012). Vinnikov et al. (2012) also emphasised that an SZA-based kernel is closely tied to the spatial inhomogeneity in surface heating and shadowing across diverse regions of the land surface and its cover. Moreover, the variability of SZA is linked to diurnal changes, seasonal fluctuations, and latitudinal differences. Consequently, it serves as a valuable bridging parameter to quantify the systematic differences between diverse LST products, which were developed using different underlying assumptions and showed systematic differences (see Table 1).

Secondly, the SZAC coefficient revealed negative associations with vegetation cover characteristics and exhibited a greater degree of uniformity within inland regions, where calibration effects exerted a more pronounced influence. Fig. 15 shows (a-d) the continental-scale and (e-t) zoomed comparisons between the spatial patterns of SZAC coefficient and 5-year median values of MODIS EVI, LAI and albedo between 01/Jan/2016 and 31/Dec/2020 for four chosen regions, respectively. The greater uniformity observed in inland arid regions was attributed to their predominantly homogeneous and larger patches of vegetation (Fig. 15 a-d). In contrast, pixels along the eastern coastlines exhibited greater heterogeneity (Region A and C; Fig. 15 e-h and q-t), characterised by denser vegetation and relatively mountainous terrain. This coastal area, where more population reside, featured more heterogeneous landscapes. Additionally, in forests, the closed canopy leads to a more even distribution, reducing internal shadowing compared to woodland areas with lower tree density. Furthermore, the SZAC coefficient and all three MODIS indices manifested distinct boundary effects within the Nullarbor Plain area (Region B; Fig. 15 i-l), an important biogeographic region as defined by the Australian Government (DCCEEW, 2020). Finally, it is noteworthy that for the Lake Eyre area (Region C; Fig. 15 m-p), the SZAC coefficient demonstrated strong connections with the masked area of LAI, which were all salt lakes, signifying the absence of canopies. The albedo of region C was also the highest within Australia, demonstrating a distinctive characteristic of highly reflective surfaces in this area.

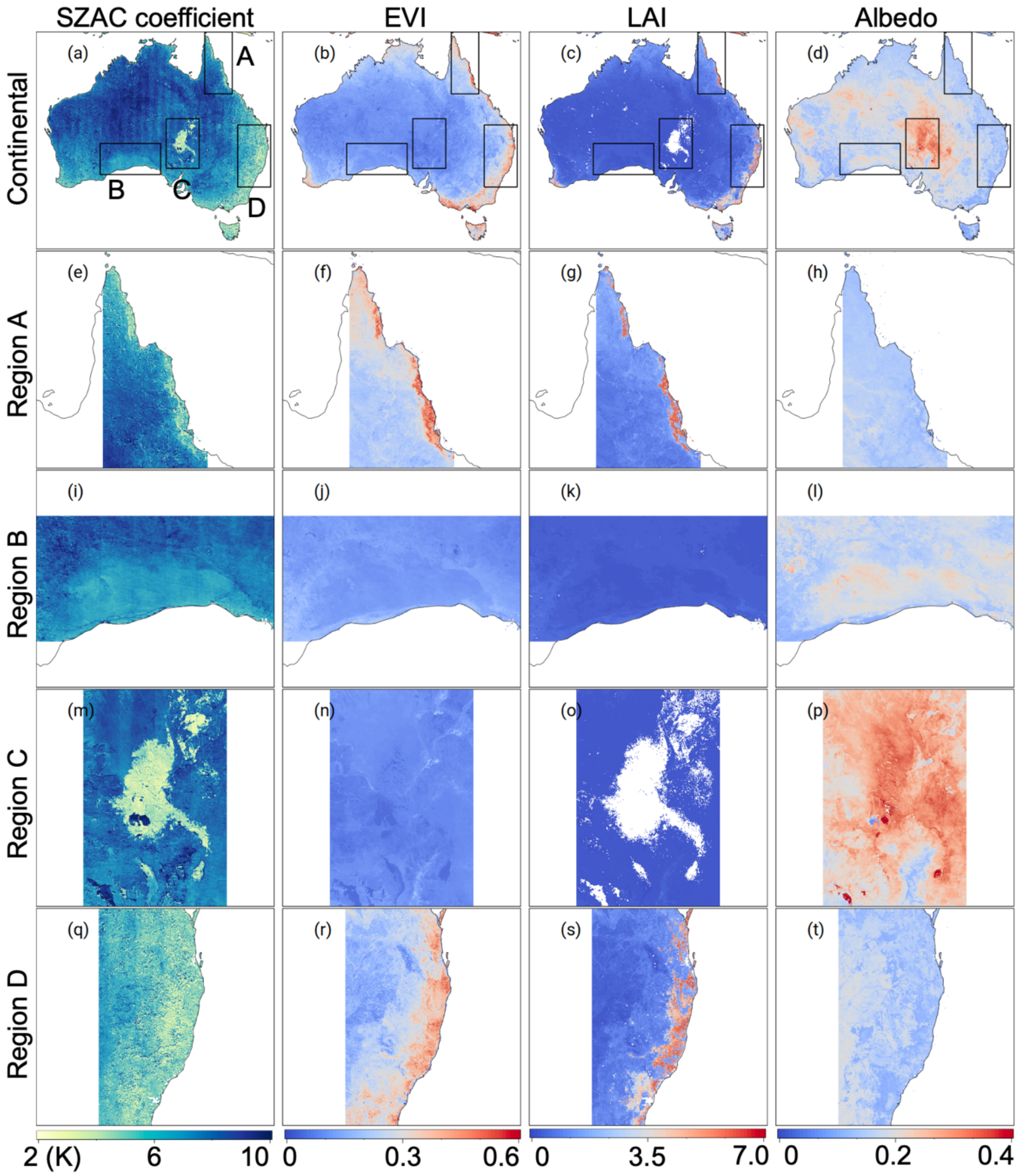

Figure 15: (a-d) Continental-scale and (e-t) zoomed comparisons between the spatial patterns of SZAC coefficient and 5-year median values of MODIS EVI, LAI and albedo between 01/Jan/2016 and 31/Dec/2020 for region A, B, C and D, respectively. Region A spans 142-147 °E and 10-20 ° S; region B spans 123-134 ° E and 28-33 °S; region C spans 135-141 °E and 24-32 °S; and region D spans 148-154 °E and 25-35 °S.

Fig. 16 presents violin plots illustrating the values of the SZAC coefficient within four equal-value-range quantiles for (a) EVI, (b) LAI, and (c) albedo between 01/Jan/2016 and 31/Dec/2020. For both EVI and LAI, the SZAC coefficient exhibited similar decreasing trend with increasing vegetation indices. As depicted in Fig. 16 (a) and (b), when EVI (LAI) was concentrated within the range of 0-0.15 (0-1.75), the median values of SZAC coefficient were 7.97 K (7.75 K); conversely, when EVI (LAI) was concentrated within the range of 0.45-0.60 (5.25-7.00), the median values of SZAC coefficient decreased to 4.87 K (4.71 K). This trend aligns with the observations in Fig. 15 (a-c), where higher SZAC coefficient values were associated with sparser vegetation (inland Australia), while lower values were linked to denser vegetation and more complex landscapes (eastern coastal Australia). Concerning albedo, the SZAC coefficient demonstrated a positive relationship when albedo was lower than 0.30. However, when albedo was concentrated within the range of 0.30-0.40, the SZAC coefficient exhibited high uncertainties, indicating a lack of strong connections between them in such scenarios. These findings reinforce the relationship between the spatial pattern of SZAC coefficient and vegetation cover characteristics.

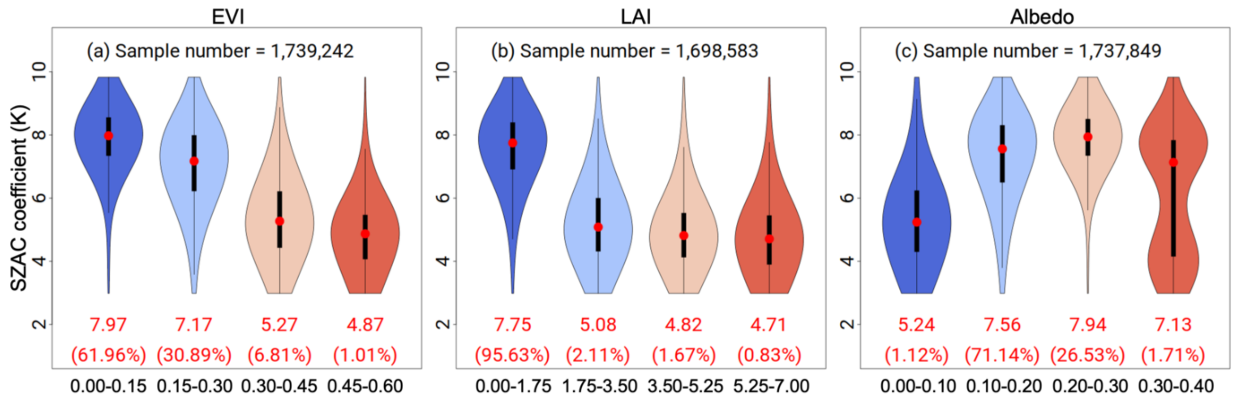

Figure 16: Violin plots of the values of SZAC coefficient within four equal-value-range quantiles for (a) EVI; (b) LAI; and (c) albedo, respectively, between 01/Jan/2016 and 31/Dec/2020. The red dots within violins represent the median value; the bold vertical black lines within violins are the interquartile range (i.e., the 75% and 25% values, respectively); the upper and lower limits of violins represent the maximum and minimum values excluding any outliers; the distribution of violins represent the kernel density of sample numbers within each quantile. The red decimal numbers (percentage) at the bottom of each plot are the median values (percentage of overall sample numbers) of SZAC coefficient within each quantile.

Thirdly, it is noteworthy that the distribution of the SZAC coefficient may be influenced by VZA of the employed satellites (Himawari-8, Terra and Aqua), although VZA was not explicitly incorporated into the calibration process. In Fig. 4, a discernible pattern in SZAC dependence was observed, particularly in relation to the longitudinal position of 140.7° E (i.e., the longitude of Himawari-8). It becomes evident that SZAC values are lower in southern regions near this longitude and higher in areas situated farther away, such as those in Western Australia (WA) and western South Australia (SA). This pattern could be attributed to the fixed VZA of Himawari-8, where a shorter atmospheric path (or lower VZA values) tends to enhance the accuracy of LST retrievals. Additionally, the distribution of the SZAC coefficient is also influenced by the viewing geometries of MODIS satellites (see Fig. 4), specifically the Terra descending and Aqua ascending orbits.

Fourthly and finally, in alignment with various parametric modelling approaches, such as diurnal temperature cycle (DTC) models, the SZAC coefficient holds physical interpretations and implications. Yamamoto et al. (2023) recently explored DTC models using Himawari-8 LST data as inputs, revealing that the maximum daily LST (T_{max}) and its diurnal temperature range (DTR) emerged as particularly informative parameters for monitoring vegetation drying signals under heatwave. This was attributed to heightened sensitivity of T_{max} to geometric conditions of sun-target-observer, its stability in model fitting, and its correlations with other environmental variables like vegetation indices and soil moisture. In this research, the SZAC coefficient was derived based on SZA values ranging from 20 to 70 ° and can be conceptualised as representing the 'magnitude of LST disparities between different platforms during the heating period of surface'. Fig. 3 illustrated when SZA approaches its minimum value (around midday), the magnitude of LST differences (and correction effect of SZAC) attains its maximum extent. Given that SZA represents the angle formed between the Sun's rays and the vertical direction, this phenomenon signifies a vital relationship between the extent of shadowing and the observed variations in LST. Moreover, the SZAC approach is consistent with previous studies that modelled DTC models by relying on sparse polar-orbiting LST observations (Duan et al., 2012; Hu et al., 2020a; Lu and Zhou, 2021). However, the performance of SZAC within 'twilight times' may require further re-evaluation due to limited available data during the time of day-to-night transition (and vice versa). The lack of data during day-night transitions can potentially introduce uncertainties in performance of SZAC, especially when dealing with rapid temperature changes and complex atmospheric conditions within twilight zones (Kurihara et al., 2016; Eytan et al., 2020).

5.2 Usage and prospects of SZAC

SZAC has demonstrated robustness and operational capability in reducing systematic bias when compared to MODIS, VIIRS and *in-situ* LST measurements. Additionally, the $\mathrm{ANU_{SZAC}}$ LST derived from the SZAC approach showed a reduction of ˜ 0.5 K in ubRMSE compared to the baseline LST when evaluated against daytime *in-situ* LST (Fig. 10). When compared to MODIS-Aqua and VIIRS LST, $\mathrm{ANU_{SZAC}}$ LST maintained a similar level of ubRMSE with the other three Himawari-8 LST products (i.e., baseline, Chiba, Copernicus). These findings underscore SZAC's capability to reduce error deviations (as demonstrated by the ubRMSE statistics against *in-situ* LST) while aligning LST values more closely with those obtained from polar-orbiting platforms (see the bias statistics). It demonstrates consistency with LSTs from both new generation geostationary satellites, thereby offering additional choices for researchers and practitioners who rely on LST snapshots from MODIS and VIIRS. For applications needing high temporal frequency thermal observations, $\mathrm{ANU_{SZAC}}$ LST emerges as a valuable alternative or complement to the polar-orbiting MODIS and VIIRS.

The $\mathrm{ANU_{SZAC}}$ LST did exhibit a higher ubRMSE than the other three products when compared against Terra-MODIS. This heightened uncertainty may stem from variations in SZA, particularly when SZA surpasses 50 ° (see Fig. 3 a), where the Himawari-8 baseline-MODIS difference and SZA becomes more variable under these circumstances. This increased variability of baseline-MODIS difference may be attributed to the weaker incoming solar radiance during the Terra overpass time (compared to Aqua and Suomi-NPP), diminishing the relative importance of SZA. Liu et al. (2009) similarly highlighted that global solar measurements may experience degradation due to cosine errors when SZA becomes large. Moreover, higher SZA values indicate an extended solar atmospheric path length, amplifying the potential impact of minor errors in precipitable water parameterisation on both baseline LST and SZAC correction attempts. Consequently, SZAC may introduce more uncertainties and spatial variabilities during Terra overpass time. However, considering the wavelength-dependent drift in reflectance, particularly with a drop of up to 8% in the shortest wavelength region observed in Terra-MODIS NIR spectral bands (Wu et al., 2013), it becomes crucial to prioritise consistency with Aqua-MODIS and VIIRS LST, where $\mathrm{ANU_{SZAC}}$ has demonstrated commendable performance.

The coefficient of SZAC was optimised against best-quality LST pixels from MOD/MYD11 series, which may warrant reconsideration or improvements in the future, given the dynamic nature of remote sensing data and advancements in satellite missions. As the Terra-MODIS mission was discontinued since November 2022, this would impact the availability of MODIS data and raise questions about the long-term sustainability of using MOD/MYD11 LST for calibration and evaluation. Alternative satellite missions and/or newer generation sensors should be considered to maintain the ongoing accuracy of the SZAC algorithm. Meanwhile, studies have reported certain limitations of the MOD/MYD11 LST product, particularly its tendency to underestimate LST during daytime in certain regions (Li et al., 2014). Inconsistencies have been identified between MOD/MYD11 and their successor VNP21, with MYD11 LST typically being 2 K cooler than VNP21 LST (Hulley et al., 2017). To address this issue, NASA produced two LST&E products (i.e., MOD/MYD21) to ensure data continuity among these platforms, with the bias of MYD21 LST against VNP21 LST narrowed to ˜ 0.4 K. Though $\mathrm{ANU_{SZAC}}$ LST has already demonstrated acceptable consistencies with MOD/MYD11 and VNP21 LST, it is crucial to consider further comparisons of $\mathrm{ANU_{SZAC}}$ against MOD/MYD21. Moreover, future calibrations might simultaneously incorporate MYD21 and VNP21, necessitating ongoing evaluations. It would be beneficial to compare $\mathrm{ANU_{SZAC}}$LST with other new generation LST products, e.g., the ECOsystem Spaceborne Thermal Radiometer Experiment on Space Station (ECOSTRESS) LST (Fisher et al., 2020). However, caution must be exercised when designing the experiments and comparison workflow due to the inherent spatiotemporal variability of LST. ECOSTRESS LST, with its irregular revisit frequency and 70 m spatial resolution, may not be suitable for direct comparison purposes. To address this, a matching strategy and spatial downscaling techniques (e.g., Yu et al., 2023) could be thoughtfully implemented in the comparison process to ensure meaningful and accurate assessments.

SZAC has shed light on potential LST calibration methods for the future, suggesting the need for spatially varied coefficients to better accommodate localised conditions. The SZAC coefficient is highly relevant to the diurnal pattern of LST error variations for a specific region and can be optimised for observation areas of different geostationary satellites. Using MODIS LST data covering Australia, we presented a pixelwise optimisation strategy that ensured ANU_{SZAC} LST incorporated MODIS LST spatial variability over the entire continent. However, LST also has considerable temporal variability and is highly dependent on localised conditions (Van De Kerchove et al., 2013; Sekertekin et al., 2016). Thus, this optimisation strategy could be extended temporally to derive seasonally dependent sets of coefficients, which may improve the accuracy of ANU_{SZAC} LST in capturing the seasonal variability of LST. However, strategies would need to be enlisted to ensure artificial step-changes in LST aren't introduced across the seasonal boundaries. Furthermore, implementing SZAC on LST using data acquired by other geostationary satellites, such as the GOES series in the Americas and the Meteosat series over Europe and Africa, may be a promising direction for future research. Developing a globally adaptive SZAC coefficient set could potentially improve our understanding of the error characteristics of overlapping geostationary satellites and enable the creation of a new global-coverage geostationary LST product, similar to the Copernicus LST. It will also help identify any potential regional biases and/or limitations of the current SZAC approach, allowing for targeted refinements and calibrations to improve accuracy and applicability. This could enhance our ability to monitor and study LST globally and aid in applications such as weather forecasting, climate modelling, and ecological and agricultural monitoring.

6. Conclusion

Numerous studies have reported the discrepancies between LST obtained from geostationary platforms and those from polar-orbiting missions, which can be particularly high (e.g., 12 K) during the daytime due to variations in viewing angles and shadowing effects. To overcome this challenge, SZA serves as a bridging parameter to systematically quantify differences between platforms. We proposed SZAC to operationally calibrate the daytime component of a Himawari-8 SW algorithm retrieved LST. SZAC is an empirical function based on the variations of SZA, describing the spatial heterogeneity and magnitude of LST discrepancies from different products.

We evaluated the calibrated LST product (ANU_{SZAC}) against MODIS LST and VIIRS LST, as well as *in-situ* LST measurements from the OzFlux network. We also compared ANU_{SZAC} LST with three Himawari-8 LST datasets (baseline, Chiba and Copernicus) over 01/Jan/2016 to 31/Dec/2020. The median values of bias of ANU_{SZAC} LST during daytime against Terra-MODIS LST, Aqua-MODIS LST and VIIRS LST were 1.52 K, 0.98 K and -0.63 K, respectively. In contrast, the other three Himawari-8 LST products had at least doubled bias against MODIS LST datasets. Additionally, the baseline and Chiba LST displayed higher bias than ANU_{SZAC} LST against VIIRS LST, whereas Copernicus LST showed good agreement with VIIRS LST, being a bias of 0.33 K. All four Himawari-8 LST products showed comparable ubRMSE when compared to LST from polar-orbiting platforms (i.e., MODIS and VIIRS). In the evaluation against daytime *in-situ* LST, the overall mean values of bias (ubRMSE) of baseline, Chiba, Copernicus and ANU_{SZAC} LST were 4.23 K (3.74 K), 2.16 K (3.62 K), 1.73 K (3.31 K) and 1.41 K (3.24 K), respectively. This demonstrated the lower bias of ANU_{SZAC} LST, and similar deviation of uncertainty (represented by ubRMSE), when evaluated against peer products.

Overall, SZAC demonstrated robustness and operational capability in reducing systematic bias in comparison to MODIS, VIIRS and *in-situ* LST measurements. It has shed light on potential calibration methods for the future, suggesting the need for spatially varying coefficients to better accommodate localised conditions. It is possible to extend SZAC using data acquired from other geostationary satellites, such as the GOES series in the Americas and the Meteosat series over Europe and Africa. This should improve our understanding of the error characteristics of overlapped geostationary imageries, allowing for targeted refinements and calibrations to further enhance applicability.

Acknowledgement

This research was performed as part of a PhD by the first author (YY) under an academic collaboration between the Australian National University (ANU) and the Commonwealth Scientific and Industrial Research Organisation (CSIRO). This research was undertaken while supported by the ANU University Research Scholarship and an ANU-CSIRO Digital Agriculture PhD Supplementary Scholarship through the Centre for Entrepreneurial Agri-Technology (CEAT). We thank the continued support of the TERN Landscapes Observatory (`https://www.tern.org.au/tern-observatory/tern-landscapes/`), a sensing platform of the Terrestrial Ecosystem Research Network (TERN; `https://www.tern.org.au/`), which is supported and enabled by the Australian Government through the National Collaborative Research Infrastructure Strategy (NCRIS). We acknowledge the resources and services provided by the National Computational Infrastructure (NCI), which is also supported by the Australian Government through NCRIS. This research was supported by resources and expertise provided by CSIRO IMT Scientific Computing.

Code availability

The key scripts for the development and operation of Himawari-ANU LST dataset (i.e., ANU_{SZAC}) are publicly available at `https://github.com/yuyi13/Himawari-ANU`, with a permalink registered at Zenodo (DOI will be provided once the manuscript is formally published).

Data availability

The Himawari-ANU LST dataset (i.e., ANU_{SZAC}) is publicly available from the TERN Data Discovery Portal (DOI) and NCI Data Catalogue (DOI will be provided once the manuscript is formally published).

References

Allen, R. G., Pereira, L. S., Raes, D. and Smith, M., 1998. *Crop evapotranspiration - Guidelines for computing crop water requirements - FAO Irrigation and drainage paper 56,* Food and Agriculture Organization of the United Nations, Rome. Available at: https://www.fao.org/3/x0490e/x0490e00.htm [Accessed 11/Sep/2023].

Atitar, M. and Sobrino, J. A., 2008. A split-window algorithm for estimating LST from Meteosat 9 data: Test and comparison with in situ data and MODIS LSTs. *IEEE Geosci. Remote Sens.,6* , 122-126. https://doi.org/10.1109/LGRS.2008.2006410.

Azarderakhsh, M., Prakash, S., Zhao, Y. and AghaKouchak, A., 2020. Satellite-Based Analysis of Extreme Land Surface Temperatures and Diurnal Variability Across the Hottest Place on Earth. *IEEE Geosci. Remote Sens., 17* , 2025-2029. https://doi.org./10.1109/LGRS.2019.2962055.

Barton, I. J., Zavody, A. M., O'Brien, D. M., Cutten, D. R., Saunders, R. W. and Llewellyn-Jones, D. T., 1989. Theoretical algorithms for satellite-derived sea surface temperatures. *J. Geophys. Res. Atmos., 94* , 3365-3375. https://doi.org/10.1029/JD094iD03p03365.

Beringer, J., Hutley, L. B., McHugh, I., Arndt, S. K., Campbell, D., Cleugh, H. A., Cleverly, J., Resco de Dios, V., Eamus, D. and Evans, B., 2016. An introduction to the Australian and New Zealand flux tower network - OzFlux. *Biogeosciences, 13* , 5895-5916. https://doi.org/10.5194/bg-13-5895-2016.

Bessho, K., Date, K., Hayashi, M., Ikeda, A., Imai, T., Inoue, H., Kumagai, Y., Miyakawa, T., Murata, H. and Ohno, T., 2016. An introduction to Himawari-8/9 - Japan's new-generation geostationary meteorological satellites. *J. Meteorol. Soc. Jpn. Ser. II,94* , 151-183. https://doi.org/10.2151/jmsj.2016-009.

Brent, R. P., 2013. *Algorithms for Minimization Without Derivatives,* Dover Publications, Canberra. Available at: https://books.google.com.au/books?id=AITCAgAAQBAJ [Accessed 25/Aug/2023].

Bureau of Meteorology, 2021. *Bureau of Meteorology Satellite Observations (Collection)* . NCI Australia, Canberra. https://doi.org/10.25914/61A609F9E7FFA.

Cao, B., Liu, Q., Du, Y., Roujean, J.-L., Gastellu-Etchegorry, J.-P., Trigo, I. F., Zhan, W., Yu, Y., Cheng, J., Jacob, F., Lagouarde, J.-P., Bian, Z., Li, H., Hu, T. and Xiao, Q., 2019. A review of earth surface thermal radiation directionality observing and modeling: Historical development, current status and perspectives. *Remote Sens. Environ., 232* , 111304. https://doi.org/10.1016/j.rse.2019.111304.

Chu, H., Luo, X., Ouyang, Z., Chan, W. S., Dengel, S., Biraud, S. C., Torn, M. S., Metzger, S., Kumar, J. and Arain, M. A., 2021. Representativeness of Eddy-Covariance flux footprints for areas surrounding AmeriFlux sites. *Agric. For. Meteorol.,301* , 108350. https://doi.org/10.1016/j.agrformet.2021.108350.

Coll, C., Caselles, V., Sobrino, J. A. and Valor, E., 1994. On the atmospheric dependence of the split-window equation for land surface temperature. *Int. J. Remote Sens., 15* , 105-122. https://doi.org/10.1080/01431169408954054.

Cresswell, M., Morse, A., Thomson, M. and Connor, S., 1999. Estimating surface air temperatures, from Meteosat land surface temperatures, using an empirical solar zenith angle model. *Int. J. Remote Sens.,20* , 1125-1132. https://doi.org/10.1080/014311699212885.

DCCEEW, 2020. *Interim Biogeographic Regionalisation (IBRA) for Australia v. 7* . Australian Government Department of Climate Change, Energy, the Environment and Water, Canberra. Available at: https://www.dcceew.gov.au/environment/land/nrs/science/ibra [Accessed 14/Nov/2023].

Di Napoli, C., Barnard, C., Prudhomme, C., Cloke, H. L. and Pappenberger, F., 2021. ERA5-HEAT: A global gridded historical dataset of human thermal comfort indices from climate reanalysis. *Geosci. Data J., 8* , 2-10. https://doi.org/10.1002/gdj3.102.

Di Napoli, C., Pappenberger, F. and Cloke, H. L., 2019. Verification of Heat Stress Thresholds for a Health-Based Heat-Wave Definition. *J. Appl. Meteorol. Climatol., 58* , 1177-1194. https://doi.org/10.1175/JAMC-D-18-0246.1.

Duan, S.-B., Li, Z.-L., Tang, B.-H., Wu, H. and Tang, R., 2014. Generation of a time-consistent land surface temperature product from MODIS data. *Remote Sens. Environ., 140* , 339-349. https://doi.org/10.1016/j.rse.2013.09.003.

Duan, S.-B., Li, Z.-L., Wang, N., Wu, H. and Tang, B.-H., 2012. Evaluation of six land-surface diurnal temperature cycle models using clear-sky in situ and satellite data. *Remote Sens. Environ.,124* , 15-25. https://doi.org/10.1016/j.rse.2012.04.016.

Ekinzog, E. K., Schlerf, M., Kraft, M., Werner, F., Riedel, A., Rock, G. and Mallick, K., 2022. Revisiting crop water stress index based on potato field experiments in Northern Germany. *Agric. Water Manag., 269* , 107664. https://doi.org/10.1016/j.agwat.2022.107664.

Ermida, S. L., DaCamara, C. C., Trigo, I. F., Pires, A. C., Ghent, D. and Remedios, J., 2017. Modelling directional effects on remotely sensed land surface temperature. *Remote Sens. Environ.,190* , 56-69. https://doi.org/10.1016/j.rse.2016.12.008.

Ermida, S. L., Trigo, I. F., DaCamara, C. C. and Roujean, J.-L., 2018. Assessing the potential of parametric models to correct directional effects on local to global remotely sensed LST. *Remote Sens. Environ., 209* , 410-422. https://doi.org/10.1016/j.rse.2018.02.066.

Eytan, E., Koren, I., Altaratz, O., Kostinski, A. B. and Ronen, A., 2020. Longwave radiative effect of the cloud twilight zone. *Nat. Geosci., 13* , 669-673. https://doi.org/10.1038/s41561-020-0636-8.

Fisher, J. B., Lee, B., Purdy, A. J., Halverson, G. H., Dohlen, M. B., Cawse-Nicholson, K., Wang, A., Anderson, R. G., Aragon, B. and Arain, M. A., 2020. ECOSTRESS: NASA's next generation mission to measure evapotranspiration from the international space station. *Water Resour. Res., 56* , e2019WR026058. https://doi.org/10.1029/2019WR026058.

Freitas, S. C., Trigo, I. F., Macedo, J., Barroso, C., Silva, R. and Perdigao, R., 2013. Land surface temperature from multiple geostationary satellites. *Int. J. Remote Sens., 34* , 3051-3068. https://doi.org/10.1080/01431161.2012.716925.

Gillespie, A., Rokugawa, S., Matsunaga, T., Cothern, J. S., Hook, S. and Kahle, A. B., 1998. A temperature and emissivity separation algorithm for Advanced Spaceborne Thermal Emission and Reflection Radiometer (ASTER) images. *IEEE Trans. Geosci. Remote Sens.,36* , 1113-1126. https://doi.org/10.1109/36.700995.

Guillevic, P. C., Bork-Unkelbach, A., Gottsche, F. M., Hulley, G., Gastellu-Etchegorry, J. P., Olesen, F. S. and Privette, J. L., 2013. Directional Viewing Effects on Satellite Land Surface Temperature Products Over Sparse Vegetation Canopies—A Multisensor Analysis.*IEEE Geosci. Remote Sens., 10* , 1464-1468. https://doi.org/10.1109/LGRS.2013.2260319.

Hersbach, H., Bell, B., Berrisford, P., Hirahara, S., Horanyi, A., Munoz-Sabater, J., Nicolas, J., Peubey, C., Radu, R., Schepers, D., Simmons, A., Soci, C., Abdalla, S., Abellan, X., Balsamo, G., Bechtold, P., Biavati, G., Bidlot, J., Bonavita, M., De Chiara, G., Dahlgren, P., Dee, D., Diamantakis, M., Dragani, R., Flemming, J., Forbes, R., Fuentes, M., Geer, A., Haimberger, L., Healy, S., Hogan, R. J., Holm, E., Janiskova, M., Keeley, S., Laloyaux, P., Lopez, P., Lupu, C., Radnoti, G., de Rosnay, P., Rozum, I., Vamborg, F., Villaume, S. and Thepaut, J.-N., 2020. The ERA5 global reanalysis. *Q. J. R. Meteorol. Soc., 146* , 1999-2049. https://doi.org/10.1002/qj.3803.

Holmes, T. R. H., Crow, W. T., Hain, C., Anderson, M. C. and Kustas, W. P., 2015. Diurnal temperature cycle as observed by thermal infrared and microwave radiometers. *Remote Sens. Environ.,158* , 110-125. https://doi.org/10.1016/j.rse.2014.10.031.

Hook, S. J., Gabell, A. R., Green, A. A. and Kealy, P. S., 1992. A comparison of techniques for extracting emissivity information from thermal infrared data for geologic studies. *Remote Sens. Environ., 42* , 123-135. https://doi.org/10.1016/0034-4257(92)90096-3.

Hu, L., Brunsell, N. A., Monaghan, A. J., Barlage, M. and Wilhelmi, O. V., 2014. How can we use MODIS land surface temperature to validate long-term urban model simulations? *J. Geophys. Res. Atmos.,119* , 3185-3201. https://doi.org/10.1002/2013JD021101.

Hu, L., Monaghan, A., Voogt, J. A. and Barlage, M., 2016. A first satellite-based observational assessment of urban thermal anisotropy.*Remote Sens. Environ., 181* , 111-121. https://doi.org/10.1016/j.rse.2016.03.043.

Hu, L., Sun, Y., Collins, G. and Fu, P., 2020a. Improved estimates of monthly land surface temperature from MODIS using a diurnal temperature cycle (DTC) model. *ISPRS J. Photogramm. Remote Sens.,168* , 131-140. https://doi.org/10.1016/j.isprsjprs.2020.08.007.

Hu, T., Renzullo, L. J., van Dijk, A. I. J. M., He, J., Tian, S., Xu, Z., Zhou, J., Liu, T. and Liu, Q., 2020b. Monitoring agricultural drought in Australia using MTSAT-2 land surface temperature retrievals.*Remote Sens. Environ., 236* , 111419. https://doi.org/10.1016/j.rse.2019.111419.

Huete, A., Didan, K., Miura, T., Rodriguez, E. P., Gao, X. and Ferreira, L. G., 2002. Overview of the radiometric and biophysical performance of the MODIS vegetation indices. *Remote Sens. Environ.,83* , 195-213. https://doi.org/10.1016/S0034-4257(02)00096-2.

Hulley, G. C., Malakar, N. K., Islam, T. and Freepartner, R. J., 2017. NASA's MODIS and VIIRS land surface temperature and emissivity products: A long-term and consistent earth system data record. *IEEE J. Sel. Top. Appl. Earth Obs. Remote Sens., 11* , 522-535. https://doi.org/10.1109/JSTARS.2017.2779330.

Islam, T., Hulley, G. C., Malakar, N. K., Radocinski, R. G., Guillevic, P. C. and Hook, S. J., 2016. A physics-based algorithm for the simultaneous retrieval of land surface temperature and emissivity from VIIRS thermal infrared data. *IEEE Trans. Geosci. Remote Sens.,55* , 563-576. https://doi.org/10.1109/TGRS.2016.2611566.

Jiang, L., Zhan, W., Hu, L., Huang, F., Hong, F., Liu, Z., Lai, J. and Wang, C., 2021. Assessment of different kernel-driven models for daytime urban thermal radiation directionality simulation. *Remote Sens. Environ., 263* , 112562. https://doi.org/10.1016/j.rse.2021.112562.

Jimenez-Munoz, J. C., Sobrino, J. A., Mattar, C. and Malhi, Y., 2013. Spatial and temporal patterns of the recent warming of the Amazon forest. *J. Geophys. Res. Atmos., 118* , 5204-5215. https://doi.org/10.1002/jgrd.50456.

Justice, C. O., Vermote, E., Townshend, J. R. G., Defries, R., Roy, D. P., Hall, D. K., Salomonson, V. V., Privette, J. L., Riggs, G., Strahler, A., Lucht, W., Myneni, R. B., Knyazikhin, Y., Running, S. W., Nemani, R. R., Zhengming, W., Huete, A. R., Leeuwen, W. v., Wolfe, R. E., Giglio, L., Muller, J., Lewis, P. and Barnsley, M. J., 1998. The Moderate Resolution Imaging Spectroradiometer (MODIS): land remote sensing for global change research. *IEEE Trans. Geosci. Remote Sens., 36* , 1228-1249. https://doi.org/10.1109/36.701075.

Kerr, Y. H., Lagouarde, J. P. and Imbernon, J., 1992. Accurate land surface temperature retrieval from AVHRR data with use of an improved split window algorithm. *Remote Sens. Environ.,41* , 197-209. https://doi.org/10.1016/0034-4257(92)90078-X.

Kurihara, Y., Murakami, H. and Kachi, M., 2016. Sea surface temperature from the new Japanese geostationary meteorological Himawari-8 satellite. *Geophys. Res. Lett., 43* , 1234-1240. https://doi.org/10.1002/2015GL067159.

Li, H., Sun, D., Yu, Y., Wang, H., Liu, Y., Liu, Q., Du, Y., Wang, H. and Cao, B., 2014. Evaluation of the VIIRS and MODIS LST products in an arid area of Northwest China. *Remote Sens. Environ.,142* , 111-121. https://doi.org/10.1016/j.rse.2013.11.014.

Li, K., Guan, K., Jiang, C., Wang, S., Peng, B. and Cai, Y., 2021. Evaluation of four new Land Surface Temperature (LST) products in the US corn belt: ECOSTRESS, GOES-R, Landsat, and Sentinel-3. *IEEE J. Sel. Top. Appl. Earth Obs. Remote Sens., 14* , 9931-9945. https://doi.org/10.1109/JSTARS.2021.3114613.

Li, R., Li, H., Sun, L., Yang, Y., Hu, T., Bian, Z., Cao, B., Du, Y. and Liu, Q., 2020. An operational split-window algorithm for retrieving land surface temperature from geostationary satellite data: A case study on Himawari-8 AHI data. *Remote Sens., 12* , 2613. https://doi.org/10.3390/rs12162613.

Li, Z.-L., Tang, B.-H., Wu, H., Ren, H., Yan, G., Wan, Z., Trigo, I. F. and Sobrino, J. A., 2013. Satellite-derived land surface temperature: Current status and perspectives. *Remote Sens. Environ.,131* , 14-37. https://doi.org/10.1016/j.rse.2012.12.008.

Liu, J., Schaaf, C., Strahler, A., Jiao, Z., Shuai, Y., Zhang, Q., Roman, M., Augustine, J. A. and Dutton, E. G., 2009. Validation of Moderate Resolution Imaging Spectroradiometer (MODIS) albedo retrieval algorithm: Dependence of albedo on solar zenith angle. *J. Geophys. Res. Atmos., 114* . https://doi.org/10.1029/2008JD009969.

Lu, L. and Zhou, X., 2021. A Four-Parameter Model for Estimating Diurnal Temperature Cycle From MODIS Land Surface Temperature Product. *J. Geophys. Res. Atmos., 126* , e2020JD033855. https://doi.org/10.1029/2020JD033855.

Lymburner, L., Tan, P., McIntyre, A., Thankappan, M. and Sixsmith, J., 2015. *Dynamic land cover dataset version 2.1 [Dataset]* . Geoscience Australia, Canberra. Available at: http://pid.geoscience.gov.au/dataset/ga/83868 [Accessed 20/Mar/2023].

Myneni, R. B., Hoffman, S., Knyazikhin, Y., Privette, J. L., Glassy, J., Tian, Y., Wang, Y., Song, X., Zhang, Y., Smith, G. R., Lotsch, A., Friedl, M., Morisette, J. T., Votava, P., Nemani, R. R. and Running, S. W., 2002. Global products of vegetation leaf area and fraction absorbed PAR from year one of MODIS data. *Remote Sens. Environ.,83* **,** 214-231. https://doi.org/10.1016/S0034-4257(02)00074-3.

Niclos, R., Caselles, V., Coll, C. and Valor, E., 2007. Determination of sea surface temperature at large observation angles using an angular and emissivity-dependent split-window equation. *Remote Sens. Environ., 111* **,** 107-121. https://doi.org/10.1016/j.rse.2007.03.014.

Perez-Planells, L., Ghent, D., Ermida, S., Martin, M. and Gottsche, F.-M., 2023. Retrieval Consistency between LST CCI Satellite Data Products over Europe and Africa. *Remote Sens.,15* **,** 3281. https://doi.org/10.3390/rs15133281.

Price, J. C., 1984. Land surface temperature measurements from the split window channels of the NOAA 7 Advanced Very High Resolution Radiometer.*J. Geophys. Res. Atmos., 89* **,** 7231-7237. https://doi.org/10.1029/JD089iD05p07231.

Qin, Y., McVicar, T. R., Huang, J., West, S. and Steven, A. D. L., 2022. On the validity of using ground-based observations to validate geostationary-satellite-derived direct and diffuse surface solar irradiance: Quantifying the spatial mismatch and temporal averaging issues. *Remote Sens. Environ., 280* **,** 113179. https://doi.org/10.1016/j.rse.2022.113179.

Schaaf, C. B., Gao, F., Strahler, A. H., Lucht, W., Li, X., Tsang, T., Strugnell, N. C., Zhang, X., Jin, Y., Muller, J.-P., Lewis, P., Barnsley, M., Hobson, P., Disney, M., Roberts, G., Dunderdale, M., Doll, C., d'Entremont, R. P., Hu, B., Liang, S., Privette, J. L. and Roy, D., 2002. First operational BRDF, albedo nadir reflectance products from MODIS. *Remote Sens. Environ., 83* **,** 135-148. https://doi.org/10.1016/S0034-4257(02)00091-3.

Schmetz, J., Pili, P., Tjemkes, S., Just, D., Kerkmann, J., Rota, S. and Ratier, A., 2002. An introduction to Meteosat second generation (MSG).*Bull. Am. Meteorol. Soc., 83* **,** 977-992. https://doi.org/10.1175/1520-0477(2002)083%3C0977:AITMSG%3E2.3.CO;2.

Schmit, T. J., Gunshor, M. M., Menzel, W. P., Gurka, J. J., Li, J. and Bachmeier, A. S., 2005. Introducing the next-generation Advanced Baseline Imager on GOES-R. *Bull. Am. Meteorol. Soc.,86* **,** 1079-1096. https://doi.org/10.1175/BAMS-86-8-1079.

Schmit, T. J., Li, J., Li, J., Feltz, W. F., Gurka, J. J., Goldberg, M. D. and Schrab, K. J., 2008. The GOES-R Advanced Baseline Imager and the continuation of current sounder products. *J. Appl. Meteorol. Climatol., 47* **,** 2696-2711. https://doi.org/10.1175/2008JAMC1858.1.

Seemann, S. W., Borbas, E. E., Knuteson, R. O., Stephenson, G. R. and Huang, H.-L., 2008. Development of a global infrared land surface emissivity database for application to clear sky sounding retrievals from multispectral satellite radiance measurements. *J. Appl. Meteorol. Climatol., 47* **,** 108-123. https://doi.org/10.1175/2007JAMC1590.1.

Sekertekin, A., Kutoglu, S. H. and Kaya, S., 2016. Evaluation of spatio-temporal variability in Land Surface Temperature: A case study of Zonguldak, Turkey. *Environ. Monit. Assess., 188* **,**1-15. https://doi.org/10.1007/s10661-015-5032-2.

Semmens, K. A., Anderson, M. C., Kustas, W. P., Gao, F., Alfieri, J. G., McKee, L., Prueger, J. H., Hain, C. R., Cammalleri, C. and Yang, Y., 2016. Monitoring daily evapotranspiration over two California vineyards using Landsat 8 in a multi-sensor data fusion approach. *Remote Sens. Environ., 185* **,** 155-170. https://doi.org/10.1016/j.rse.2015.10.025.

Sharifnezhadazizi, Z., Norouzi, H., Prakash, S., Beale, C. and Khanbilvardi, R., 2019. A Global Analysis of Land Surface Temperature Diurnal Cycle Using MODIS Observations. *J. Appl. Meteorol. Climatol., 58* , 1279-1291. https://doi.org/10.1175/JAMC-D-18-0256.1.

Singh, R., Singh, C., Ojha, S. P., Kumar, A. S., Kishtawal, C. M. and Kumar, A. S. K., 2016. Land surface temperature from INSAT-3D imager data: Retrieval and assimilation in NWP model. *J. Geophys. Res. Atmos., 121* , 6909-6926. https://doi.org/10.1002/2016JD024752.

Sobrino, J. A. and Jimenez-Munoz, J. C., 2005. Land surface temperature retrieval from thermal infrared data: An assessment in the context of the Surface Processes and Ecosystem Changes Through Response Analysis (SPECTRA) mission. *J. Geophys. Res. Atmos., 110* . https://doi.org/10.1029/2004JD005588.

Sobrino, J. A., Jimenez-Munoz, J. C. and Paolini, L., 2004. Land surface temperature retrieval from LANDSAT TM 5. *Remote Sens. Environ.,90* , 434-440. https://doi.org/10.1016/j.rse.2004.02.003.

Trebs, I., Mallick, K., Bhattarai, N., Sulis, M., Cleverly, J., Woodgate, W., Silberstein, R., Hinko-Najera, N., Beringer, J., Meyer, W. S., Su, Z. and Boulet, G., 2021. The role of aerodynamic resistance in thermal remote sensing-based evapotranspiration models. *Remote Sens. Environ., 264* , 112602. https://doi.org/10.1016/j.rse.2021.112602.

Trigo, I. F., Ermida, S. L., Martins, J. P., Gouveia, C. M., Gottsche, F.-M. and Freitas, S. C., 2021. Validation and consistency assessment of land surface temperature from geostationary and polar orbit platforms: SEVIRI/MSG and AVHRR/Metop. *ISPRS J. Photogramm. Remote Sens.,175* , 282-297. https://doi.org/10.1016/j.isprsjprs.2021.03.013.

Uspenskii, A. B., Kukharskii, A. V. and Uspenskii, S. A., 2015. Validation of the results of the satellite monitoring of land surface temperature. *Russ. Meteorol. Hydrol., 40* ,131-140. https://doi.org/10.3103/S1068373915020107.

Van De Kerchove, R., Lhermitte, S., Veraverbeke, S. and Goossens, R., 2013. Spatio-temporal variability in remotely sensed land surface temperature, and its relationship with physiographic variables in the Russian Altay Mountains. *Int. J. Appl. Earth Obs. Geoinf.,20* , 4-19. https://doi.org/10.1016/j.jag.2011.09.007.

Vanos, J. K., Rykaczewski, K., Middel, A., Vecellio, D. J., Brown, R. D. and Gillespie, T. J., 2021. Improved methods for estimating mean radiant temperature in hot and sunny outdoor settings. *Int. J. Biometeorol., 65* , 967-983. https://doi.org/10.1007/s00484-021-02131-y.

Vinnikov, K. Y., Yu, Y., Goldberg, M. D., Tarpley, D., Romanov, P., Laszlo, I. and Chen, M., 2012. Angular anisotropy of satellite observations of land surface temperature. *Geophys. Res. Lett.,39* . https://doi.org/10.1029/2012GL054059.

Vinnikov, K. Y., Yu, Y., Rama Varma Raja, M. K., Tarpley, D. and Goldberg, M. D., 2008. Diurnal-seasonal and weather-related variations of land surface temperature observed from geostationary satellites. *Geophys. Res. Lett., 35* . https://doi.org/10.1029/2008GL035759.

Wan, Z., 2013. *Collection-6 MODIS Land Surface Temperature Products Users' Guide* . NASA LP DAAC. Available at: https://lpdaac.usgs.gov/documents/118/MOD11_User_Guide_V6.pdf [Accessed 08/Oct/2023].

Wan, Z., 2014. New refinements and validation of the collection-6 MODIS land-surface temperature/emissivity product. *Remote Sens. Environ., 140* , 36-45. https://doi.org/10.1016/j.rse.2013.08.027.

Wan, Z. and Dozier, J., 1996. A generalized split-window algorithm for retrieving land-surface temperature from space. *IEEE Trans. Geosci. Remote Sens., 34* , 892-905. https://doi.org/10.1109/36.508406.

Wan, Z. and Li, Z.-L., 1997. A physics-based algorithm for retrieving land-surface emissivity and temperature from EOS/MODIS data. *IEEE Trans. Geosci. Remote Sens., 35* , 980-996. https://doi.org/10.1109/36.602541.

Wang, J., Tang, R., Jiang, Y., Liu, M. and Li, Z.-L., 2023. A practical method for angular normalization of global MODIS land surface temperature over vegetated surfaces. *ISPRS J. Photogramm. Remote Sens., 199* , 289-304. https://doi.org/10.1016/j.isprsjprs.2023.04.015.

Wang, K. and Liang, S., 2009. Evaluation of ASTER and MODIS land surface temperature and emissivity products using long-term surface longwave radiation observations at SURFRAD sites. *Remote Sens. Environ.,113* , 1556-1565. https://doi.org/10.1016/j.rse.2009.03.009.

Wilson, A. M. and Jetz, W., 2016. Remotely Sensed High-Resolution Global Cloud Dynamics for Predicting Ecosystem and Biodiversity Distributions.*PLOS Biol., 14* , e1002415. https://doi.org/10.1371/journal.pbio.1002415.

Wu, A., Xiong, X., Doelling, D. R., Morstad, D., Angal, A. and Bhatt, R., 2013. Characterization of Terra and Aqua MODIS VIS, NIR, and SWIR Spectral Bands' Calibration Stability. *IEEE Trans. Geosci. Remote Sens., 51* , 4330-4338. https://doi.org/10.1109/TGRS.2012.2226588.

Yamamoto, Y., Ichii, K., Ryu, Y., Kang, M. and Murayama, S., 2022. Uncertainty quantification in land surface temperature retrieved from Himawari-8/AHI data by operational algorithms. *ISPRS J. Photogramm. Remote Sens., 191* , 171-187. https://doi.org/10.1016/j.isprsjprs.2022.07.008.

Yamamoto, Y., Ichii, K., Ryu, Y., Kang, M., Murayama, S., Kim, S.-J. and Cleverly, J. R., 2023. Detection of vegetation drying signals using diurnal variation of land surface temperature: Application to the 2018 East Asia heatwave. *Remote Sens. Environ., 291* ,113572. https://doi.org/10.1016/j.rse.2023.113572.

Yamamoto, Y. and Ishikawa, H., 2018. Thermal land surface emissivity for retrieving land surface temperature from Himawari-8. *J. Meteorol. Soc. Jpn. Ser. II, 96B* , 43-58. https://doi.org/10.2151/jmsj.2018-004.

Yamamoto, Y., Ishikawa, H., Oku, Y. and Hu, Z., 2018. An Algorithm for Land Surface Temperature Retrieval Using Three Thermal Infrared Bands of Himawari-8. *J. Meteorol. Soc. Jpn. Ser. II, 96B* ,59-76. https://doi.org/10.2151/jmsj.2018-005.

Yang, J., Zhang, Z., Wei, C., Lu, F. and Guo, Q., 2017. Introducing the new generation of Chinese geostationary weather satellites, Fengyun-4.*Bull. Am. Meteorol. Soc., 98* , 1637-1658. https://doi.org/10.1175/BAMS-D-16-0065.1.

Yeom, J.-M., Han, K.-S. and Kim, J.-J., 2012. Evaluation on penetration rate of cloud for incoming solar radiation using geostationary satellite data. *Asia-Pac. J. Atmospheric Sci., 48* , 115-123. https://doi.org/10.1007/s13143-012-0011-9.

Yu, Y., Privette, J. L. and Pinheiro, A. C., 2007. Evaluation of split-window land surface temperature algorithms for generating climate data records. *IEEE Trans. Geosci. Remote Sens.,46* , 179-192. https://doi.org/10.1109/TGRS.2007.909097.

Yu, Y., Renzullo, L. J., McVicar, T. R., Malone, B. P. and Tian, S., 2023. Generating daily 100 m resolution land surface temperature estimates continentally using an unbiased spatiotemporal fusion approach. *Remote Sens. Environ., 297* , 113784. https://doi.org/10.1016/j.rse.2023.113784.

Yu, Y., Tarpley, D., Privette, J. L., Flynn, L. E., Xu, H., Chen, M., Vinnikov, K. Y., Sun, D. and Tian, Y., 2012. Validation of GOES-R Satellite Land Surface Temperature Algorithm Using SURFRAD Ground Measurements and Statistical Estimates of Error Properties. *IEEE Trans. Geosci. Remote Sens., 50* , 704-713. https://doi.org/10.1109/TGRS.2011.2162338.

Yu, Y., Tarpley, D., Privette, J. L., Goldberg, M. D., Raja, M. K. R. V., Vinnikov, K. Y. and Xu, H., 2009. Developing Algorithm for Operational GOES-R Land Surface Temperature Product. *IEEE Trans. Geosci. Remote Sens., 47* , 936-951. https://doi.org/10.1109/TGRS.2008.2006180.

Zhang, L., Jiao, W., Zhang, H., Huang, C. and Tong, Q., 2017. Studying drought phenomena in the Continental United States in 2011 and 2012 using various drought indices. *Remote Sens. Environ.,190* , 96-106. https://doi.org/10.1016/j.rse.2016.12.010.

Zhao, W., Wu, H., Yin, G. and Duan, S.-B., 2019. Normalization of the temporal effect on the MODIS land surface temperature product using random forest regression. *ISPRS J. Photogramm. Remote Sens.,152* , 109-118. https://doi.org/10.1016/j.isprsjprs.2019.04.008.

Solar zenith angle-based calibration of Himawari-8 land surface temperature based on MODIS spatiotemporal characteristics

Yi Yu [a,b,*], Luigi J. Renzullo [a,c], Tim R. McVicar [d], Thomas G. Van Niel [e], Dejun Cai [d], Siyuan Tian [a,c] and Yichuan Ma [d,f]

[a] Fenner School of Environment & Society, The Australian National University, Canberra, ACT 2601, Australia

[b] CSIRO Agriculture and Food, Canberra, ACT 2601, Australia

[c] Bureau of Meteorology, Canberra, ACT 2600, Australia

[d] CSIRO Environment, Canberra, ACT 2601, Australia

[e] CSIRO Environment, Wembley, WA 6913, Australia

[f] Hubei Key Laboratory of Quantitative Remote Sensing of Land and Atmosphere, School of Remote Sensing and Information Engineering, Wuhan University, Wuhan 430079, China

* Correspondence to Yi Yu (u6726739@anu.edu.au)

Abstract

The geostationary Himawari-8 satellite offers a unique opportunity to monitor sub-daily thermal dynamics over Asia and Oceania, and several operational land surface temperature (LST) retrieval algorithms have been developed for this purpose. However, studies have reported inconsistency between LST data obtained from geostationary and polar-orbiting platforms, particularly for daytime LST, which usually shows directional artefacts and can be strongly impacted by viewing and illumination geometries and shadowing effects. To overcome this challenge, Solar Zenith Angle (SZA) serves as an ideal physical variable to quantify systematic differences between platforms. Here we presented an SZA-based Calibration (SZAC) method to operationally calibrate the daytime component of a split-window retrieved Himawari-8 LST (referred to here as the baseline). SZAC describes the spatial heterogeneity and magnitude of diurnal LST discrepancies from different products. The SZAC coefficient was spatiotemporally optimised against highest-quality assured (error < 1 K) pixels from the MODerate-resolution Imaging Spectroradiometer (MODIS) daytime LST between 01/Jan/2016 and 31/Dec/2020. We evaluated the calibrated LST data, referred to as the Australian National University LST with SZAC (ANU_{SZAC}), against MODIS LST and the Visible Infrared Imaging Radiometer Suite (VIIRS) LST, as well as *in-situ* LST from the OzFlux network. Two peer Himawari-8 LST products from Chiba University and the Copernicus Global Land Service were also collected for comparisons. The median daytime bias of ANU_{SZAC} LST against Terra-MODIS LST, Aqua-MODIS LST and VIIRS LST was 1.52 K, 0.98 K and -0.63 K, respectively, which demonstrated improved performance compared to baseline (5.37 K, 4.85 K and 3.02 K, respectively) and Chiba LST (3.71 K, 2.90 K and 1.07 K, respectively). All four Himawari-8 LST products showed comparable performance of unbiased root mean squared error (ubRMSE), ranging from 2.47 to 3.07 K, compared to LST from polar-orbiting platforms. In the evaluation against *in-situ* LST, the overall mean values of bias (ubRMSE) of baseline, Chiba, Copernicus and ANU_{SZAC} LST during daytime were 4.23 K (3.74 K), 2.16 K (3.62 K), 1.73 K (3.31 K) and 1.41 K (3.24 K), respectively, based on 171,289 hourly samples from 20 OzFlux sites across Australia between 01/Jan/2016 and 31/Dec/2020. In summary, the SZAC method offers a promising approach to enhance the reliability of geostationary LST retrievals by incorporating the spatiotemporal characteristics observed by accurate polar-orbiting LST data. Furthermore, it is possible to extend SZAC for LST estimation by using data acquired by geostationary satellites in other regions, e.g., Europe, Africa and Americas, as this could improve our understanding of the error characteristics of overlapped geostationary imageries, allowing for targeted refinements and calibrations to further enhance applicability.

Keywords

Land surface temperature; Geostationary; Himawari-8; Diurnal temperature cycle; Calibration; Solar zenith angle; MODIS; VIIRS

1. Introduction

Land surface temperature (LST) plays an important role in the Earth's surface energy budget, and is widely used in hydrology, meteorology and climatology (Li et al., 2013; Cao et al., 2019). LST undergoes rapid fluctuations over time, exhibiting distinct diurnal and seasonal patterns. The increasing quantity of LST observations obtained from various satellite missions has been important to comprehend the spatiotemporal dynamics of longwave radiation (Hu et al., 2020a). Such observations have been utilised in numerous scientific fields, including but not limited to agriculture (e.g., Ekinzog et al., 2022), drought monitoring (e.g., Zhang et al., 2017; Hu et al., 2020b), evapotranspiration estimation (e.g., Semmens et al., 2016) and ecology (e.g., Jiménez-Muñoz et al., 2013).

Remotely sensed LST can be routinely retrieved using data provided by polar-orbiting and geostationary satellite missions (Yu et al., 2009). Some well-known polar-orbiting platforms that provide LST retrievals include the Advanced Very High Resolution Radiometer (AVHRR; Kerr et al., 1992), the MODerate-resolution Imaging Spectroradiometer (MODIS; Wan and Li, 1997), the Advanced Spaceborne Thermal Emission and Reflection Radiometer (ASTER; Gillespie et al., 1998) and the Visible Infrared Imaging Radiometer Suite (VIIRS; Islam et al., 2016). They have a global coverage and relatively fine spatial resolution (e.g., 1 km for MODIS and VIIRS) but low temporal frequency, e.g., 4 times per day maximum for MODIS (less when considering cloud; Wilson and Jetz, 2016). As a comparison, geostationary platforms acquire LST over the complete diurnal cycle, with so-called ‘new generation’ geostationary instruments acquiring imagery at sub-hourly frequency (e.g., every 10 or 15 minutes), but with relatively coarse spatial resolution (usually equivalent to, or coarser than, 2 km). Examples of geostationary satellites include Himawari-8 (Bessho et al., 2016), the Geostationary Operational Environmental Satellite (GOES-R; Schmit et al., 2008), the Meteosat Second Generation (MSG; Schmetz et al., 2002), the Feng Yun meteorological satellites (FY-4A; Yang et al., 2017), the Indian National Satellite (INSAT-3D; Singh et al., 2016) and the Russian meteorological satellites (Elektro-L; Uspenskii et al., 2015). However, each geostationary satellite only observes a longitudinally defined hemisphere. To overcome this limitation, Freitas et al. (2013) fused data from multiple geostationary satellites to generate a global-coverage LST product with hourly frequency, known as the Copernicus Global Land Service (CGLS) project, but with a spatial resolution that is coarser than the individually retrieved geostationary LST products.

Over the past decades, there have been marked efforts to develop LST retrieval algorithms (Wan and Dozier, 1996; Sobrino et al., 2004; Yamamoto et al., 2018). Provided that land surface emissivity (LSE) is known *a priori*, the retrieval algorithms can be mainly classified by three categories, including (i) single-channel methods; (ii) multi-channel methods; and (iii) multi-angle methods (Li et al., 2013). Firstly, the single channel method, alternatively known as the model emissivity method (Hook et al., 1992), utilises radiance measured by the sensor in a single thermal infrared channel. An accurate estimation of LST through this approach requires a high-fidelity atmospheric transmittance/radiance code, extensive familiarity with the channel LSE, an accurate atmospheric profile, and an appropriate consideration of the topographic impacts (Sobrino et al., 2004). Secondly, due to the inherent challenges in either pre-establishing radiative transfer models or accurately estimating atmospheric profiles, linear split-window (SW) algorithms have been devised for the retrieval of sea surface temperature (SST; Barton et al., 1989; Niclòs et al., 2007). These algorithms leverage data from two adjacent channels centred at ~ 11 and 12 μm. This linear approach serves as a typical multi-channel method and has been subsequently extended to LST studies, which was shown to be highly effective (e.g., Price, 1984; Coll et al., 1994; Wan and Dozier, 1996). Due to the SW algorithm's versatility and compatibility with almost all geostationary sensors, it is a popular choice for geostationary satellite products (Yu et al., 2007; Yu et al., 2009; Freitas et al., 2013; Li et al., 2020), with the exception of GOES 13/15 imagers, which have only one thermal band. Multi-channel methods can also employ nonlinear terms (Atitar and Sobrino,

2008) or utilise more than two adjacent channels (Yamamoto et al., 2018). Thirdly and finally, similar to the underlying principle of the multi-channel method, the multi-angle method relies on differential atmospheric absorption resulting from distinct path-lengths, which occurs when the same object is viewed from varying angles in a particular channel (Sobrino et al., 2004; Li et al., 2013). The outcomes of this method may surpass those of the SW algorithm, provided that the spectral and angular characteristics of LSE are well-determined (Li et al., 2013). However, a crucial concern in the multi-angle method is the angular dependence of LSE as the angular behaviour of natural surfaces (e.g., soils and rocks) is typically not well understood at the spatial scale of satellite observations (Sobrino and Jiménez-Muñoz, 2005). As a result, multi-angle methods are generally limited to homogeneous areas (e.g., sea surface or densely vegetated forests) under optimal atmospheric conditions, hence there has been limited use of multi-channel methods in most scenarios, particularly in heterogeneous environments.

Regardless of the specific retrieval algorithms utilised, studies have reported inconsistencies between LST obtained from geostationary and polar-orbiting missions. Trigo et al. (2021) demonstrated a difference of approximately ±1 K between LST products from the AVHRR sensor onboard Metop polar-orbiting satellites and the Spinning Enhanced Visible and Infrared Imager (SEVIRI) onboard the MSG geostationary platform. Pérez-Planells et al. (2023) reported that Terra- and Aqua-MODIS LST products (i.e., MOD11 and MYD11, respectively) were around 2 K cooler than the LST datasets from the European Space Agency’s Climate Change Initiative (ESA CCI) across all land cover classes. Similarly, Li et al. (2020) found MYD11 LST generally showed lower values than their SW algorithm-retrieved Himawari-8 LST over southeast China and Australia. Comparatively, their product displayed better agreement with MYD21 LST, a successor to MYD11 LST, which Hulley et al. (2017) developed using a Temperature and Emissivity Separation (TES) algorithm. The pronounced discrepancy between MYD11 and MYD21 LST was attributed to the differences in the emissivity calculation methods used in the retrievals (Hulley et al., 2017).

The discrepancy between polar-orbiting and geostationary LST can be particularly high during the daytime (Wang and Liang, 2009; Li et al., 2014; Li et al., 2021; Trigo et al., 2021; Yamamoto et al., 2022), due to variations in viewing and illumination angles (Ermida et al., 2017; Trigo et al., 2021). For example, daytime LST derived from polar-orbiting (i.e., MODIS) and geostationary (i.e., SEVIRI) platforms can have a difference of up to 12 K due to directional effects (Guillevic et al., 2013). This demonstrates that daytime geostationary LST measurements require further recalibration to better align with ground observations. Researchers have directed their investigations towards the conspicuous directional characteristics of LST and have developed correction and harmonisation methodologies, in which the solar zenith angle (SZA) plays a pivotal role (Vinnikov et al., 2012; Ermida et al., 2017; Ermida et al., 2018; Jiang et al., 2021).

SZA represents the angle formed between the Sun's rays and the vertical direction. It is important in various meteorological and climatological calculations, including the determination of radiant temperature (Di Napoli et al., 2019; Vanos et al., 2021), and in the computation of thermal and heat indices such as the Universal Thermal Climate Index (UTCI; Di Napoli et al., 2021). SZA has also found extensive utility in rectifying and harmonising discrepancies in daytime LST acquired from different platforms. Specifically, Vinnikov et al. (2012) introduced an LST anisotropy model that incorporates an SZA-based kernel, representing the influence of directional heterogeneity on observed LST, in conjunction with isotropic and emissivity kernels, which showed improved agreements with ground-based observations. Ermida et al. (2017) calibrated this model against satellite-observed LST acquired at varying viewing angles, and derived spatially varying coefficients for the SZA-based kernel, which encapsulated the characteristics of terrain and vegetation cover. The application of this model ameliorated disparities in LST observed by different satellites, as well as between satellite observations and ground measurements, offering utility to harmonise LST products (Vinnikov et al., 2012; Ermida et al., 2017). Furthermore, Duan et al. (2014) used SZA as a predictor to normalise Terra-MODIS LST during daylight hours, ensuring consistency with local solar time and facilitating the generation of temporally consistent LST products. To normalise the temporal effects of MODIS LST, Zhao et al. (2019) estimated cumulative incident solar radiation by incorporating the cosine value of the SZA, while also considering atmospheric transmittance and path length. Their normalised LST showed reduced uncertainty against MSG-SEVIRI LST. Jiang et al. (2021) compared the performances of 11 kernel-driven models in simulating daytime urban thermal radiation directionality (UTRD), where SZA was used to assess the impact of city latitude and to simulate parametric kernels for UTRD. They found that dual-kernel models achieved a best performance against forward-modelling and satellite data. Wang et al. (2023) also employed the SZA as a key parameter to establish an angular normalisation model to convert MODIS off-nadir LST values to nadir values, which yielded better consistencies with Sentinel-3A nadir LST. As summarised in Table 1, these diverse applications of SZA underscore its effectiveness in rectifying LST discrepancies arising from multiple observational platforms.

Table 1. An overview of studies representing the major types of methods using SZA for LST correction or normalisation. Studies are ordered chronologically by year of publication (oldest to newest). Our study is added for completeness. The following abbreviations are used: AHI (Advanced Himawari Imager); SURFRAD (SURFace RADiation budget observing network); VZA (Viewing Zenith Angle).

Reference	**Satellite platforms**	**Summary of key objective(s)**	**Usage of SZA**	**Key results**	**Potential limitations**
Vinnikov et al. (2012)	GOES-EAST and GOES-WEST	Proposed a statistical model for evaluation and adjustment of angularity of LST.	SZA was used to simulate a solar kernel that represents directional inhomogeneity of LST.	Evaluations against observations from 5 SURFRAD stations showed bias within ±0.5 K and RMSE of 1.2-1.4 K.	All 5 SURFRAD stations are located within limited range of VZA between 43 ° and 66 °. The study also lacked observations of SZA < 10.75 °.
Duan et al. (2014)	Terra-MODIS and MSG-SEVIRI	Proposed a temporal normalisation method of daytime LST.	SZA was used as a regression predictor to estimate the slope of LST versus local solar time.	Difference between Terra-MODIS and MSG-SEVIRI LST reduced from ~ 1.5 K to ~ 0.5 K after normalisation.	The regression was established using data from only 4 months (January, April, July, and October) in 2010. No ground-based evaluations were performed.
Ermida et al. (2017)	Terra-, Aqua-MODIS and MSG-SEVIRI	Calibrated Vinnikov et al. (2012) model with LST acquired at different view angles to characterise LST anisotropy.	Same with Vinnikov et al. (2012).	Cross-validation showed the RMSE between SEVIRI and MODIS daytime (nighttime) reduced from 3.5 K (1.5 K) to 2.3 K (1.3 K). Evaluations against *in-situ* daytime LST showed a	Seasonal variations of vegetation-shaded fraction may impact the values of SZA-based kernel but was not considered. There was no observation of azimuth angles from north but was expected to

Reference	Satellite platforms	Summary of key objective(s)	Usage of SZA	Key results	Potential limitations
				reduced RMSE from 4.6 K (2.0 K) to 3.8 K (1.9 K) for MODIS (SEVIRI).	have minor impacts as SZA-based kernel is symmetric to relative azimuth angles.
Zhao et al. (2019)	Terra-MODIS and MSG-SEVIRI	Normalised the temporal effects of MODIS LST using a random forest regression.	SZA was used to estimate the cumulative incident solar radiation, with the consideration of atmospheric transmittance and path length.	Normalised LST showed reduced bias (RMSE) of 1.66 K (1.23 K) against MSG-SEVIRI LST compared to the original MODIS LST.	The estimation of solar radiation factor may be affected by the simplification of spatial variability of atmospheric transmittance. No ground-based evaluations were performed.
Jiang et al. (2021)	Quasi-simultaneous multi-angle MODIS LST produced by Hu et al. (2016)	Simulated daytime urban thermal radiation directionality (UTRD) using 11 kernel-driven models.	SZA was used to assess the impact of city latitude and to simulate parametric kernels for UTRD.	Dual-kernel models achieved a best performance of RMSE against forward-modelling and satellite data, being 0.49 K and 0.77 K, respectively.	All models used herein were originally developed for vegetated surfaces, without considerations of urban surface types and environmental conditions. No ground-based evaluations were performed.
Wang et al. (2023)	Terra-, Aqua-MODIS and Sentinel-3A	Developed an angular normalisation method for converting global MODIS	SZA was used to estimate sensor-object-solar geometry and kernel functions.	Normalised daytime LST showed bias (RMSE) of 0 K (1.57 K) against *in-situ* LST, and bias (RMSE) of −1.20 K (2.26 K)	This study only focused on the vegetated surfaces. The cross-platform validation (i.e., against

Reference	Satellite platforms	Summary of key objective(s)	Usage of SZA	Key results	Potential limitations
		off-nadir LST to nadir over vegetated surface.		against Sentinel-3A nadir LST, while those of MODIS off-nadir LST being −2.15 K (3.01 K).	Sentinel-3A) was only performed for 4 days in 2020.
Our study	Terra-, Aqua-MODIS, VIIRS and Himawari-AHI	Proposed a calibration approach to reduce the daytime LST discrepancies between polar-orbiting and geostationary platforms.	SZA was used to construct an empirical function representing spatial heterogeneity of surface heating and the magnitude of LST discrepancies from different products.	Calibrated daytime LST showed improved bias (1.52 K, 0.98 K and -0.63 K, respectively) than baseline (5.37 K, 4.85 K and 3.02 K, respectively) against Terra-, Aqua-MODIS and VIIRS LST. It also had the best bias (ubRMSE) of 1.41 K (3.24 K) in evaluations against *in-situ* LST compared to other three Himawari-8 LST products.	The utilised observations of SZA were concentrated between 20 ° and 70 °. The method did not consider elevation and seasonal variations of vegetation.

173

Based on the summary of previous studies presented in Table 1, it is evident that certain limitations exist within the body of research, such as a lack of cross-platform validation, absence of ground-based evaluations, and focus on a limited range of land cover types. These factors collectively suggest that the full potential of SZA has not been explored to maximise the consistency of LST across multiple platforms. Additionally, to enhance the synchronisation of daytime and nighttime observations, it is imperative to gain a comprehensive understanding of the diurnal patterns of LST (Sharifnezhadazizi et al., 2019; Azarderakhsh et al., 2020). While some studies have employed multi-parameter models to simulate the diurnal cycle patterns of LST using sparsely sampled observations from polar-orbiting satellites (Duan et al., 2012; Hu et al., 2020a; Lu and Zhou, 2021), there have been minimal efforts to quantify the diurnal characteristics of error performance of geostationary LST products (Vinnikov et al., 2008; Holmes et al., 2015). Hence, there is a need to address this scientific gap and to investigate the diurnal error dynamics of geostationary LST products, thus further improving accuracy of geostationary LST products.

Accordingly, our objectives were to: (i) calibrate the daytime component of an SW algorithm-retrieved Himawari-8 LST product using an SZA-based calibration approach that incorporates the spatiotemporal characteristics of polar-orbiting MODIS LST; (ii) evaluate the diurnal error characteristics of calibrated LST and collected Himawari-8 LST peer products against *in-situ* LST across different seasons; and (iii) compare the spatial pattern and derive pixelwise metrics of calibrated LST and Himawari-8 LST peer products against VIIRS LST.

2. Data and study area

The remotely sensed data and ground measurements used herein are itemised in Table 2. The Himawari-8 brightness temperature (T_B) was used as input, along with the emissivity, to retrieve LST through an SW algorithm. Two peer Himawari-8 LST products (i.e., (i) Chiba and (ii)

Copernicus) were used for evaluations against *in-situ* LST derived from ground-based longwave radiation and polar-orbiting LST products. The MOD11A1 and MYD11A1 LST products (Collection 6) were employed for pixelwise calibration of SW retrieved Himawari-8 LST and assessment of model performance. The VNP21A1D LST acquired by the VIIRS mission was used for spatiotemporal evaluations of multi-sourced Himawari-8 LST through pixelwise metrics. The longwave radiation obtained from the OzFlux network was used to derive *in-situ* LST for ground-based evaluation. The MOD13A1 enhanced vegetation index (EVI), MCD15A2H leaf area index (LAI) and MCD43A3 albedo products (all Collection 6) were used for evaluations of the spatial patterns of the calibration coefficient of Himawari-8 LST.

Table 2. Summary of data used herein. The spatial resolution of OzFlux measurements is not strictly a point, rather an aggregation of local area fluxes in the vicinity of the flux tower. This means the values of flux towers are representative of a specific region, while the area depends on localised settings in the vicinity of each flux tower station. The contribution from flux tower can range from meters to kilometres and can be considered comparable to remotely sensed data (Chu et al., 2021; Qin et al., 2022). UW denotes University of Wisconsin.

Categories	**Datasets**	**Spatial resolution**	**Temporal frequency**	**Period**	**References**
Input	Himawari-8 T_B	2 km	10-min	01/Jan/2016 – 31/Dec/2020	Bureau of Meteorology (2021)
	UW baseline fit emissivity	5 km	Long-term monthly	01/Jan/2003 – 31/Dec/2016	Seemann et al. (2008)
Himawari-8 LST products	Chiba	2 km	Hourly	01/Jan/2016 – 31/Dec/2020	Yamamoto et al. (2018)
	Copernicus	~ 4.5 km	Hourly	01/Jan/2016 – 31/Dec/2020	Freitas et al. (2013)
Polar-orbiting LST products	MOD11A1 and MYD11A1	1 km	Daily	01/Jan/2016 – 31/Dec/2020	Wan (2014)

Categories	Datasets	Spatial resolution	Temporal frequency	Period	References
	VNP21A1D	1 km	Daily	01/Jan/2016 – 31/Dec/2020	Islam et al. (2016)
Ground measurements	OzFlux Longwave radiation	Point	30-min	01/Jan/2016 – 31/Dec/2020	Beringer et al. (2016)
Surface reflectance products	MOD13A1	500 m	16-day	01/Jan/2016 – 31/Dec/2020	Huete et al. (2002)
	MCD15A2H	500 m	8-day	01/Jan/2016 – 31/Dec/2020	Myneni et al. (2002)
	MCD43A3	500 m	Daily	01/Jan/2016 – 31/Dec/2020	Schaaf et al. (2002)

2.1 UW baseline fit emissivity

The University of Wisconsin (UW) Baseline Fit Emissivity Database is a global database of infrared land surface emissivity derived using an operational MODIS product (MOD11) (Seemann et al., 2008). The database fills in the spectral gaps of MOD11 and provides emissivity at 10 wavelengths, ranging from 3.6 to 14.3 μm, with 0.05 degree spatial resolution (~ 5 km at the equator). We acquired the emissivity at 10.8 and 12.1 μm wavelengths (selected to match the wavelengths used in baseline LST retrieval, see Section 3.1 Baseline algorithm) for each month over 2003-2016 and calculated monthly values by averaging them over the 14-year period.

2.2 Himawari-8 LST

The Himawari-8 geostationary satellite was launched by the Japan Meteorological Agency in October 2014 and has been operational since July 2015 (Bessho et al., 2016). It carries the Advanced Himawari Imager (AHI) with capabilities comparable to the Advanced Baseline Imager (ABI) on board GOES-R (Schmit et al., 2005; Schmit et al., 2008). Himawari-8 is located above the equator at longitude of 140.7 °E and observes east/southeast Asia and Oceania. The AHI has 16 observation bands, including 3 visible bands at wavelengths centred at 0.47, 0.51 and 0.64 μm (B1 – B3), 3 near-infrared (NIR) bands at wavelengths centred at 0.86, 1.61, and 2.25 μm (B4 – B6), and 10 infrared (IR) bands with central wavelengths ranging from 3.9 to 13.3 μm (B7 – B16). The resolution of observation bands ranges from 0.5 to 2 km at the sub-satellite point. The observation cycle occurs every 10 min for the full disk. Himawari-8 data are available through the collection of Australian Bureau of Meteorology Satellite Observations (Bureau of Meteorology, 2021).

2.1.1 Chiba LST

The LST retrieval from Chiba University, Japan, uses a three-band algorithm developed by Yamamoto et al. (2018), herein denoted as the YAM algorithm, which employs several nonlinear terms to improve the LST estimation accuracy over a wide temperature range (Yamamoto et al., 2022). It requires 3 bands of Himawari-8 T_B, 3 bands of LSEs and precipitable water (PW) as inputs. The wavelengths of 3 required TIR bands (T_{B13}, T_{B14} and T_{B15}) are 10.4, 11.2 and 12.4 μm, respectively. LSEs (ε_{B13}, ε_{B14}, and ε_{B15}) are estimated using an NDVI threshold approach developed by Yamamoto and Ishikawa (2018), while PW are total column water vapour values from the European Centre for Medium-Range Weather Forecasts (ECMWF) ReAnalysis version 5 (ERA5; Hersbach et al., 2020). We collected Chiba LST for 01/Jan/2016 – 31/Dec/2020 with a spatial resolution of 2 km and an hourly frequency (i.e., on the hour mark). The Chiba LST data are distributed by the Center for Environmental Remote Sensing (CEReS), Chiba University, Japan, and are freely available at ftp://modis.cr.chiba-u.ac.jp/yyamamoto/AHILST/v0/ (Accessed 05/Oct/2023).

2.1.2 Copernicus LST

The Copernicus LST dataset is a global-coverage LST product using input data from various geostationary satellites, including MSG, GOES and Himawari-8 (Freitas et al., 2013). It employs a generalised SW algorithm to accommodate different characteristics from each geostationary satellite imager, which utilises two adjacent channels within the thermal infrared domain to retrieve LST. We collected Copernicus LST covering 01/Jan/2016 – 31/Dec/2020 with a spatial resolution of ~ 4.5 km at an hourly frequency (i.e., on the hour mark). We acquired the Copernicus LST data from the CGLS project (https://land.copernicus.eu/global/products/lst; accessed 05/Oct/2023).

2.3 MODIS LST

MODIS is aboard the Terra and Aqua satellites launched by the National Aeronautics and Space Administration (NASA) in 1999 and 2002, respectively (Justice et al., 1998). These satellites are in sun-synchronous orbits, where Terra has a nominal descending node at approximately 10:30 local solar time, while Aqua has an ascending node at approximately 13:30 local solar time. The MODIS LST is retrieved through a generalised SW algorithm with a reported accuracy of approximately 2.0 K (Wan, 2014). We collected the MOD11A1 (Terra) and MYD11A1 (Aqua) datasets (both Collection 6) covering 01/Jan/2016 – 31/Dec/2020 with a spatial resolution of 1 km and daily temporal frequency. These data were acquired from the NASA Earthdata Search platform (https://search.earthdata.nasa.gov/search; accessed 05/Oct/2023).

2.4 VIIRS LST

VIIRS is a scanning radiometer on the Suomi National Polar-orbiting Partnership (Suomi-NPP) satellite launched by NASA in October 2011 (Islam et al., 2016). It operates in a sun-synchronous orbit, with an equatorial crossing time at the ascending node of approximately 13:30 local solar time. The VIIRS LST & Emissivity (LST&E) product (VNP21) is retrieved using a physics-based Temperature and Emissivity Separation (TES) algorithm, providing the simultaneous retrieval of LST and emissivity from the thermal infrared bands. We obtained the VNP21A1D dataset (Collection 1) for 01/Jan/2016 to 31/Dec/2020 with a spatial resolution of 1 km and daily temporal frequency. The data were acquired from the NASA Earthdata Search platform (https://search.earthdata.nasa.gov/search; accessed 05/Oct/2023).

2.5 Study area and *in-situ* measurements

The observation area of Himawari-8 covers the longitude of 85 °E – 155 °W and latitude of 60 °S – 60 °N (Fig. 1a). We chose a subset (112 °E – 154 °E and 45 °S – 10 °S) covering the Australian continent as the study area. Fig. 1 (b) shows the land cover of Australia (Lymburner et al., 2015) and locations of 20 flux tower sites from the OzFlux network (Beringer et al., 2016). Table 3 provides the details of the 20 flux tower sites.

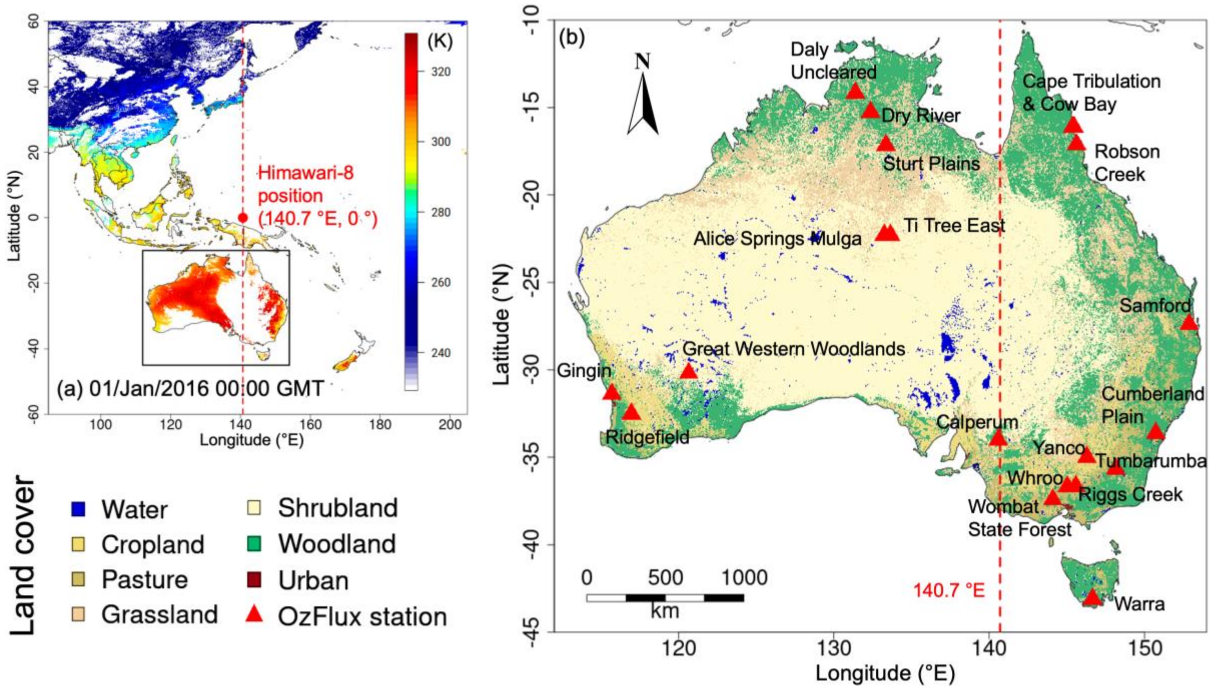

Fig. 1. (a) LST of the full-disk Himawari-8 observation area on 01/Jan/2016 00:00 GMT with clouds and oceans masked out; and (b) the land cover map of Australia (Lymburner et al., 2015) and the distribution of 20 OzFlux sites. The study site is provided by the black rectangle bounding Australia in (a).

Table 3. Summary of 20 sites from the OzFlux network. The land cover and annual rainfall information are from https://ozflux.org.au/ (Accessed 05/Oct/2023). The following abbreviations are used in the 'standard

time zone' column: ACST (Australian Central Standard Time; GMT+9.5); AEST (Australian Eastern Standard Time; GMT+10); AWST (Australian Western Standard Time; GMT+8).

Site name	Latitude (°N)	Longitude (°E)	Land cover	Annual rainfall (mm/year)	Standard time zone
Alice Springs Mulga	-22.283	133.249	Semi-arid mulga	306	ACST
Calperum	-34.003	140.588	Recovering woodland	240	ACST
Cape Tribulation	-16.106	145.378	Tropical rainforest	5,700	AEST
Cow Bay	-16.103	145.447	Complex mesophyll vine forest	4,000	AEST
Cumberland Plain	-33.615	150.724	Dry sclerophyll	800	AEST
Daly Uncleared	-14.159	131.388	Woodland savanna	1,170	ACST
Dry River	-15.258	132.370	Open forest savanna	895	ACST
Gingin	-31.376	115.714	Coastal health woodland	641	AWST
Great Western Woodlands	-30.191	120.654	Temperate woodland, shrubland and mallee	240	AWST
Ridgefield	-32.506	116.966	Dryland agriculture	446	AWST
Riggs Creek	-36.650	145.576	Dryland agriculture	650	AEST
Robson Creek	-17.118	145.630	Complex mesophyll vine forest	2,236	AEST
Samford	-27.388	152.877	Improved pasture	1,102	AEST
Sturt Plains	-17.150	133.350	Low lying plain dominated by grass	640	ACST
Ti Tree East	-22.287	133.640	Grassy mulga woodland and savanna	305	ACST
Tumbarumba	-35.656	148.151	Wet temperate sclerophyll eucalypt	1,000	AEST
Warra	-43.095	146.654	Eucalyptus obliqua forest	1,700	AEST
Whroo	-36.673	145.029	Box woodland	558	AEST
Wombat State Forest	-37.422	144.094	Dry sclerophyll eucalypt forest	650	AEST
Yanco	-34.989	146.291	Various soils and cropland	465	AEST

We estimated the *in-situ* LST using the ground-level upwelling and downwelling longwave radiation (Level 3) data observed at the OzFlux stations. By manipulating the traditional equation governing longwave radiation balance (Allen et al., 1998; Trebs et al., 2021) an approximation of the *in-situ* LST was derived as:

$$LST_{in-situ} = \left(\frac{F^{\uparrow} - (1 - \varepsilon_b)F^{\downarrow}}{\sigma\varepsilon_b}\right)^{1/4} \quad (1)$$

where $LST_{in-situ}$ is *in-situ* LST (K), $F^{\uparrow}$ is the upwelling longwave radiation (W/m^2), $F^{\downarrow}$ is the downwelling longwave radiation (W/m^2), ε_b is the surface broadband emissivity (unitless), and σ is the Boltzmann constant (5.67 × 10^{-8} W m^{-2} K^{-4}).

2.6 MODIS surface reflectance-derived indices

We collected three MODIS surface reflectance-derived products, including the 500 m resolution 16-day MOD13A1 EVI (Huete et al., 2002), the 500 m resolution 8-day MCD15A2H LAI (Myneni et al., 2002) and the 500 m resolution daily MCD43A3 albedo (Schaaf et al., 2002) products (all Collection 6), covering 01/Jan/2016 – 31/Dec/2020. We calculated the pixelwise median values of each product for the Australian continent throughout the 5-year period. These data were acquired from the NASA Earthdata Search platform (https://search.earthdata.nasa.gov/search; accessed 05/Oct/2023).

3. Methodology

Fig. 2 presents the experimental design employed herein, comprising three key steps. Firstly, we retrieved the baseline LST through an SW algorithm (Yu et al., 2012) using Himawari-8 T_B and emissivity from the UW Baseline Fit Emissivity Database (Section 3.1 Baseline algorithm). Secondly, we conducted the Solar Zenith Angle-based Calibration (SZAC) using all available scenes of Terra- and Aqua-MODIS daytime LST for the Australian continent between 01/Jan/2016 and 31/Dec/2020. To ensure the highest data quality, we applied quality assurance (QA) flags to select MODIS LST pixels with an expected retrieval error of less than 1.0 K (Wan, 2013). We selected MODIS QA flags with numeric values of 0, 5, 17 and 21. By using the time series of both

MODIS best-quality LST and baseline LST, we derived a spatial distribution of optimised coefficient of SZAC for Australia, which allowed us to calibrate the daytime component of baseline LST. This step is denoted as Section 3.2 Solar Zenith Angle-based Calibration (SZAC). Thirdly and finally, we evaluated the performance of calibrated LST, referred to as the Australian National University LST with SZAC (ANU_{SZAC} LST), against *in-situ* LST and all available pixels from MODIS and VIIRS LST data between 01/Jan/2016 and 31/Dec/2020, while utilising the performances of three Himawari-8 LST datasets (baseline, Chiba, and Copernicus) as comparisons (Section 3.3 Multi-platform evaluation).

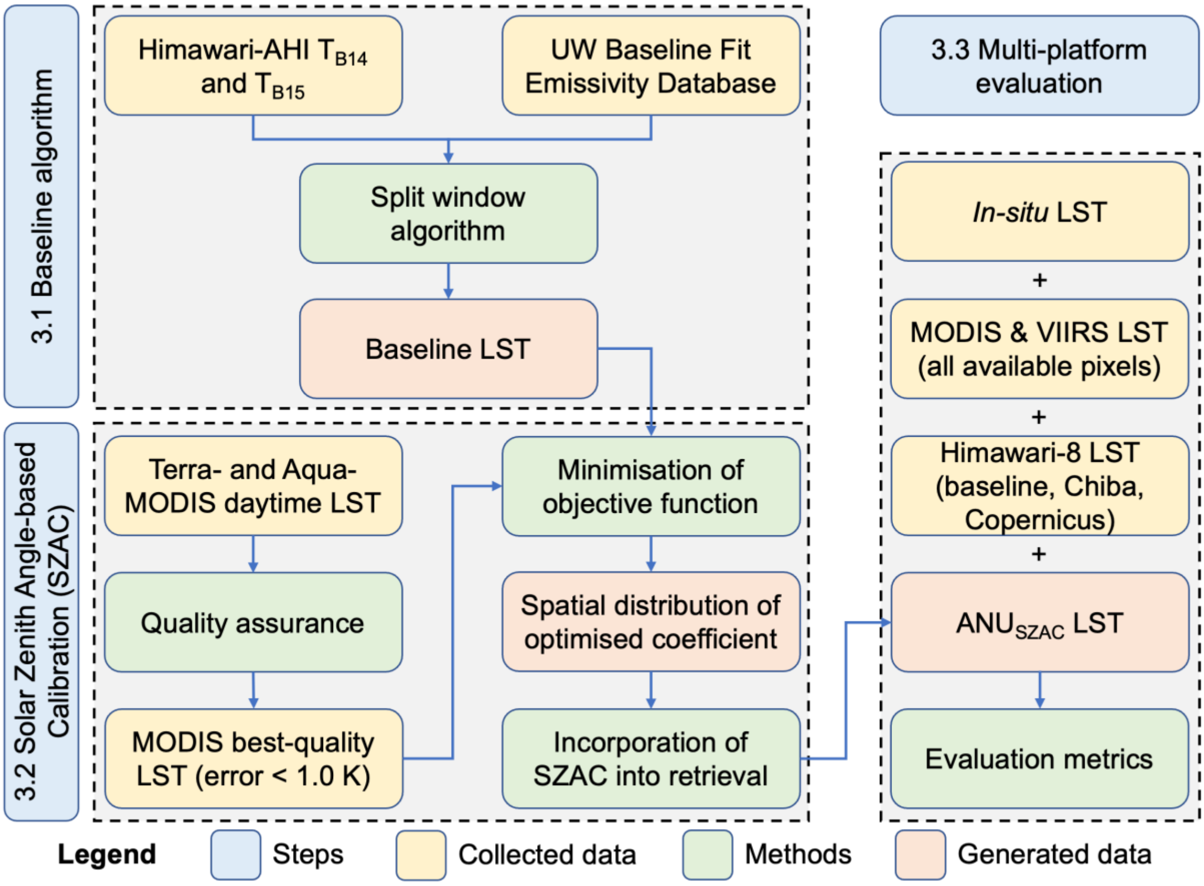

Fig. 2. Experimental design for this research. The SZAC process was conducted using the time series of every 2 × 2 km pixel throughout the Australian continent.

3.1 Baseline algorithm

We employed an SW algorithm (Yu et al., 2009) with coefficients from Yu et al. (2012) to retrieve LST, referred to as the baseline Himawari-8 LST retrieval herein, taking the following forms:

$$LST_{day} = 30.022546 + 1.018212T_{11} + 1.263787(T_{11} - T_{12}) - 39.387858\varepsilon + 0.609744(T_{11} - T_{12})(sec\theta_{view} - 1) \quad (2)$$

$$LST_{night} = 36.160667 + 1.012895T_{11} + 1.022203(T_{11} - T_{12}) - 38.909505\varepsilon + 0.669541(T_{11} - T_{12})(sec\theta_{view} - 1) \quad (3)$$

where LST_{day} and LST_{night} represent LST (K) during daytime and nighttime, respectively, which are defined as when SZA (°) is lower/higher than 85 °; T_{11} and T_{12} are T_B (K) at ~ 11 and ~ 12 μm wavelength (i.e., Himawari-8 bands 14 and 15, respectively); ε is broadband emissivity (unitless); θ_{view} is the viewing zenith angle (VZA; °) of Himawari-8. The Yu et al. (2012) LST coefficients were originally developed for GOES-ABI and with Himawari-AHI having essentially identical spectral and radiometric characteristics at bands 14 and 15 (Schmit et al., 2008; Bessho et al., 2016) they were applied to Himawari-8 data.

3.2 Solar Zenith Angle-based Calibration (SZAC)

SZA has underscored its effectiveness in rectifying LST discrepancies arising from multiple observational platforms (see Table 1). SZA can serve as a proxy for the amount of solar energy that reaches the ground surface, and its consequent impact on LST can be analysed through statistical approaches (Cresswell et al., 1999). Theoretically, SZA should remain consistent across all platforms, serving as an ideal bridging parameter to quantify systematic differences between them. This is preferable to VZA, as the scanning strategies of polar-orbiting and geostationary platforms are fundamentally distinct. This facilitates a spatially coherent approach for achieving the necessary spatiotemporal calibration.

Here we introduce the concept of SZAC to calibrate the daytime component of Himawari-8 baseline LST using an empirical function of SZA on a pixelwise basis. In SZAC, a fundamental assumption is that the diurnal variations of clear-sky LST are continuous and can be simulated using discrete observations (Duan et al., 2012; Lu and Zhou, 2021). SZAC is a calibration factor (K) to be subtracted from daytime baseline LST, which involves the application of a logarithm on the cosine of SZA and is given as:

$$SZAC(x_i, y_i, t) = Coeff(x_i, y_i) \times log(cos\theta_{solar}(x_i, y_i, t) + 1) \quad (4)$$

$$cos\,\theta_{solar}(x_i, y_i, t) = sin\,\Phi(x_i, y_i)\,sin\,\delta(x_i, y_i, t) + cos\,\Phi(x_i, y_i)\,cos\,\delta(x_i, y_i, t)\,cos\,h(x_i, y_i, t) \quad (5)$$

where (x_i, y_i) is the geolocation of a given pixel i; t is the given time; $SZAC$ is the calibration factor (K); $Coeff$ is an empirical coefficient (K) to be optimised; θ_{solar} is SZA (°); Φ is the latitude; δ is the current declination of Sun; and h is the hour angle in local solar time.

SZAC can be conceptualised as the magnitude of LST disparities between different platforms during the heating period of surface. The cosine of SZA represents the diurnal variations of shadowed area in relation to the total surface area, serving as an effective measure of the solar radiance (not considering topographic adjustment) reaching the Earth's surface (Yeom et al., 2012), with the application of a logarithmic filter to attenuate potential overfitting of regression. Additionally, this filtering ensures the curve approaches near-zero values during the day-night transition and not adversely affect nighttime LST retrievals. We employed LST from both Terra- and Aqua-MODIS as reference for optimising the coefficient of SZAC. Fig. 3 (a) provides a scatterplot example illustrating the baseline-MODIS difference plotted against SZA at the Wombat State Forest site during 1/Jan/2016-31/Dec/2020. The majority of samples cluster within the range of 20 - 70 ° SZA, which corresponds to the MODIS overpass times of approximately 10:30 am and 1:30 pm local solar time for Terra and Aqua, respectively. Fig. 3 (b) shows the temporal variation of

SZAC throughout a day. SZAC attains its maximum value when SZA is lowest (i.e., around midday) and reaches its minimum value when SZA is approximately 85 ° (i.e., sunrise or sunset). This ensures that SZAC has minimal impact on the day-night transition and does not affect the nighttime LST retrievals.

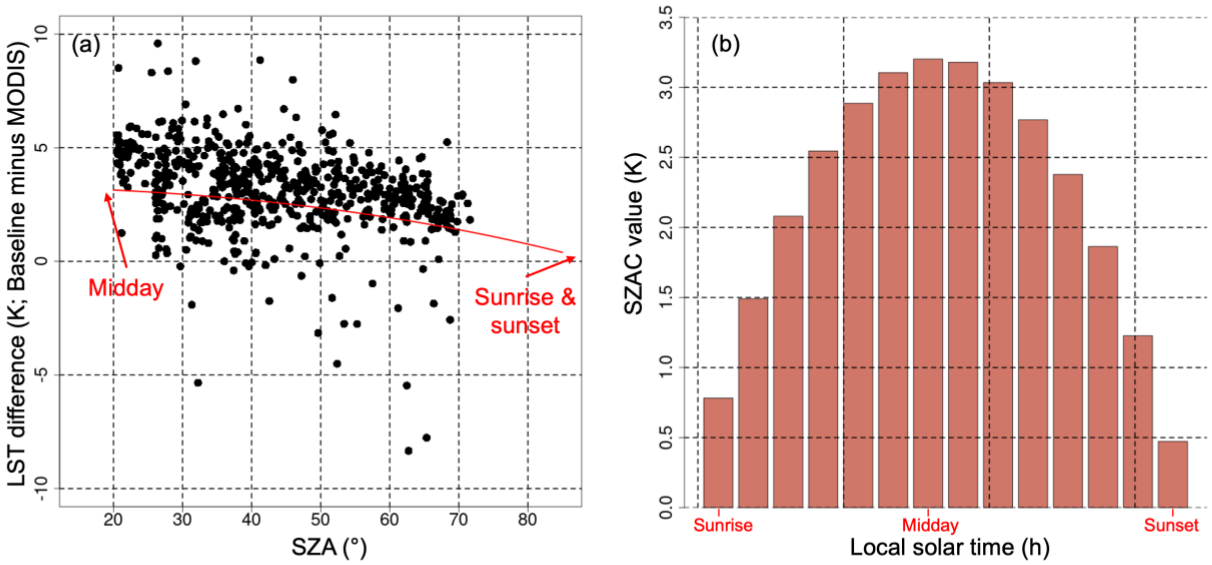

Fig. 3. (a) Schematic of SZAC at the Wombat State Forest site and; (b) an example to show the temporal variation (using a bin size of 60 minutes) of SZAC during daytime on 02/Jan/2016. The location of Wombat State Forest is shown on Fig. 1. (b) with additional details provided in Table 3.

We employed the Brent (2013) local optimisation approach to determine the coefficient of SZAC for each matched cloud-free baseline-MODIS LST time series during 1/Jan/2016-31/Dec/2020 on a pixelwise basis. This minimised the difference between all coincident baseline Himawari LST and MODIS LST observations over the full 5-year period on a pixelwise basis. The objective function was the root mean square error (RMSE) between the baseline LST and MODIS LST. Then the daytime baseline LST for each pixel was calibrated using the single coefficient along with the temporal variations of SZA, which was denoted as the calibrated LST (i.e., ANU_{SZAC}):

$$LST_{day,ZAC}(x_i, y_i, t) = LST_{day}(x_i, y_i, t) - SZAC(x_i, y_i, t) \tag{6}$$

where $LST_{day,ZAC}$ is the calibrated daytime LST and LST_{day} is the baseline daytime LST.

3.3 Multi-platform evaluation

3.3.1 Cross-satellite matching strategy

Geostationary and polar-orbiting satellites have different surface scanning strategies. The Terra, Aqua and Suomi-NPP satellites do not have a constant overpass time, e.g., the data acquisition time of Terra ranges from 10:00 to 12:10 local solar time (Hu et al., 2014). To standardise the acquisition times of MODIS and VIIRS LST records and make them comparable with those of Himawari-8 LST, we converted the MODIS and VIIRS 'view time' layer, which is expressed in local solar time, to the GMT format, which is given as:

$$T_{polar,GMT}(x_i, y_i, t) = T_{polar,solar}(x_i, y_i, t) - Lon/15 \tag{7}$$

where $T_{polar,GMT}$ is the MODIS or VIIRS view time in GMT format, $T_{polar,solar}$ is the MODIS or VIIRS view time in local solar time, and Lon is the longitude in decimal of a given pixel. Then we utilised a one-hour temporal window (i.e., ± 30 minutes) to match Himawari-8 time (GMT) and MODIS time (GMT) on a pixelwise basis:

$$T_{H8,GMT}(x_i, y_i, t) - 30\ min \leq T_{polar,GMT}(x_i, y_i, t) \leq T_{H8,GMT}(x_i, y_i, t) + 30\ min \tag{8}$$

where $T_{H8,GMT}$ is the time stamp of Himawari-8 in GMT format. This matching strategy allowed us to derive comparable LST records from Himawari-8 and polar orbiting satellites (MODIS or VIIRS).

3.3.2 *In-situ* matching strategy

We employed the *in-situ* LST derived from OzFlux longwave radiation to evaluate Himawari-8 LST. Flux towers from the OzFlux network (see Fig. 1 (b) for locations and Table 3 for additional information) measure longwave radiation at half-hour intervals. We also implemented a one-hour temporal window (i.e., ± 30 minutes) strategy, similar to Eq. 8, to match Himawari-8 time (GMT) and *in-situ* time (converted to GMT). We calculated the mean in cases where two *in-situ* records are present within the hour. By adopting this approach, direct comparisons between Himawari-8 LST observations and corresponding ground-level measurements were made, disregarding individual time zones of flux towers.

3.3.3 Evaluation metrics

We utilised bias and unbiased root mean square error (ubRMSE) to evaluate the performance of Himawari-8 LST data against the corresponding reference LST:

$$Bias = \frac{\sum\left(LST_{H8} - LST_{ref}\right)}{N} \quad (9)$$

$$ubRMSE = \sqrt{\frac{\sum\left(\left(LST_{H8} - \mu(LST_{H8})\right) - \left(LST_{ref} - \mu\left(LST_{ref}\right)\right)\right)^2}{N}} \quad (10)$$

where LST_{H8} is the time series of Himawari-8 (i.e., baseline, Chiba, Copernicus or ANU_{SZAC}) LST; LST_{ref} is the time series of reference (i.e., *in-situ*, MODIS or VIIRS) LST; N is the number of individual observations in each reference time series.

4. Results

4.1 Assessment of MODIS-based SZAC's performance

Fig. 4 (a) shows the spatial distribution of SZAC coefficient for the Australian continent. Lower values of the coefficient (less than 4 K) were observed over the eastern edge, whereas higher values (exceeding 8 K) were concentrated in central and northern Australia. This means that the Himawari-8 baseline LST was more consistent with MODIS LST in Australia's eastern coastal regions, yet tended to overestimate LST in central and northern Australia when compared to MODIS LST. Notably, the area of Lake Eyre, the largest salt-lake in inland Australia, exhibited the lowest coefficient value (~2 K), which could be attributed to the absence of canopies within these highly reflective salt-lake regions. A more detailed analysis of the spatial pattern of SZAC coefficient is elucidated in Fig. 15. The distribution of the SZAC coefficient was also influenced by the scanning strategy employed by the MODIS instrument during its orbit which resulted in MODIS-induced strips in the SZAC coefficient. Nevertheless, as SZAC functions as a calibration factor to be subtracted from the Himawari-8 baseline LST, it introduces certain offsets associated with the emissivity artifacts within the baseline LST. This phenomenon is further elucidated in Fig. 5.

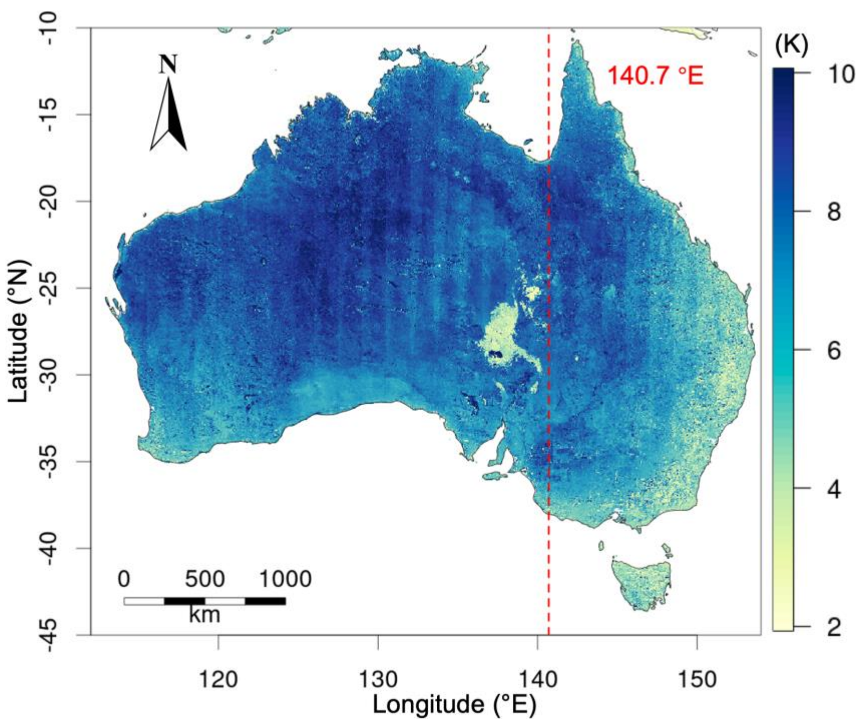

Fig. 4. (a) Spatial distribution of the SZAC coefficient for the Australian continent during 01/Jan/2016 – 31/Dec/2020. The 'light-green / yellow' region just west of Himawari's longitude (140.7 °E represented by the red dashed line) exhibiting the lowest coefficient values of ~ 2 K, is associated with Lake Eyre and other salt lakes within inland Australia.

Fig. 5 presents the spatial distribution of input emissivity, SZAC values, baseline and ANU_{SZAC} LST at 02:00 GMT (i.e., 12:00 AEST) on (a-d) 20/Mar/2016 (austral autumn equinox); (e-h) 21/Jun/2016 (austral winter solstice); (i-l) 23/Sep/2016 (austral spring equinox); and (m-p) 21/Dec/2016 (austral summer solstice). The SZAC values showed seasonal variations, being highest at the summer solstice (Fig. 5 n), moderate and comparable at the spring and autumn equinoxes (Fig. 5 b and j), and lowest at the winter solstice (Fig. 5 f). This variation signifies that the disparities between the baseline LST and MODIS LST were most pronounced in the summer, a period when incoming radiation peaks and necessitate a stronger correction. The systematic differences between the Himawari-8 baseline and MODIS LST in inland and northern Australia were always higher than other regions. Furthermore, both input emissivity (Fig. 5; first column) and SZAC values (Fig. 5; second column) exhibited artefacts associated with MODIS scanning effects. However, these artefacts were effectively removed by the calibration process as seen in both baseline (Fig. 5; third column) and ANU_{SZAC} LST (Fig. 5; fourth column).

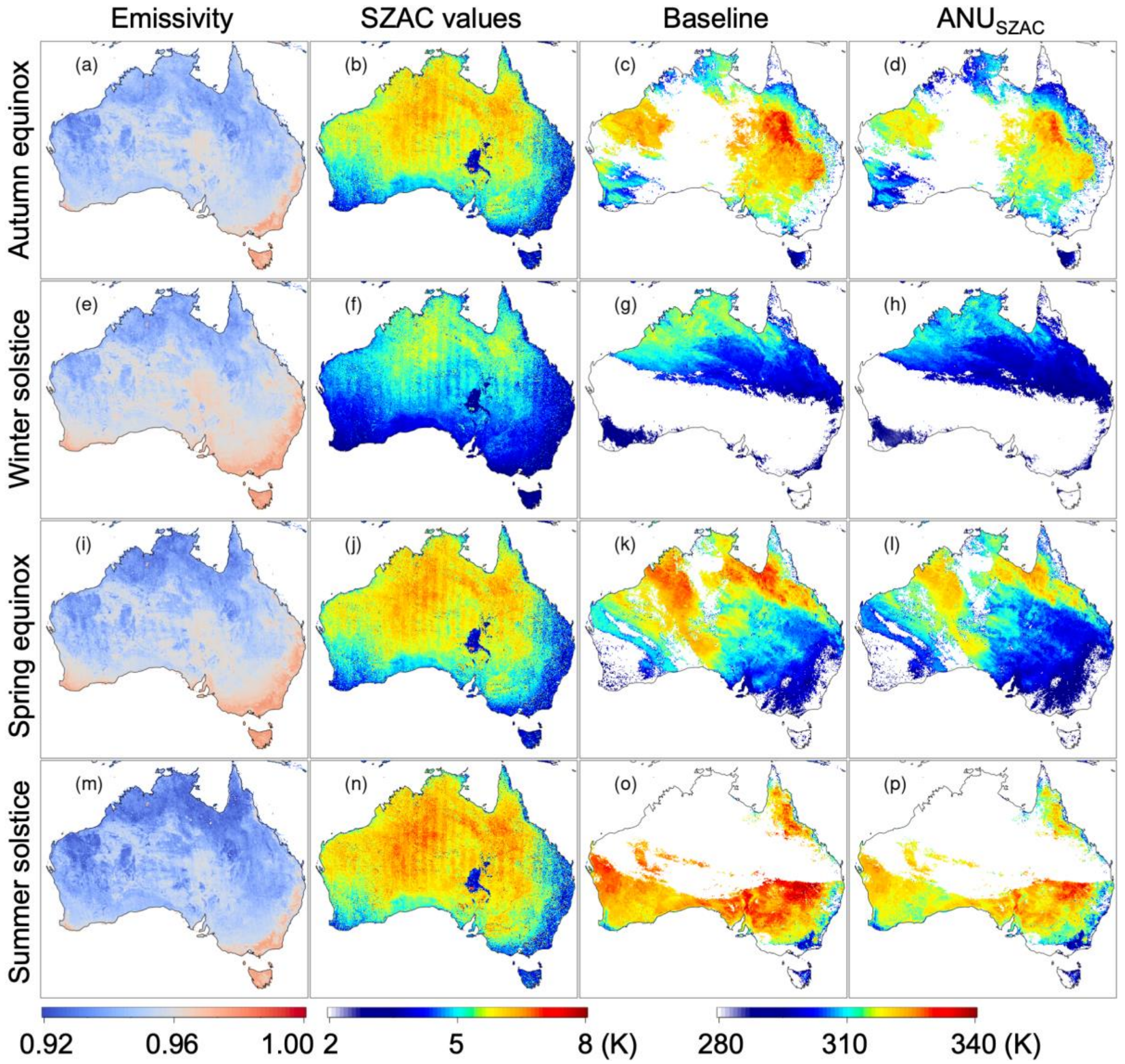

Fig. 5. Respective spatial distribution of emissivity, SZAC values, baseline and ANU$_{SZAC}$ LST at 02:00 GMT on (a-d) 20/Mar/2016 (austral autumn equinox); (e-h) 21/Jun/2016 (austral winter solstice); (i-l) 23/Sep/2016 (austral spring equinox); and (m-p) 21/Dec/2016 (austral summer solstice). The oceans and seas surrounding Australia are white in all parts, with Himawari cloud contaminated pixels being white over land in the two columns on the right.

Fig. 6 presents the spatial distribution of bias (a-b) and ubRMSE (c-d) of baseline and ANU$_{SZAC}$ LST against best-quality MODIS LST for the Australian continent between 01/Jan/2016 and 31/Dec/2020. This evaluation assesses the fitting performance of ANU$_{SZAC}$ LST by comparing to the training set. The median bias of baseline LST against $MODIS_{best}$ LST for the Australian continent is 5.09 K while the median bias of ANU_{SZAC} LST was reduced to 1.07 K. Both baseline and ANU_{SZAC} LST demonstrated comparable levels of ubRMSE performance, being 2.50 K and 2.53 K, respectively. In general, both LST products exhibited the lowest ubRMSE values (ranging from 1 to 2 K) for much of inland Australia. However, over coastal regions, the ubRMSE increased to 2 to 3 K for both products (Fig. 6 b and e). The evaluation based on the training set demonstrated that SZAC could reduce the bias performance while maintaining a similar ubRMSE level.

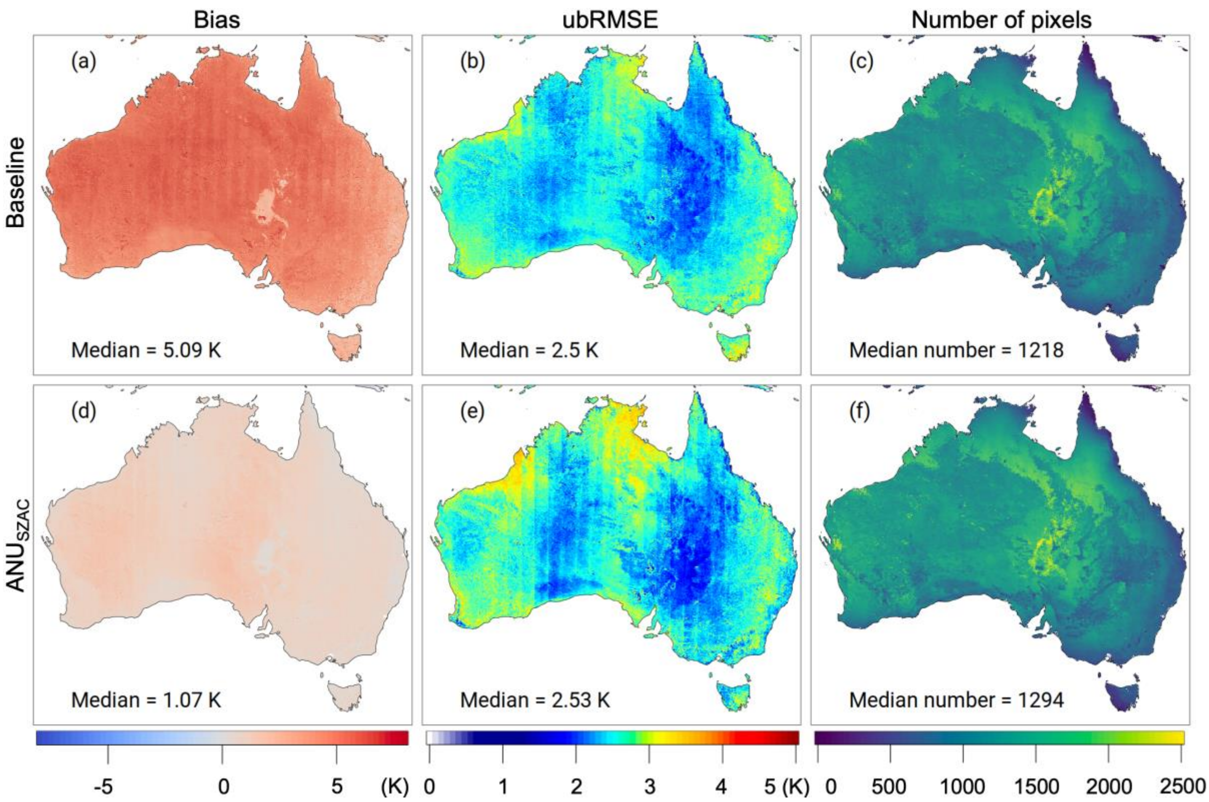

Fig. 6. Spatial distribution of bias and ubRMSE of baseline and ANU_{SZAC} LST against best-quality (i.e., expected error < 1 K) MODIS (both MOD11A1 and MYD11A1) LST for the Australian continent between 01/Jan/2016 and 31/Dec/2020. The oceans and seas surrounding Australia are white in all parts.

Fig. 7 presents the spatial distribution of bias (a-d) and ubRMSE (e-h) of baseline, Chiba, Copernicus and ANU_{SZAC} LST against all available LST pixels from Terra-MODIS (i.e., MOD11A1) for the Australian continent at ~ 10:30 local solar time between 01/Jan/2016 and 31/Dec/2020. The median bias of baseline, Chiba, Copernicus LST against Terra-MODIS LST for the Australian continent was 5.37, 3.71, 3.25 K, respectively, while the median bias of ANU_{SZAC} LST was only 1.52 K, less than half of the second-best other result (i.e., Copernicus LST). This indicates that ANU_{SZAC} LST outperformed the other LST products in terms of bias, demonstrating an improved agreement against the ~ 10:30 local solar time Terra-MODIS LST. The median ubRMSE of baseline, Chiba, Copernicus LST was 2.47, 2.56 and 2.55 K, respectively, while the ubRMSE of ANU_{SZAC} LST was 2.75 K and showed more spatial variability.

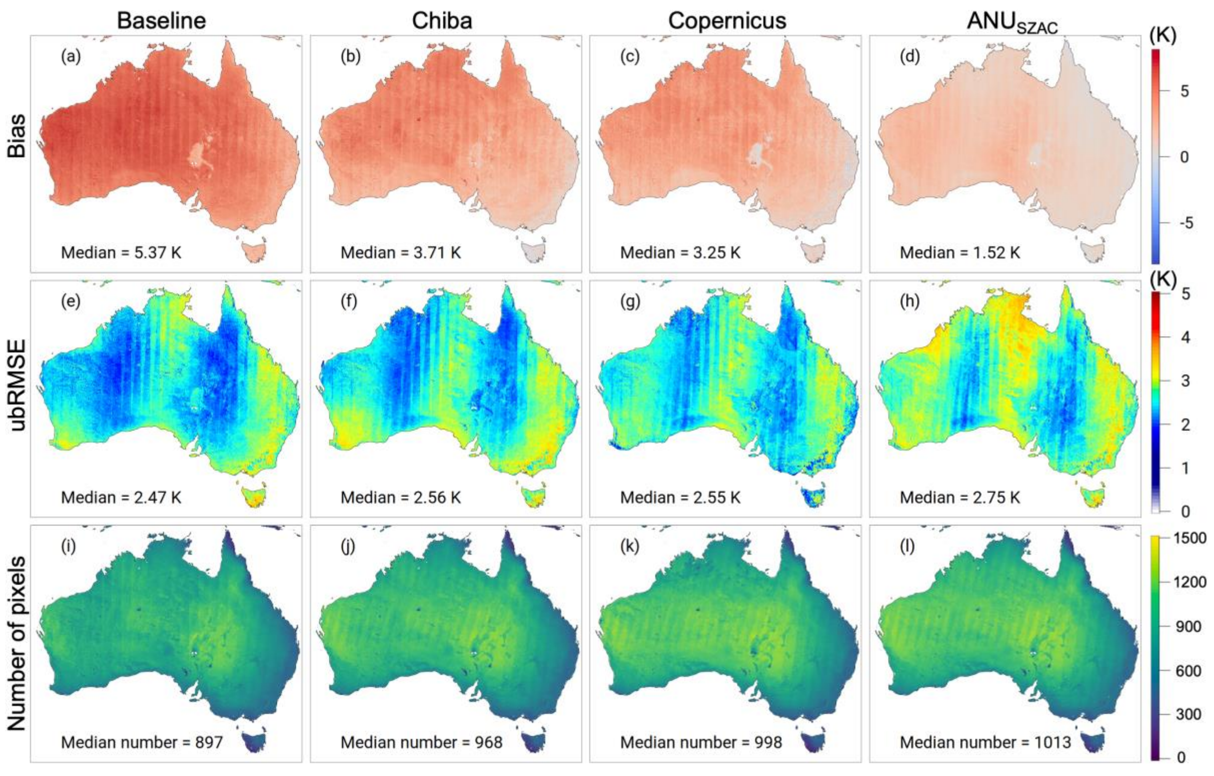

Fig. 7. Spatial distribution of bias and ubRMSE of baseline, Chiba, Copernicus and ANU_{SZAC} LST against all available LST pixels from Terra-MODIS (i.e., MOD11A1) for the Australian continent at ~ 10:30 local solar time between 01/Jan/2016 and 31/Dec/2020. The oceans and seas surrounding Australia are white in all parts.

Fig. 8 presents the spatial distribution of bias (a-d) and ubRMSE (e-h) of baseline, Chiba, Copernicus and ANU_{SZAC} LST against all available LST pixels from Aqua-MODIS (i.e., MYD11A1) for the Australian continent at ~ 13:30 local solar time between 01/Jan/2016 and 31/Dec/2020. The median bias of baseline, Chiba, Copernicus LST against Aqua-MODIS LST for Australian was 4.85, 2.90 and 2.28 K, respectively. In contrast, ANU_{SZAC} LST exhibited a reduced median bias of 0.98 K, which was less than half of the second-best other result (i.e., Copernicus LST). This indicated that all Himawari-8 LST products showed better agreement in the afternoon (~ 13:30 local solar time) than the morning (~ 10:30 local solar time), while ANU_{SZAC} LST had a superior bias performance compared to the three other LST products in both the morning and afternoon. The median ubRMSE of baseline, Chiba, Copernicus and ANU_{SZAC} LST was 2.42, 2.37, 2.48 and 2.44 K, respectively. Both baseline and ANU_{SZAC} LST displayed relatively lower ubRMSE values (~ 2 K) for inland regions with relatively higher values (~ 3 K) in the north. The differences in the direction of strips seen in Fig. 8 compared to Fig. 7 are attributed to the differences of orbits of Terra (descending at ~ 10:30 local solar time) and Aqua (ascending at ~ 13:30 local solar time) satellites.

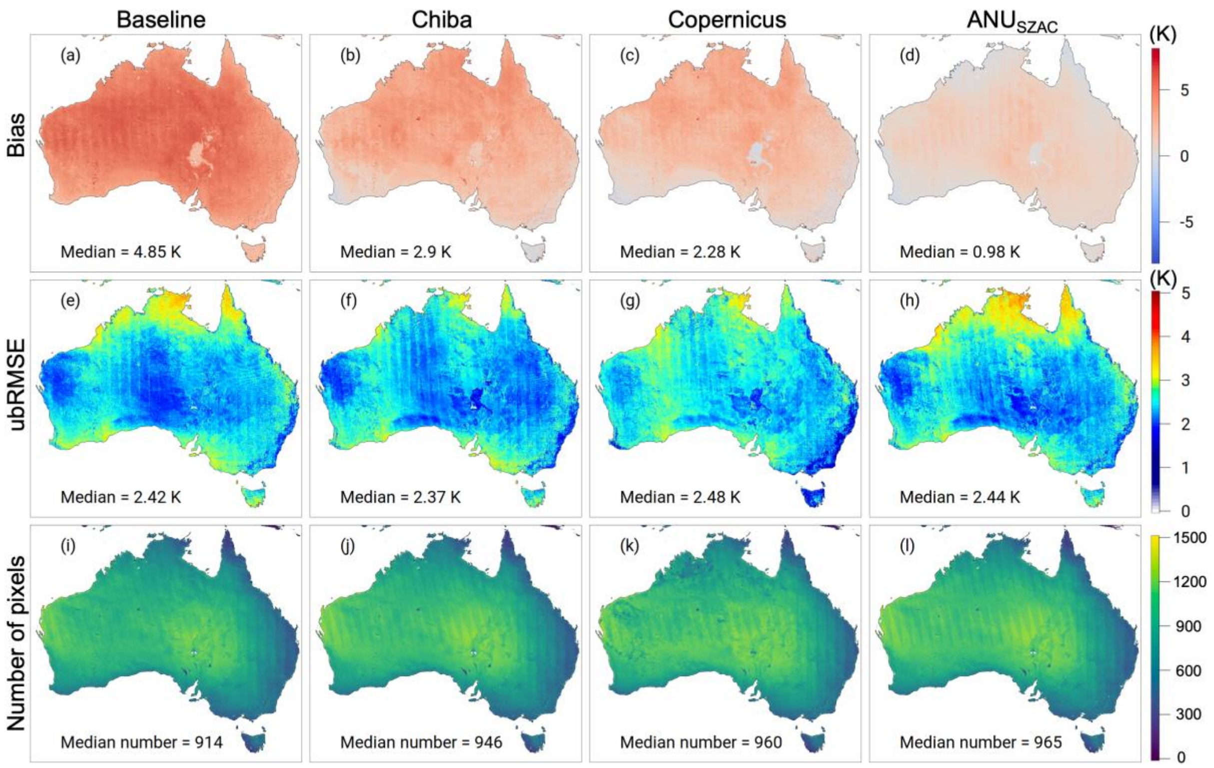

Fig. 8. Spatial distribution of bias and ubRMSE of baseline, Chiba, Copernicus and ANU_{SZAC} LST against all available LST pixels from Aqua-MODIS (i.e., MYD11A1) for Australia at ~ 13:30 local solar time between 01/Jan/2016 and 31/Dec/2020. The oceans and seas surrounding Australia are white in all parts.

4.2 Evaluation against *in-situ* LST during 2016-2020

Fig. 9 presents the annual and seasonal boxplots of bias of baseline, Chiba, Copernicus and ANU_{SZAC} LST against the *in-situ* LST derived at the 20 OzFlux sites (see Fig. 1 (b) for their locations) at different times (i.e., all day, daytime and nighttime) between 01/Jan/2016 and 31/Dec/2020. Regarding the all-day metrics (Fig. 9 a), the overall mean values of bias of baseline, Chiba, Copernicus and ANU_{SZAC} LST were 1.87 K, -0.29 K, -0.57 K and 0.60 K, respectively. For the daytime evaluation (Fig. 9 b), the overall mean values of bias of baseline, Chiba, Copernicus and ANU_{SZAC} LST were 4.23 K, 2.16 K, 1.73 K and 1.41 K, respectively. ANU_{SZAC} LST exhibited better performance than baseline LST and outperformed Chiba and Copernicus in almost all seasons during daytime; while ANU_{SZAC} LST was comparable with Copernicus LST in winter. For the nighttime evaluation (i.e., Fig. 9 c), the overall mean values of bias of baseline, Chiba, Copernicus and ANU_{SZAC} LST against *in-situ* LST were 0.06 K, -2.29 K, -2.45 K and -0.06 K, respectively. As no SZAC was applied at the night, the baseline and ANU_{SZAC} LST exhibit identical performance during nighttime. Both baseline and ANU_{SZAC} LST consistently outperformed Chiba and Copernicus LST in all seasons during nighttime evaluations. It is notable that the superior all-day bias metrics of Chiba and Copernicus LST were due to the daytime and nighttime bias metrics essentially cancelling each other out. For detailed metrics of the individual 20 OzFlux sites, see Table S1 in the Supplementary material.

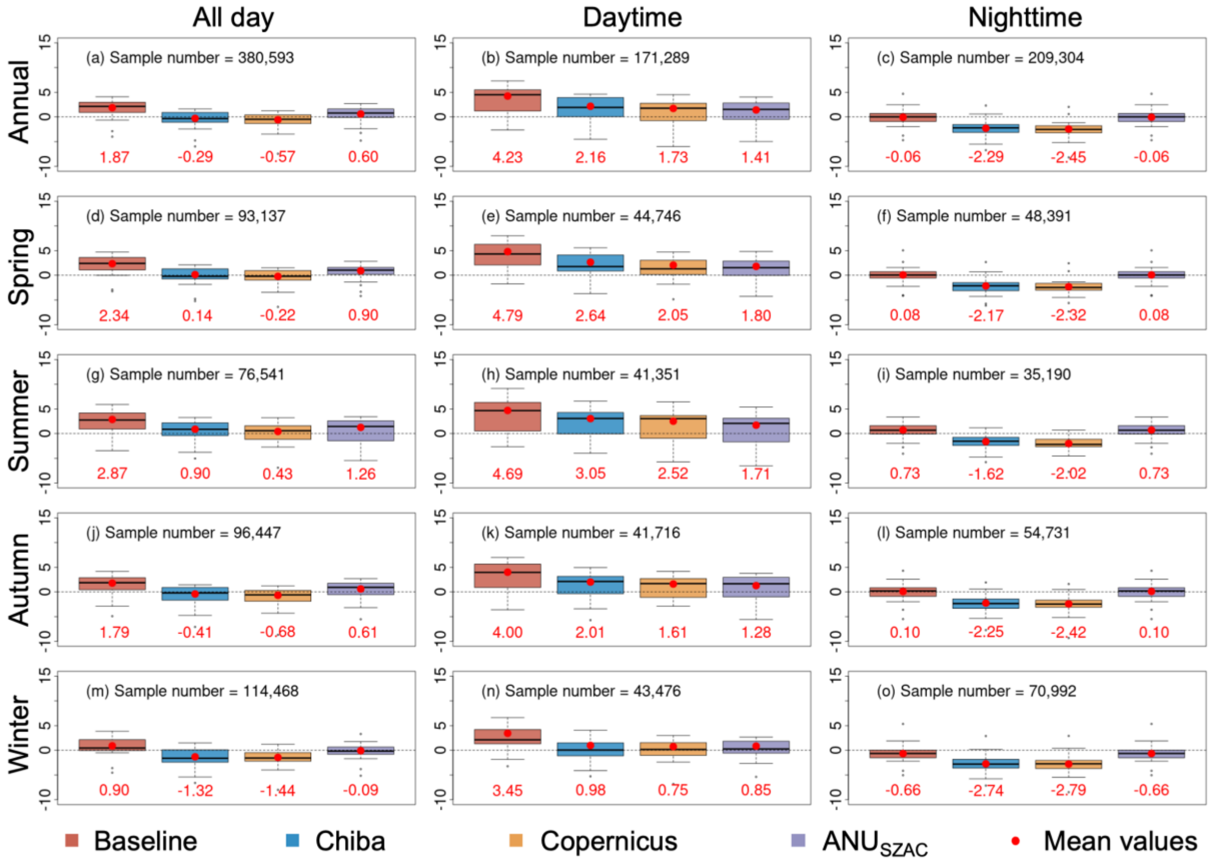

Fig. 9. Annual and seasonal boxplots of bias of baseline, Chiba, Copernicus and ANU_{SZAC} LST against in-situ LST at different times (i.e., all day, daytime and nighttime) between 01/Jan/2016 and 31/Dec/2020. For the southern hemisphere spring is from September to November, summer from December to February, autumn from March to May, and winter from June to August. The dark horizontal line within the boxplots represents the median value; the upper and lower lines defining the coloured rectangle are the interquartile range (i.e., the 75% and 25% values) respectively; the upper and lower whiskers extend from the box represent the maximum and minimum values excluding any outliers. The red numbers at the bottom of each plot are the overall mean values of bias. The unit of bias is K.

Fig. 10 presents the annual and seasonal boxplots of ubRMSE of baseline, Chiba, Copernicus and ANU_{SZAC} LST against *in-situ* LST at different times (i.e., all day, daytime and nighttime) between 01/Jan/2016 and 31/Dec/2020 for the 20 OzFlux sites. Regarding the all-day metrics (Fig. 10 a), the overall mean values of ubRMSE of baseline, Chiba, Copernicus and ANU_{SZAC} LST were 3.98

K, 3.89 K, 3.69 K and 3.24 K, respectively. ANU_{SZAC} LST displayed a narrowed spread of ubRMSE in all seasons, which indicated that ANU_{SZAC} LST had the best overall agreement with *in-situ* LST. For the daytime evaluation (Fig. 10 b), the overall mean values of ubRMSE of baseline, Chiba, Copernicus and ANU_{SZAC} LST were 3.74 K, 3.62 K, 3.31 K and 3.24 K, respectively. ANU_{SZAC} LST demonstrated narrowed spread than baseline throughout all seasons. For the nighttime evaluation (Fig. 10 c), the overall mean values of ubRMSE of baseline, Chiba, Copernicus and ANU_{SZAC} LST against *in-situ* LST were 2.77 K, 2.57 K, 2.54 K and 2.77 K, respectively. The nighttime measurements of all four LST products were generally comparable across all seasons, with Copernicus LST showing a slightly greater uncertainty in the spread of ubRMSE. For detailed metrics of the individual 20 OzFlux sites, see Table S2 in the Supplementary material.

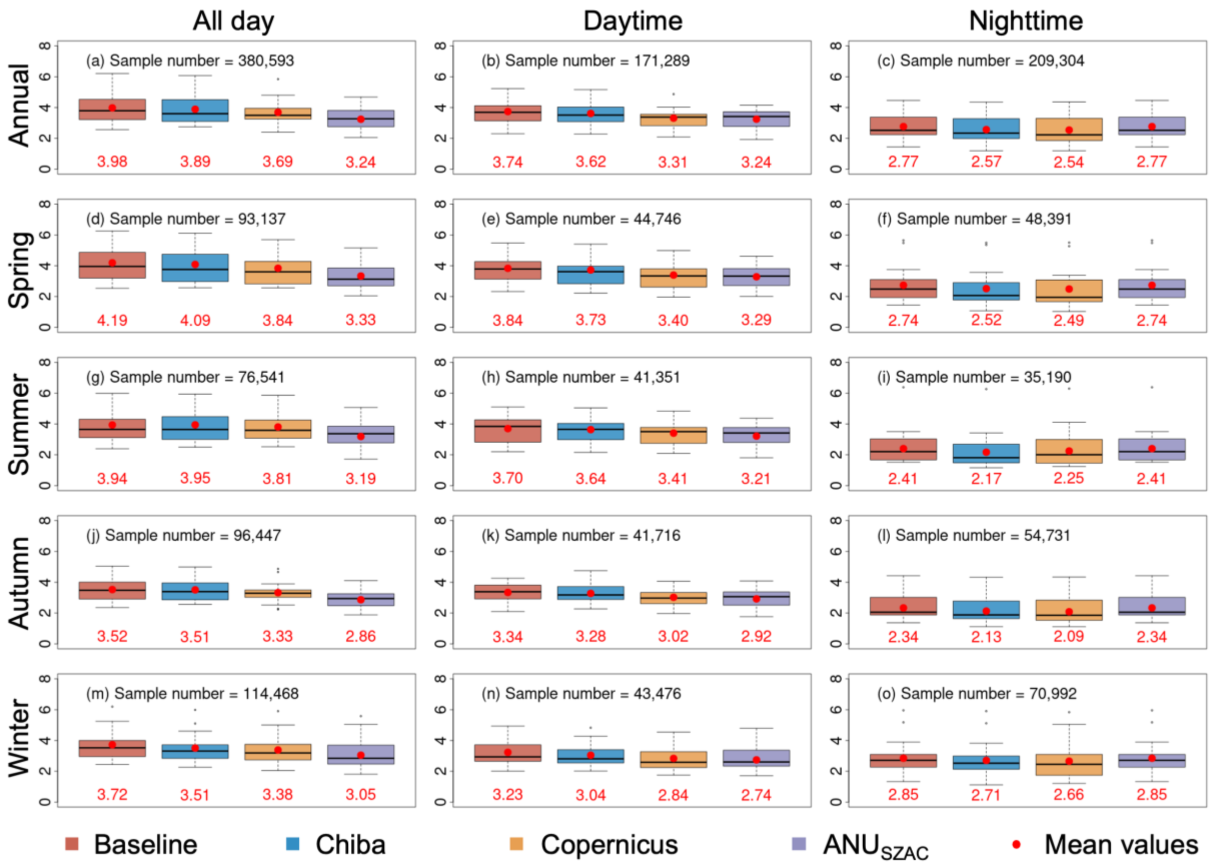

Fig. 10. Annual and seasonal boxplots of ubRMSE of baseline, Chiba, Copernicus and ANU_{SZAC} LST against in-situ LST at different times (i.e., all day, daytime and nighttime) between 01/Jan/2016 and 31/Dec/2020.

The explanation of seasonal division and boxplot features are the same as in the Fig. 9 caption. The red numbers at the bottom of each plot are the overall mean values of ubRMSE. The unit of ubRMSE is K.

Fig. 11 presents the hourly boxplots over the diurnal cycle of bias of baseline, Chiba, Copernicus and ANU_{SZAC} LST against *in-situ* LST in local standard time zone between 01/Jan/2016 and 31/Dec/2020. During the daytime, ANU_{SZAC} LST showed smaller bias values compared to baseline LST. This was evident as the bias of ANU_{SZAC} LST was closer to the zero-bias line, indicating a reduced systematic error. Additionally, the spread of boxplots representing the variation of bias at different sites was also narrowed for ANU_{SZAC} LST. The biggest improvement in bias of ANU_{SZAC} LST was observed around midday (i.e., 10:00-12:00 local standard time), corresponding to the time when the SZAC coefficients reach their maximum thus the calibration had the strongest effects (see Fig. 3 a). On the other hand, both Chiba and Copernicus LST showed better bias performance than baseline during the daytime. However, both Chiba and Copernicus LST exhibited negative bias during the nighttime, indicating an underestimation of LST values compared to *in-situ* measurements. In contrast, during the nighttime the median values of baseline and ANU_{SZAC} LST were close to the zero-bias line. Overall, the calibration process applied to ANU_{SZAC} LST effectively mitigated most systematic errors, resulting in improved accuracy during daytime hours.

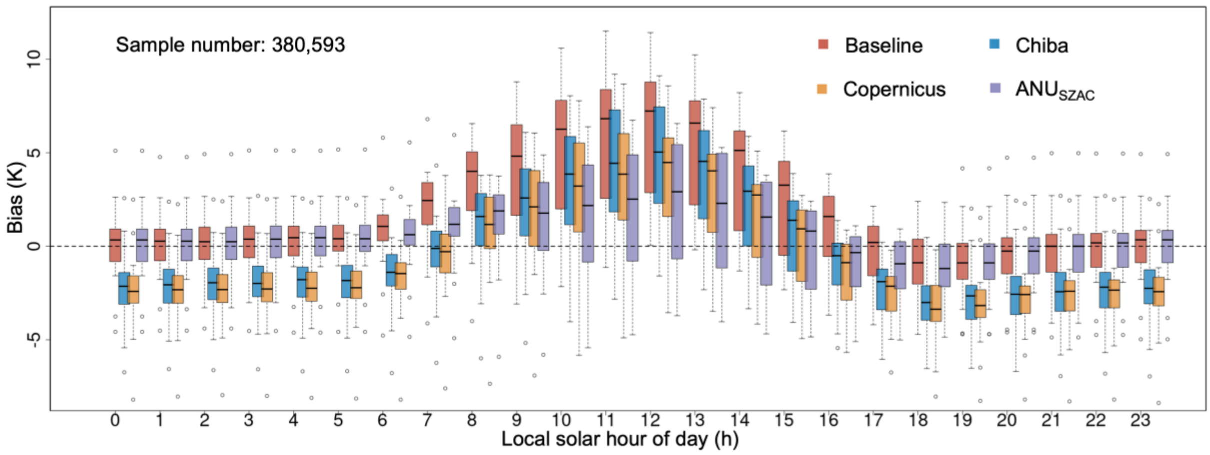

Fig. 11. Hourly boxplots over the diurnal cycle of bias of baseline, Chiba, Copernicus and ANU$_{SZAC}$ LST against in-situ LST in local standard time zone between 01/Jan/2016 and 31/Dec/2020. The boxplot features are fully explained in the Fig. 9 caption.

Fig. 12 presents four examples of temporal variation of baseline, Chiba, Copernicus, ANU$_{SZAC}$ and *in-situ* LST in local standard time zone at (a) Cumberland Plain, (b) Daly Uncleared, (c) Gingin and (d) Tumbarumba sites within a 150-hour temporal window (see Fig. 1 (b) for the locations of these OzFlux sites). All four Himawari-8 LST products showed consistent diurnal cycles with *in-situ* LST measurements. Among them, the baseline LST was generally overestimated during daytime (a-c), which has been effectively resolved in ANU$_{SZAC}$ LST. As a comparison, ANU$_{SZAC}$ LST exhibited similar temporal patterns with Chiba and Copernicus LST during daytime, aligning more closely with their diurnal cycles. However, ANU$_{SZAC}$ LST retained the nighttime component of baseline LST, which generally demonstrates better agreement with *in-situ* LST during nighttime, aligning more closely with the observed LST values in most cases.

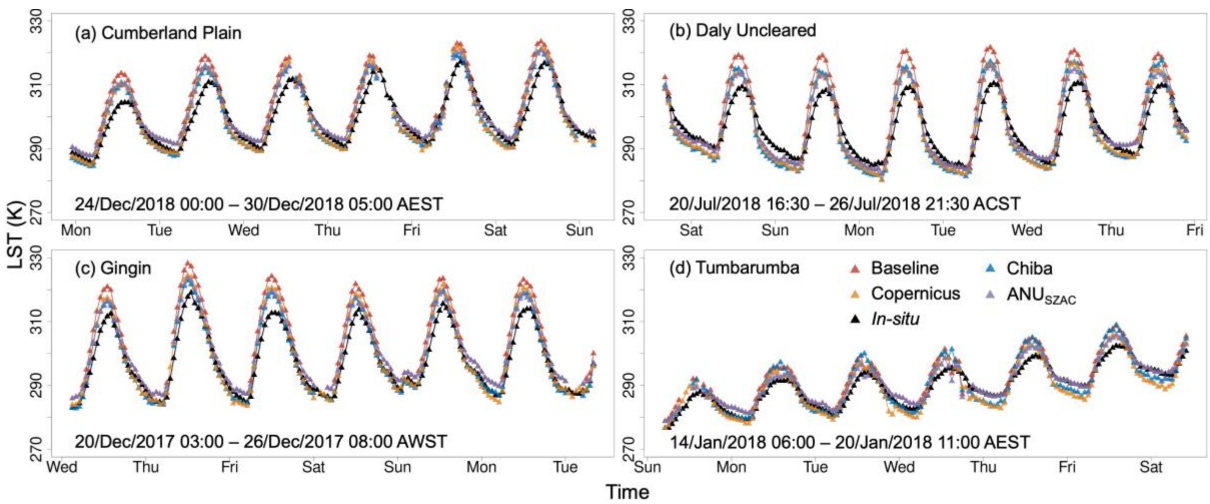

Fig. 12. Four examples of temporal variation of baseline, Chiba, Copernicus, ANU$_{SZAC}$ and in-situ LST in local standard time zone at (a) Cumberland Plain, (b) Daly Uncleared, (c) Gingin and (d) Tumbarumba OzFlux sites within a 150-hour window. The legend in (d) applies to all other parts. The locations of the four sites are shown in Fig. 1 (b) with additional site information provided in Table 3.

4.3 Spatial comparison against VIIRS LST during 2016-2020

Fig. 13 presents the spatial distribution of bias and ubRMSE of baseline, Chiba, Copernicus and ANU_{SZAC} LST against all available LST pixels from VIIRS (i.e., VNP21A1D) for the Australian continent at ~ 13:30 local solar time between 01/Jan/2016 and 31/Dec/2020. The median bias of baseline, Chiba, Copernicus and ANU_{SZAC} LST against VIIRS LST was 3.02, 1.07, 0.33 and -0.63 K, respectively. This indicates that all Himawari-8 LST products demonstrated less bias when compared against VIIRS LST than when compared against Aqua-MODIS LST (which was 4.85, 2.90, 2.28 and 0.98 K, respectively; see Fig. 8). Notably, both VIIRS and Aqua-MODIS have an overpass time of ~ 13:30 local solar time making this comparison essentially free of diurnal cycle influences. The median ubRMSE of baseline, Chiba, Copernicus and ANU_{SZAC} LST against VIIRS LST was 3.07, 2.84, 2.92 and 2.94 K, respectively. ANU_{SZAC} LST exhibited reduced values of ubRMSE in northern and mid-eastern regions of Australia compared to the baseline LST. In general, ANU_{SZAC} LST was more comparable to Copernicus LST than the two other products in terms of bias and ubRMSE metrics. However, ANU_{SZAC} offered the additional advantage of higher spatial resolution (i.e., 2 km for ANU_{SZAC} and ~ 4.5 km for Copernicus) and better temporal frequency (i.e., 10 min for ANU_{SZAC} and 1 hour for Copernicus); see Table 2.

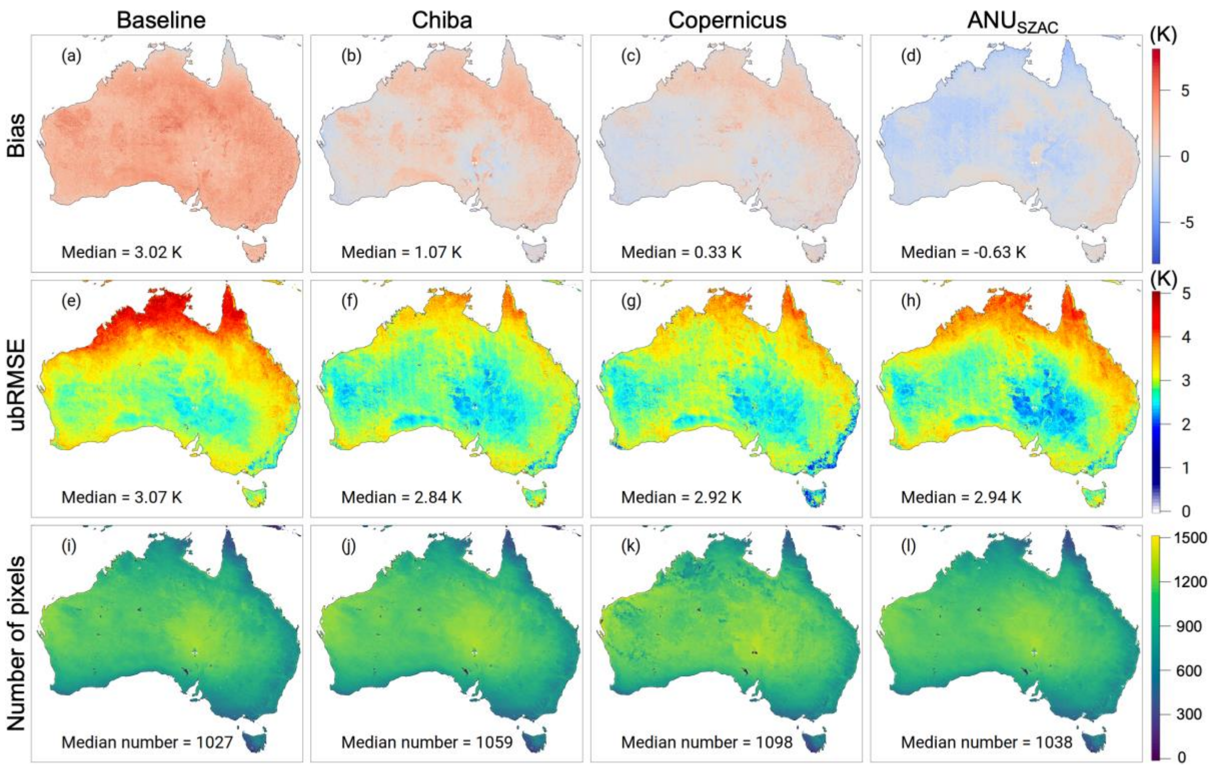

Fig. 13. Spatial distribution of bias and ubRMSE of baseline, Chiba, Copernicus and ANU$_{SZAC}$ LST against all available LST pixels from VIIRS (i.e., VNP21A1D) for Australia at ~ 13:30 local solar time between 01/Jan/2016 and 31/Dec/2020. The oceans and seas surrounding Australia are white in all parts.

Fig. 14 presents two examples of spatial pattern comparison of baseline, Chiba, Copernicus and ANU$_{SZAC}$ LST against VIIRS LST at 04:00 GMT (i.e., equivalent to 14:00 AEST, 13:30 ACST or 12:00 AWST) on 20/Jun/2019 (austral winter) and 20/Dec/2019 (austral summer), respectively. On both days, the four Himawari-8 LST products exhibit similar spatial patterns, though differences are observed. On 20/Jun/2019, the baseline LST generally showed higher values in the north-western regions; while on 20/Dec/2019, the baseline LST displayed higher values in eastern regions. In contrast, ANU$_{SZAC}$ LST demonstrated more similarity with Chiba, Copernicus on both days, showing reduced discrepancies with the reference VIIRS LST product. On 20/Jun/2019, the differences of Chiba, Copernicus and ANU$_{SZAC}$ LST against VIIRS were visually similar (Fig. 14, second column from left). On 20/Dec/2019, Chiba LST showed slightly higher values while

ANU_{SZAC} LST exhibited slightly lower values compared to VIIRS LST (Fig. 14, right most column). The spatial comparisons presented in Fig. 14 were consistent with the pixelwise metrics indicated in Fig. 13.

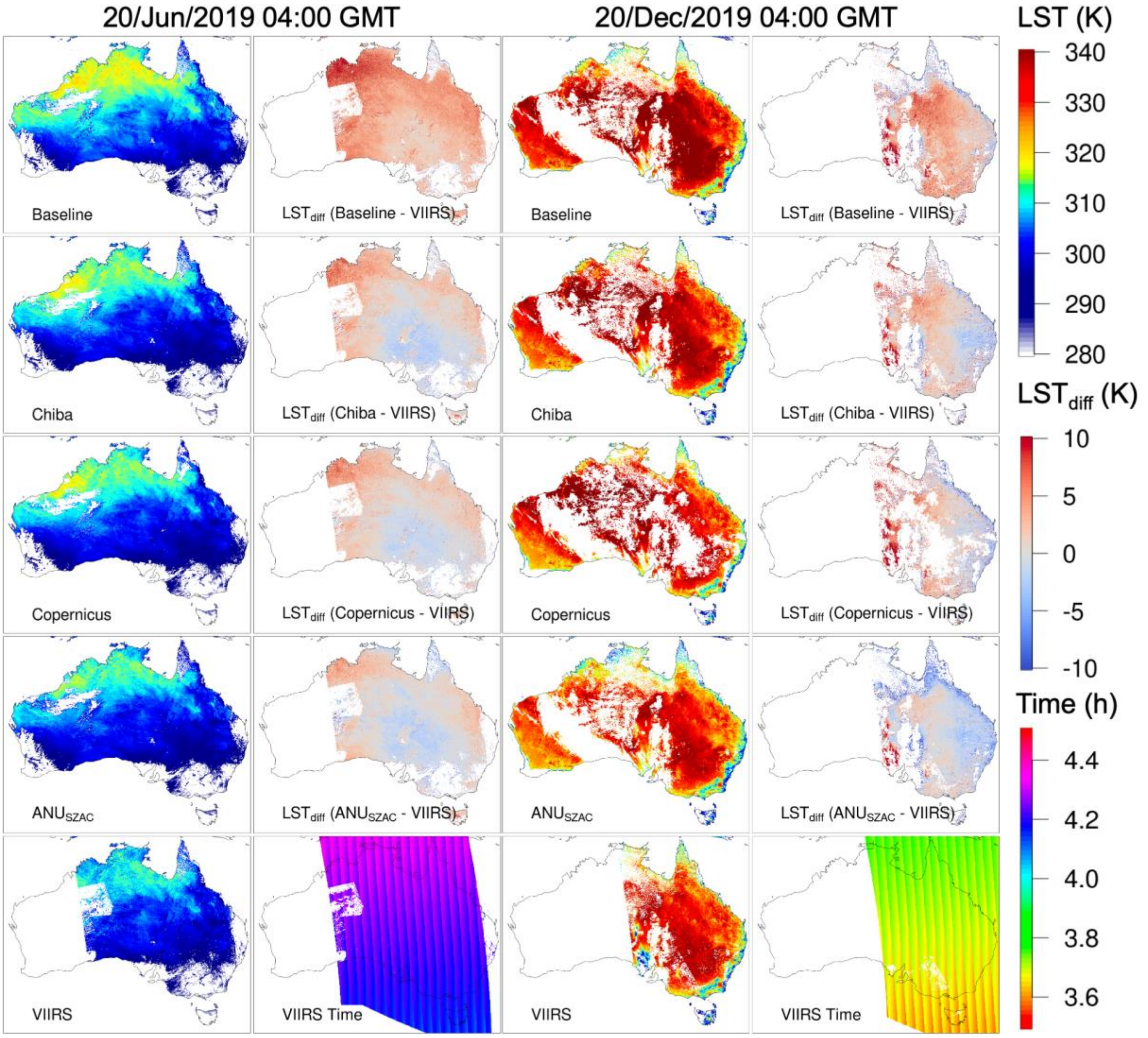

Fig. 14. Two examples of spatial comparison of baseline, Chiba, Copernicus and ANU_{SZAC} LST against VIIRS LST at 04:00 GMT on 20/Jun/2019 and 20/Dec/2019, respectively. The first and third columns from the left are LST from the four Himawari products with VIIRS being the bottom row. The first four rows of the second and fourth columns from the left are differences (denoted 'LST_{diff}' in the legend) between each Himawari-8 LST product (in turn) and the VIIRS LST. The last rows of the second and fourth columns from the left are the VIIRS view time strips (in GMT). The oceans and seas surrounding Australia, cloud contaminated pixels and areas beyond the VIIRS swath are white in all parts.

5. Discussion

5.1 Distribution of SZAC coefficient and its physical implications

Numerous studies have noted discrepancies between LST acquired at essentially the same time from both geostationary and polar-orbiting platforms (e.g., Li et al., 2020; Trigo et al., 2021; Pérez-Planells et al., 2023). Nighttime LST products exhibit good agreement across various viewing configurations, whereas daytime observations have discrepancies attributed to the influence of shadows and temperature gradients within the landscape cover (Guillevic et al., 2013). As a result, SZA in conjunction with emissivity has been extensively applied to rectify the angular effects and enhance agreement of LST products acquired from different platforms (Vinnikov et al., 2012; Ermida et al., 2017; Ermida et al., 2018). Herein, we examined the diurnal patterns of baseline LST errors and proposed the SZAC approach, which leverages the dynamics of SZA (which mainly changes as a function of latitude, time-of-day and day-of-year) to spatiotemporally correct the daytime component of baseline LST measurements. There are four insights gleaned from this research.

Firstly, the effectiveness of SZA as an input for spatial correction lies in its cosine value, which is associated with the ratio of shadowed area to the total surface area. This property makes SZA a representative measure of the solar radiance reaching the Earth's surface (Yeom et al., 2012). Vinnikov et al. (2012) also emphasised that an SZA-based kernel is closely tied to the spatial inhomogeneity in surface heating and shadowing across diverse regions of the land surface and its cover. Moreover, the variability of SZA is linked to diurnal changes, seasonal fluctuations, and latitudinal differences. Consequently, it serves as a valuable bridging parameter to quantify the systematic differences between diverse LST products, which were developed using different underlying assumptions and showed systematic differences (see Table 1).

Secondly, the SZAC coefficient revealed negative associations with vegetation cover characteristics and exhibited a greater degree of uniformity within inland regions, where calibration effects exerted a more pronounced influence. Fig. 15 shows (a-d) the continental-scale and (e-t) zoomed comparisons between the spatial patterns of SZAC coefficient and 5-year median values of MODIS EVI, LAI and albedo between 01/Jan/2016 and 31/Dec/2020 for four chosen regions, respectively. The greater uniformity observed in inland arid regions was attributed to their predominantly homogeneous and larger patches of vegetation (Fig. 15 a-d). In contrast, pixels along the eastern coastlines exhibited greater heterogeneity (Region A and C; Fig. 15 e-h and q-t), characterised by denser vegetation and relatively mountainous terrain. This coastal area, where more population reside, featured more heterogeneous landscapes. Additionally, in forests, the closed canopy leads to a more even distribution, reducing internal shadowing compared to woodland areas with lower tree density. Furthermore, the SZAC coefficient and all three MODIS indices manifested distinct boundary effects within the Nullarbor Plain area (Region B; Fig. 15 i-l), an important biogeographic region as defined by the Australian Government (DCCEEW, 2020). Finally, it is noteworthy that for the Lake Eyre area (Region C; Fig. 15 m-p), the SZAC coefficient demonstrated strong connections with the masked area of LAI, which were all salt lakes, signifying the absence of canopies. The albedo of region C was also the highest within Australia, demonstrating a distinctive characteristic of highly reflective surfaces in this area.

705

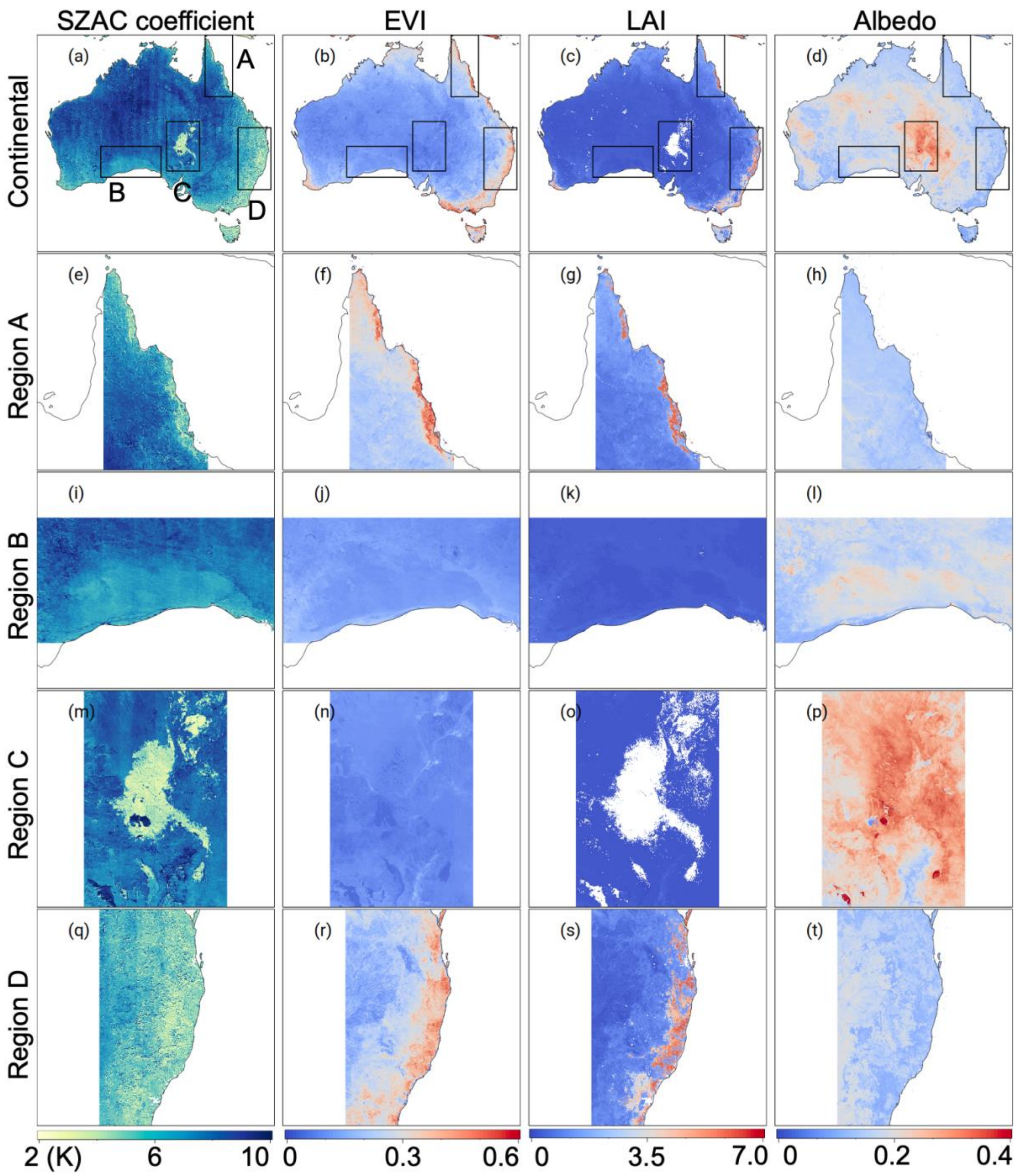

706 *Fig. 15. (a-d) Continental-scale and (e-t) zoomed comparisons between the spatial patterns of SZAC*
707 *coefficient and 5-year median values of MODIS EVI, LAI and albedo between 01/Jan/2016 and 31/Dec/2020*
708 *for region A, B, C and D, respectively. Region A spans 142-147 °E and 10-20 ° S; region B spans 123-134 °*
709 *E and 28-33 °S; region C spans 135-141 °E and 24-32 °S; and region D spans 148-154 °E and 25-35 °S.*

710

Fig. 16 presents violin plots illustrating the values of the SZAC coefficient within four equal-value-range quantiles for (a) EVI, (b) LAI, and (c) albedo between 01/Jan/2016 and 31/Dec/2020. For both EVI and LAI, the SZAC coefficient exhibited similar decreasing trend with increasing vegetation indices. As depicted in Fig. 16 (a) and (b), when EVI (LAI) was concentrated within the range of 0-0.15 (0-1.75), the median values of SZAC coefficient were 7.97 K (7.75 K); conversely, when EVI (LAI) was concentrated within the range of 0.45-0.60 (5.25-7.00), the median values of SZAC coefficient decreased to 4.87 K (4.71 K). This trend aligns with the observations in Fig. 15 (a-c), where higher SZAC coefficient values were associated with sparser vegetation (inland Australia), while lower values were linked to denser vegetation and more complex landscapes (eastern coastal Australia). Concerning albedo, the SZAC coefficient demonstrated a positive relationship when albedo was lower than 0.30. However, when albedo was concentrated within the range of 0.30-0.40, the SZAC coefficient exhibited high uncertainties, indicating a lack of strong connections between them in such scenarios. These findings reinforce the relationship between the spatial pattern of SZAC coefficient and vegetation cover characteristics.

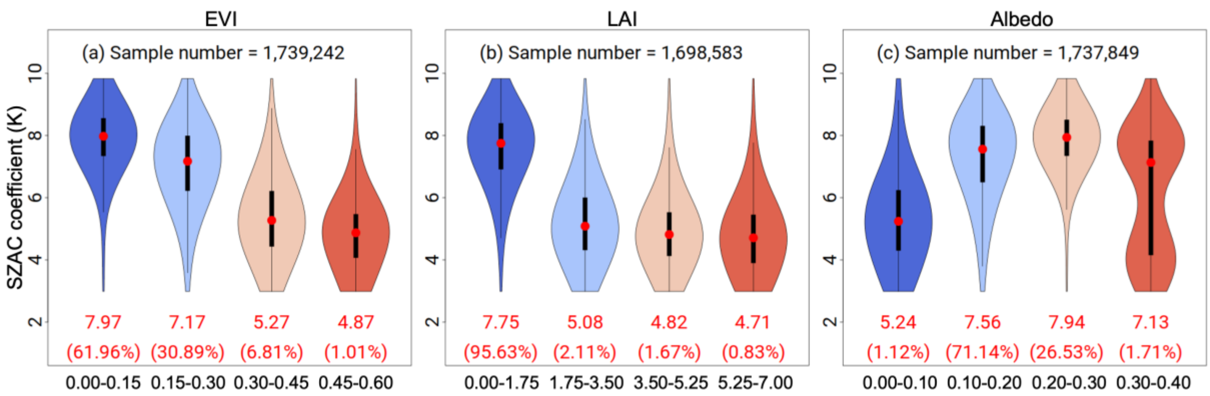

Fig. 16. Violin plots of the values of SZAC coefficient within four equal-value-range quantiles for (a) EVI; (b) LAI; and (c) albedo, respectively, between 01/Jan/2016 and 31/Dec/2020. The red dots within violins represent the median value; the bold vertical black lines within violins are the interquartile range (i.e., the 75% and 25% values, respectively); the upper and lower limits of violins represent the maximum and minimum values excluding any outliers; the distribution of violins represent the kernel density of sample

numbers within each quantile. The red decimal numbers (percentage) at the bottom of each plot are the median values (percentage of overall sample numbers) of SZAC coefficient within each quantile.

Thirdly, it is noteworthy that the distribution of the SZAC coefficient may be influenced by VZA of the employed satellites (Himawari-8, Terra and Aqua), although VZA was not explicitly incorporated into the calibration process. In Fig. 4, a discernible pattern in SZAC dependence was observed, particularly in relation to the longitudinal position of 140.7° E (i.e., the longitude of Himawari-8). It becomes evident that SZAC values are lower in southern regions near this longitude and higher in areas situated farther away, such as those in Western Australia (WA) and western South Australia (SA). This pattern could be attributed to the fixed VZA of Himawari-8, where a shorter atmospheric path (or lower VZA values) tends to enhance the accuracy of LST retrievals. Additionally, the distribution of the SZAC coefficient is also influenced by the viewing geometries of MODIS satellites (see Fig. 4), specifically the Terra descending and Aqua ascending orbits.

Fourthly and finally, in alignment with various parametric modelling approaches, such as diurnal temperature cycle (DTC) models, the SZAC coefficient holds physical interpretations and implications. Yamamoto et al. (2023) recently explored DTC models using Himawari-8 LST data as inputs, revealing that the maximum daily LST (T_{max}) and its diurnal temperature range (DTR) emerged as particularly informative parameters for monitoring vegetation drying signals under heatwave. This was attributed to heightened sensitivity of T_{max} to geometric conditions of sun-target-observer, its stability in model fitting, and its correlations with other environmental variables like vegetation indices and soil moisture. In this research, the SZAC coefficient was derived based on SZA values ranging from 20 to 70 ° and can be conceptualised as representing the 'magnitude of LST disparities between different platforms during the heating period of surface'. Fig. 3 illustrated when SZA approaches its minimum value (around midday), the magnitude of LST differences (and correction effect of SZAC) attains its maximum extent. Given that SZA represents the angle formed between the Sun's rays and the vertical direction, this phenomenon signifies a vital relationship between the extent of shadowing and the observed variations in LST. Moreover, the SZAC approach is consistent with previous studies that modelled DTC models by relying on sparse polar-orbiting LST observations (Duan et al., 2012; Hu et al., 2020a; Lu and Zhou, 2021). However, the performance of SZAC within 'twilight times' may require further re-evaluation due to limited available data during the time of day-to-night transition (and vice versa). The lack of data during day-night transitions can potentially introduce uncertainties in performance of SZAC, especially when dealing with rapid temperature changes and complex atmospheric conditions within twilight zones (Kurihara et al., 2016; Eytan et al., 2020).

5.2 Usage and prospects of SZAC

SZAC has demonstrated robustness and operational capability in reducing systematic bias when compared to MODIS, VIIRS and *in-situ* LST measurements. Additionally, the ANU_{SZAC} LST derived from the SZAC approach showed a reduction of ~ 0.5 K in ubRMSE compared to the baseline LST when evaluated against daytime *in-situ* LST (Fig. 10). When compared to MODIS-Aqua and VIIRS LST, ANU_{SZAC} LST maintained a similar level of ubRMSE with the other three Himawari-8 LST products (i.e., baseline, Chiba, Copernicus). These findings underscore SZAC's capability to reduce error deviations (as demonstrated by the ubRMSE statistics against *in-situ* LST) while aligning LST values more closely with those obtained from polar-orbiting platforms (see the bias statistics). It demonstrates consistency with LSTs from both new generation geostationary satellites, thereby offering additional choices for researchers and practitioners who rely on LST snapshots from MODIS and VIIRS. For applications needing high temporal frequency thermal observations, ANU_{SZAC} LST emerges as a valuable alternative or complement to the polar-orbiting MODIS and VIIRS.

The ANU_{SZAC} LST did exhibit a higher ubRMSE than the other three products when compared against Terra-MODIS. This heightened uncertainty may stem from variations in SZA, particularly when SZA surpasses 50 ° (see Fig. 3 a), where the Himawari-8 baseline-MODIS difference and SZA becomes more variable under these circumstances. This increased variability of baseline-MODIS difference may be attributed to the weaker incoming solar radiance during the Terra overpass time (compared to Aqua and Suomi-NPP), diminishing the relative importance of SZA. Liu et al. (2009) similarly highlighted that global solar measurements may experience degradation due to cosine errors when SZA becomes large. Moreover, higher SZA values indicate an extended solar atmospheric path length, amplifying the potential impact of minor errors in precipitable water parameterisation on both baseline LST and SZAC correction attempts. Consequently, SZAC may introduce more uncertainties and spatial variabilities during Terra overpass time. However, considering the wavelength-dependent drift in reflectance, particularly with a drop of up to 8% in the shortest wavelength region observed in Terra-MODIS NIR spectral bands (Wu et al., 2013), it becomes crucial to prioritise consistency with Aqua-MODIS and VIIRS LST, where ANU_{SZAC} has demonstrated commendable performance.

The coefficient of SZAC was optimised against best-quality LST pixels from MOD/MYD11 series, which may warrant reconsideration or improvements in the future, given the dynamic nature of remote sensing data and advancements in satellite missions. As the Terra-MODIS mission was discontinued since November 2022, this would impact the availability of MODIS data and raise questions about the long-term sustainability of using MOD/MYD11 LST for calibration and evaluation. Alternative satellite missions and/or newer generation sensors should be considered to maintain the ongoing accuracy of the SZAC algorithm. Meanwhile, studies have reported certain limitations of the MOD/MYD11 LST product, particularly its tendency to underestimate LST during daytime in certain regions (Li et al., 2014). Inconsistencies have been identified between

MOD/MYD11 and their successor VNP21, with MYD11 LST typically being 2 K cooler than VNP21 LST (Hulley et al., 2017). To address this issue, NASA produced two LST&E products (i.e., MOD/MYD21) to ensure data continuity among these platforms, with the bias of MYD21 LST against VNP21 LST narrowed to ~ 0.4 K. Though ANU_{SZAC} LST has already demonstrated acceptable consistencies with MOD/MYD11 and VNP21 LST, it is crucial to consider further comparisons of ANU_{SZAC} against MOD/MYD21. Moreover, future calibrations might simultaneously incorporate MYD21 and VNP21, necessitating ongoing evaluations. It would be beneficial to compare ANU_{SZAC} LST with other new generation LST products, e.g., the ECOsystem Spaceborne Thermal Radiometer Experiment on Space Station (ECOSTRESS) LST (Fisher et al., 2020). However, caution must be exercised when designing the experiments and comparison workflow due to the inherent spatiotemporal variability of LST. ECOSTRESS LST, with its irregular revisit frequency and 70 m spatial resolution, may not be suitable for direct comparison purposes. To address this, a matching strategy and spatial downscaling techniques (e.g., Yu et al., 2023) could be thoughtfully implemented in the comparison process to ensure meaningful and accurate assessments.

SZAC has shed light on potential LST calibration methods for the future, suggesting the need for spatially varied coefficients to better accommodate localised conditions. The SZAC coefficient is highly relevant to the diurnal pattern of LST error variations for a specific region and can be optimised for observation areas of different geostationary satellites. Using MODIS LST data covering Australia, we presented a pixelwise optimisation strategy that ensured ANU_{SZAC} LST incorporated MODIS LST spatial variability over the entire continent. However, LST also has considerable temporal variability and is highly dependent on localised conditions (Van De Kerchove et al., 2013; Sekertekin et al., 2016). Thus, this optimisation strategy could be extended temporally to derive seasonally dependent sets of coefficients, which may improve the accuracy of ANU_{SZAC} LST in capturing the seasonal variability of LST. However, strategies would need to be enlisted to ensure artificial step-changes in LST aren't introduced across the seasonal boundaries. Furthermore, implementing SZAC on LST using data acquired by other geostationary satellites, such as the GOES series in the Americas and the Meteosat series over Europe and Africa, may be a promising direction for future research. Developing a globally adaptive SZAC coefficient set could potentially improve our understanding of the error characteristics of overlapping geostationary satellites and enable the creation of a new global-coverage geostationary LST product, similar to the Copernicus LST. It will also help identify any potential regional biases and/or limitations of the current SZAC approach, allowing for targeted refinements and calibrations to improve accuracy and applicability. This could enhance our ability to monitor and study LST globally and aid in applications such as weather forecasting, climate modelling, and ecological and agricultural monitoring.

6. Conclusion

Numerous studies have reported the discrepancies between LST obtained from geostationary platforms and those from polar-orbiting missions, which can be particularly high (e.g., 12 K) during the daytime due to variations in viewing angles and shadowing effects. To overcome this challenge, SZA serves as a bridging parameter to systematically quantify differences between platforms. We proposed SZAC to operationally calibrate the daytime component of a Himawari-8 SW algorithm retrieved LST. SZAC is an empirical function based on the variations of SZA, describing the spatial heterogeneity and magnitude of LST discrepancies from different products.

We evaluated the calibrated LST product (ANU_{SZAC}) against MODIS LST and VIIRS LST, as well as *in-situ* LST measurements from the OzFlux network. We also compared ANU_{SZAC} LST with three Himawari-8 LST datasets (baseline, Chiba and Copernicus) over 01/Jan/2016 to 31/Dec/2020. The median values of bias of ANU_{SZAC} LST during daytime against Terra-MODIS LST, Aqua-MODIS LST and VIIRS LST were 1.52 K, 0.98 K and -0.63 K, respectively. In contrast, the other three Himawari-8 LST products had at least doubled bias against MODIS LST datasets. Additionally, the baseline and Chiba LST displayed higher bias than ANU_{SZAC} LST against VIIRS LST, whereas Copernicus LST showed good agreement with VIIRS LST, being a bias of 0.33 K. All four Himawari-8 LST products showed comparable ubRMSE when compared to LST from polar-orbiting platforms (i.e., MODIS and VIIRS). In the evaluation against daytime *in-situ* LST, the overall mean values of bias (ubRMSE) of baseline, Chiba, Copernicus and ANU_{SZAC} LST were 4.23 K (3.74 K), 2.16 K (3.62 K), 1.73 K (3.31 K) and 1.41 K (3.24 K), respectively. This demonstrated the lower bias of ANU_{SZAC} LST, and similar deviation of uncertainty (represented by ubRMSE), when evaluated against peer products.

Overall, SZAC demonstrated robustness and operational capability in reducing systematic bias in comparison to MODIS, VIIRS and *in-situ* LST measurements. It has shed light on potential calibration methods for the future, suggesting the need for spatially varying coefficients to better accommodate localised conditions. It is possible to extend SZAC using data acquired from other geostationary satellites, such as the GOES series in the Americas and the Meteosat series over Europe and Africa. This should improve our understanding of the error characteristics of overlapped geostationary imageries, allowing for targeted refinements and calibrations to further enhance applicability.

Acknowledgement

This research was performed as part of a PhD by the first author (YY) under an academic collaboration between the Australian National University (ANU) and the Commonwealth Scientific and Industrial Research Organisation (CSIRO). This research was undertaken while supported by the ANU University Research Scholarship and an ANU-CSIRO Digital Agriculture PhD Supplementary Scholarship through the Centre for Entrepreneurial Agri-Technology (CEAT). We thank the continued support of the TERN Landscapes Observatory (https://www.tern.org.au/tern-observatory/tern-landscapes/), a sensing platform of the Terrestrial Ecosystem Research Network (TERN; https://www.tern.org.au/), which is supported and enabled by the Australian Government through the National Collaborative Research Infrastructure Strategy (NCRIS). We acknowledge the resources and services provided by the National Computational Infrastructure (NCI), which is also supported by the Australian Government through NCRIS. This research was supported by resources and expertise provided by CSIRO IMT Scientific Computing.

Code availability

The key scripts for the development and operation of Himawari-ANU LST dataset (i.e., ANU_{SZAC}) are publicly available at https://github.com/yuyi13/Himawari-ANU, with a permalink registered at Zenodo (DOI will be provided once the manuscript is formally published).

Data availability

The Himawari-ANU LST dataset (i.e., ANU_{SZAC}) is publicly available from the TERN Data Discovery Portal (DOI) and NCI Data Catalogue (DOI will be provided once the manuscript is formally published).

References

Allen, R. G., Pereira, L. S., Raes, D. and Smith, M., 1998. *Crop evapotranspiration - Guidelines for computing crop water requirements - FAO Irrigation and drainage paper 56,* Food and Agriculture Organization of the United Nations, Rome. Available at: https://www.fao.org/3/x0490e/x0490e00.htm [Accessed 11/Sep/2023].

Atitar, M. and Sobrino, J. A., 2008. A split-window algorithm for estimating LST from Meteosat 9 data: Test and comparison with in situ data and MODIS LSTs. *IEEE Geosci. Remote Sens., 6*, 122-126. https://doi.org/10.1109/LGRS.2008.2006410.

Azarderakhsh, M., Prakash, S., Zhao, Y. and AghaKouchak, A., 2020. Satellite-Based Analysis of Extreme Land Surface Temperatures and Diurnal Variability Across the Hottest Place on Earth. *IEEE Geosci. Remote Sens., 17*, 2025-2029. https://doi.org./10.1109/LGRS.2019.2962055.

Barton, I. J., Zavody, A. M., O'Brien, D. M., Cutten, D. R., Saunders, R. W. and Llewellyn-Jones, D. T., 1989. Theoretical algorithms for satellite-derived sea surface temperatures. *J. Geophys. Res. Atmos., 94*, 3365-3375. https://doi.org/10.1029/JD094iD03p03365.

Beringer, J., Hutley, L. B., McHugh, I., Arndt, S. K., Campbell, D., Cleugh, H. A., Cleverly, J., Resco de Dios, V., Eamus, D. and Evans, B., 2016. An introduction to the Australian and New Zealand flux tower network - OzFlux. *Biogeosciences, 13*, 5895-5916. https://doi.org/10.5194/bg-13-5895-2016.

Bessho, K., Date, K., Hayashi, M., Ikeda, A., Imai, T., Inoue, H., Kumagai, Y., Miyakawa, T., Murata, H. and Ohno, T., 2016. An introduction to Himawari-8/9 - Japan's new-generation geostationary meteorological satellites. *J. Meteorol. Soc. Jpn. Ser. II, 94*, 151-183. https://doi.org/10.2151/jmsj.2016-009.

Brent, R. P., 2013. *Algorithms for Minimization Without Derivatives,* Dover Publications, Canberra. Available at: https://books.google.com.au/books?id=AITCAgAAQBAJ [Accessed 25/Aug/2023].

Bureau of Meteorology, 2021. *Bureau of Meteorology Satellite Observations (Collection)*. NCI Australia, Canberra. https://doi.org/10.25914/61A609F9E7FFA.

Cao, B., Liu, Q., Du, Y., Roujean, J.-L., Gastellu-Etchegorry, J.-P., Trigo, I. F., Zhan, W., Yu, Y., Cheng, J., Jacob, F., Lagouarde, J.-P., Bian, Z., Li, H., Hu, T. and Xiao, Q., 2019. A review of earth surface thermal radiation directionality observing and modeling: Historical development, current status and perspectives. *Remote Sens. Environ., 232*, 111304. https://doi.org/10.1016/j.rse.2019.111304.

Chu, H., Luo, X., Ouyang, Z., Chan, W. S., Dengel, S., Biraud, S. C., Torn, M. S., Metzger, S., Kumar, J. and Arain, M. A., 2021. Representativeness of Eddy-Covariance flux footprints for areas surrounding AmeriFlux sites. *Agric. For. Meteorol., 301*, 108350. https://doi.org/10.1016/j.agrformet.2021.108350.

Coll, C., Caselles, V., Sobrino, J. A. and Valor, E., 1994. On the atmospheric dependence of the split-window equation for land surface temperature. *Int. J. Remote Sens., 15*, 105-122. https://doi.org/10.1080/01431169408954054.

Cresswell, M., Morse, A., Thomson, M. and Connor, S., 1999. Estimating surface air temperatures, from Meteosat land surface temperatures, using an empirical solar zenith angle model. *Int. J. Remote Sens., 20*, 1125-1132. https://doi.org/10.1080/014311699212885.

DCCEEW, 2020. *Interim Biogeographic Regionalisation (IBRA) for Australia v. 7*. Australian Government Department of Climate Change, Energy, the Environment and Water, Canberra. Available at: https://www.dcceew.gov.au/environment/land/nrs/science/ibra [Accessed 14/Nov/2023].

Di Napoli, C., Barnard, C., Prudhomme, C., Cloke, H. L. and Pappenberger, F., 2021. ERA5-HEAT: A global gridded historical dataset of human thermal comfort indices from climate reanalysis. *Geosci. Data J., 8*, 2-10. https://doi.org/10.1002/gdj3.102.

Di Napoli, C., Pappenberger, F. and Cloke, H. L., 2019. Verification of Heat Stress Thresholds for a Health-Based Heat-Wave Definition. *J. Appl. Meteorol. Climatol., 58*, 1177-1194. https://doi.org/10.1175/JAMC-D-18-0246.1.

Duan, S.-B., Li, Z.-L., Tang, B.-H., Wu, H. and Tang, R., 2014. Generation of a time-consistent land surface temperature product from MODIS data. *Remote Sens. Environ., 140*, 339-349. https://doi.org/10.1016/j.rse.2013.09.003.

Duan, S.-B., Li, Z.-L., Wang, N., Wu, H. and Tang, B.-H., 2012. Evaluation of six land-surface diurnal temperature cycle models using clear-sky in situ and satellite data. *Remote Sens. Environ., 124*, 15-25. https://doi.org/10.1016/j.rse.2012.04.016.

Ekinzog, E. K., Schlerf, M., Kraft, M., Werner, F., Riedel, A., Rock, G. and Mallick, K., 2022. Revisiting crop water stress index based on potato field experiments in Northern Germany. *Agric. Water Manag., 269*, 107664. https://doi.org/10.1016/j.agwat.2022.107664.

Ermida, S. L., DaCamara, C. C., Trigo, I. F., Pires, A. C., Ghent, D. and Remedios, J., 2017. Modelling directional effects on remotely sensed land surface temperature. *Remote Sens. Environ., 190*, 56-69. https://doi.org/10.1016/j.rse.2016.12.008.

Ermida, S. L., Trigo, I. F., DaCamara, C. C. and Roujean, J.-L., 2018. Assessing the potential of parametric models to correct directional effects on local to global remotely sensed LST. *Remote Sens. Environ., 209*, 410-422. https://doi.org/10.1016/j.rse.2018.02.066.

Eytan, E., Koren, I., Altaratz, O., Kostinski, A. B. and Ronen, A., 2020. Longwave radiative effect of the cloud twilight zone. *Nat. Geosci., 13*, 669-673. https://doi.org/10.1038/s41561-020-0636-8.

Fisher, J. B., Lee, B., Purdy, A. J., Halverson, G. H., Dohlen, M. B., Cawse-Nicholson, K., Wang, A., Anderson, R. G., Aragon, B. and Arain, M. A., 2020. ECOSTRESS: NASA's next generation mission to measure evapotranspiration from the international space station. *Water Resour. Res., 56*, e2019WR026058. https://doi.org/10.1029/2019WR026058.

Freitas, S. C., Trigo, I. F., Macedo, J., Barroso, C., Silva, R. and Perdigão, R., 2013. Land surface temperature from multiple geostationary satellites. *Int. J. Remote Sens., 34*, 3051-3068. https://doi.org/10.1080/01431161.2012.716925.

Gillespie, A., Rokugawa, S., Matsunaga, T., Cothern, J. S., Hook, S. and Kahle, A. B., 1998. A temperature and emissivity separation algorithm for Advanced Spaceborne Thermal Emission and Reflection Radiometer (ASTER) images. *IEEE Trans. Geosci. Remote Sens., 36*, 1113-1126. https://doi.org/10.1109/36.700995.

Guillevic, P. C., Bork-Unkelbach, A., Göttsche, F. M., Hulley, G., Gastellu-Etchegorry, J. P., Olesen, F. S. and Privette, J. L., 2013. Directional Viewing Effects on Satellite Land Surface Temperature Products Over Sparse Vegetation Canopies—A Multisensor Analysis. *IEEE Geosci. Remote Sens., 10*, 1464-1468. https://doi.org/10.1109/LGRS.2013.2260319.

Hersbach, H., Bell, B., Berrisford, P., Hirahara, S., Horányi, A., Muñoz-Sabater, J., Nicolas, J., Peubey, C., Radu, R., Schepers, D., Simmons, A., Soci, C., Abdalla, S., Abellan, X., Balsamo, G., Bechtold, P., Biavati, G., Bidlot, J., Bonavita, M., De Chiara, G., Dahlgren, P., Dee, D., Diamantakis, M., Dragani, R., Flemming, J., Forbes, R., Fuentes, M., Geer, A., Haimberger, L., Healy, S., Hogan, R. J., Hólm, E., Janisková, M., Keeley, S., Laloyaux, P., Lopez, P., Lupu, C., Radnoti, G., de Rosnay, P., Rozum, I., Vamborg, F., Villaume, S. and Thépaut, J.-N., 2020. The ERA5 global reanalysis. *Q. J. R. Meteorol. Soc., 146*, 1999-2049. https://doi.org/10.1002/qj.3803.

Holmes, T. R. H., Crow, W. T., Hain, C., Anderson, M. C. and Kustas, W. P., 2015. Diurnal temperature cycle as observed by thermal infrared and microwave radiometers. *Remote Sens. Environ., 158*, 110-125. https://doi.org/10.1016/j.rse.2014.10.031.

Hook, S. J., Gabell, A. R., Green, A. A. and Kealy, P. S., 1992. A comparison of techniques for extracting emissivity information from thermal infrared data for geologic studies. *Remote Sens. Environ., 42*, 123-135. https://doi.org/10.1016/0034-4257(92)90096-3.

Hu, L., Brunsell, N. A., Monaghan, A. J., Barlage, M. and Wilhelmi, O. V., 2014. How can we use MODIS land surface temperature to validate long-term urban model simulations? *J. Geophys. Res. Atmos., 119*, 3185-3201. https://doi.org/10.1002/2013JD021101.

Hu, L., Monaghan, A., Voogt, J. A. and Barlage, M., 2016. A first satellite-based observational assessment of urban thermal anisotropy. *Remote Sens. Environ., 181*, 111-121. https://doi.org/10.1016/j.rse.2016.03.043.

Hu, L., Sun, Y., Collins, G. and Fu, P., 2020a. Improved estimates of monthly land surface temperature from MODIS using a diurnal temperature cycle (DTC) model. *ISPRS J. Photogramm. Remote Sens., 168*, 131-140. https://doi.org/10.1016/j.isprsjprs.2020.08.007.

Hu, T., Renzullo, L. J., van Dijk, A. I. J. M., He, J., Tian, S., Xu, Z., Zhou, J., Liu, T. and Liu, Q., 2020b. Monitoring agricultural drought in Australia using MTSAT-2 land surface temperature retrievals. *Remote Sens. Environ., 236*, 111419. https://doi.org/10.1016/j.rse.2019.111419.

Huete, A., Didan, K., Miura, T., Rodriguez, E. P., Gao, X. and Ferreira, L. G., 2002. Overview of the radiometric and biophysical performance of the MODIS vegetation indices. *Remote Sens. Environ., 83*, 195-213. https://doi.org/10.1016/S0034-4257(02)00096-2.

Hulley, G. C., Malakar, N. K., Islam, T. and Freepartner, R. J., 2017. NASA's MODIS and VIIRS land surface temperature and emissivity products: A long-term and consistent earth system data record. *IEEE J. Sel. Top. Appl. Earth Obs. Remote Sens., 11*, 522-535. https://doi.org/10.1109/JSTARS.2017.2779330.

Islam, T., Hulley, G. C., Malakar, N. K., Radocinski, R. G., Guillevic, P. C. and Hook, S. J., 2016. A physics-based algorithm for the simultaneous retrieval of land surface temperature and emissivity from VIIRS thermal infrared data. *IEEE Trans. Geosci. Remote Sens., 55*, 563-576. https://doi.org/10.1109/TGRS.2016.2611566.

Jiang, L., Zhan, W., Hu, L., Huang, F., Hong, F., Liu, Z., Lai, J. and Wang, C., 2021. Assessment of different kernel-driven models for daytime urban thermal radiation directionality simulation. *Remote Sens. Environ., 263*, 112562. https://doi.org/10.1016/j.rse.2021.112562.

Jiménez-Muñoz, J. C., Sobrino, J. A., Mattar, C. and Malhi, Y., 2013. Spatial and temporal patterns of the recent warming of the Amazon forest. *J. Geophys. Res. Atmos., 118*, 5204-5215. https://doi.org/10.1002/jgrd.50456.

Justice, C. O., Vermote, E., Townshend, J. R. G., Defries, R., Roy, D. P., Hall, D. K., Salomonson, V. V., Privette, J. L., Riggs, G., Strahler, A., Lucht, W., Myneni, R. B., Knyazikhin, Y., Running, S. W., Nemani, R. R., Zhengming, W., Huete, A. R., Leeuwen, W. v., Wolfe, R. E., Giglio, L., Muller, J., Lewis, P. and Barnsley, M. J., 1998. The Moderate Resolution Imaging Spectroradiometer (MODIS): land remote sensing for global change research. *IEEE Trans. Geosci. Remote Sens., 36*, 1228-1249. https://doi.org/10.1109/36.701075.

Kerr, Y. H., Lagouarde, J. P. and Imbernon, J., 1992. Accurate land surface temperature retrieval from AVHRR data with use of an improved split window algorithm. *Remote Sens. Environ., 41*, 197-209. https://doi.org/10.1016/0034-4257(92)90078-X.

Kurihara, Y., Murakami, H. and Kachi, M., 2016. Sea surface temperature from the new Japanese geostationary meteorological Himawari-8 satellite. *Geophys. Res. Lett., 43*, 1234-1240. https://doi.org/10.1002/2015GL067159.

Li, H., Sun, D., Yu, Y., Wang, H., Liu, Y., Liu, Q., Du, Y., Wang, H. and Cao, B., 2014. Evaluation of the VIIRS and MODIS LST products in an arid area of Northwest China. *Remote Sens. Environ., 142*, 111-121. https://doi.org/10.1016/j.rse.2013.11.014.

Li, K., Guan, K., Jiang, C., Wang, S., Peng, B. and Cai, Y., 2021. Evaluation of four new Land Surface Temperature (LST) products in the US corn belt: ECOSTRESS, GOES-R, Landsat, and Sentinel-3. *IEEE J. Sel. Top. Appl. Earth Obs. Remote Sens., 14*, 9931-9945. https://doi.org/10.1109/JSTARS.2021.3114613.

Li, R., Li, H., Sun, L., Yang, Y., Hu, T., Bian, Z., Cao, B., Du, Y. and Liu, Q., 2020. An operational split-window algorithm for retrieving land surface temperature from geostationary satellite data: A case study on Himawari-8 AHI data. *Remote Sens., 12*, 2613. https://doi.org/10.3390/rs12162613.

Li, Z.-L., Tang, B.-H., Wu, H., Ren, H., Yan, G., Wan, Z., Trigo, I. F. and Sobrino, J. A., 2013. Satellite-derived land surface temperature: Current status and perspectives. *Remote Sens. Environ., 131*, 14-37. https://doi.org/10.1016/j.rse.2012.12.008.

Liu, J., Schaaf, C., Strahler, A., Jiao, Z., Shuai, Y., Zhang, Q., Roman, M., Augustine, J. A. and Dutton, E. G., 2009. Validation of Moderate Resolution Imaging Spectroradiometer (MODIS) albedo retrieval algorithm: Dependence of albedo on solar zenith angle. *J. Geophys. Res. Atmos., 114*. https://doi.org/10.1029/2008JD009969.

Lu, L. and Zhou, X., 2021. A Four-Parameter Model for Estimating Diurnal Temperature Cycle From MODIS Land Surface Temperature Product. *J. Geophys. Res. Atmos., 126*, e2020JD033855. https://doi.org/10.1029/2020JD033855.

Lymburner, L., Tan, P., McIntyre, A., Thankappan, M. and Sixsmith, J., 2015. *Dynamic land cover dataset version 2.1 [Dataset]*. Geoscience Australia, Canberra. Available at: http://pid.geoscience.gov.au/dataset/ga/83868 [Accessed 20/Mar/2023].

Myneni, R. B., Hoffman, S., Knyazikhin, Y., Privette, J. L., Glassy, J., Tian, Y., Wang, Y., Song, X., Zhang, Y., Smith, G. R., Lotsch, A., Friedl, M., Morisette, J. T., Votava, P., Nemani, R. R. and Running, S. W., 2002. Global products of vegetation leaf area and fraction absorbed PAR from year one of MODIS data. *Remote Sens. Environ., 83*, 214-231. https://doi.org/10.1016/S0034-4257(02)00074-3.

Niclòs, R., Caselles, V., Coll, C. and Valor, E., 2007. Determination of sea surface temperature at large observation angles using an angular and emissivity-dependent split-window equation. *Remote Sens. Environ., 111*, 107-121. https://doi.org/10.1016/j.rse.2007.03.014.

Pérez-Planells, L., Ghent, D., Ermida, S., Martin, M. and Göttsche, F.-M., 2023. Retrieval Consistency between LST CCI Satellite Data Products over Europe and Africa. *Remote Sens., 15*, 3281. https://doi.org/10.3390/rs15133281.

Price, J. C., 1984. Land surface temperature measurements from the split window channels of the NOAA 7 Advanced Very High Resolution Radiometer. *J. Geophys. Res. Atmos., 89*, 7231-7237. https://doi.org/10.1029/JD089iD05p07231.

Qin, Y., McVicar, T. R., Huang, J., West, S. and Steven, A. D. L., 2022. On the validity of using ground-based observations to validate geostationary-satellite-derived direct and diffuse surface solar irradiance: Quantifying the spatial mismatch and temporal averaging issues. *Remote Sens. Environ., 280*, 113179. https://doi.org/10.1016/j.rse.2022.113179.

Schaaf, C. B., Gao, F., Strahler, A. H., Lucht, W., Li, X., Tsang, T., Strugnell, N. C., Zhang, X., Jin, Y., Muller, J.-P., Lewis, P., Barnsley, M., Hobson, P., Disney, M., Roberts, G., Dunderdale, M., Doll, C., d'Entremont, R. P., Hu, B., Liang, S., Privette, J. L. and Roy, D., 2002. First operational BRDF, albedo nadir reflectance products from MODIS. *Remote Sens. Environ., 83*, 135-148. https://doi.org/10.1016/S0034-4257(02)00091-3.

Schmetz, J., Pili, P., Tjemkes, S., Just, D., Kerkmann, J., Rota, S. and Ratier, A., 2002. An introduction to Meteosat second generation (MSG). *Bull. Am. Meteorol. Soc., 83*, 977-992. https://doi.org/10.1175/1520-0477(2002)083%3C0977:AITMSG%3E2.3.CO;2.

Schmit, T. J., Gunshor, M. M., Menzel, W. P., Gurka, J. J., Li, J. and Bachmeier, A. S., 2005. Introducing the next-generation Advanced Baseline Imager on GOES-R. *Bull. Am. Meteorol. Soc., 86*, 1079-1096. https://doi.org/10.1175/BAMS-86-8-1079.

Schmit, T. J., Li, J., Li, J., Feltz, W. F., Gurka, J. J., Goldberg, M. D. and Schrab, K. J., 2008. The GOES-R Advanced Baseline Imager and the continuation of current sounder products. *J. Appl. Meteorol. Climatol., 47*, 2696-2711. https://doi.org/10.1175/2008JAMC1858.1.

Seemann, S. W., Borbas, E. E., Knuteson, R. O., Stephenson, G. R. and Huang, H.-L., 2008. Development of a global infrared land surface emissivity database for application to clear sky sounding retrievals from multispectral satellite radiance measurements. *J. Appl. Meteorol. Climatol., 47*, 108-123. https://doi.org/10.1175/2007JAMC1590.1.

Sekertekin, A., Kutoglu, S. H. and Kaya, S., 2016. Evaluation of spatio-temporal variability in Land Surface Temperature: A case study of Zonguldak, Turkey. *Environ. Monit. Assess., 188*, 1-15. https://doi.org/10.1007/s10661-015-5032-2.

Semmens, K. A., Anderson, M. C., Kustas, W. P., Gao, F., Alfieri, J. G., McKee, L., Prueger, J. H., Hain, C. R., Cammalleri, C. and Yang, Y., 2016. Monitoring daily evapotranspiration over two California vineyards using Landsat 8 in a multi-sensor data fusion approach. *Remote Sens. Environ., 185*, 155-170. https://doi.org/10.1016/j.rse.2015.10.025.

Sharifnezhadazizi, Z., Norouzi, H., Prakash, S., Beale, C. and Khanbilvardi, R., 2019. A Global Analysis of Land Surface Temperature Diurnal Cycle Using MODIS Observations. *J. Appl. Meteorol. Climatol., 58*, 1279-1291. https://doi.org/10.1175/JAMC-D-18-0256.1.

Singh, R., Singh, C., Ojha, S. P., Kumar, A. S., Kishtawal, C. M. and Kumar, A. S. K., 2016. Land surface temperature from INSAT-3D imager data: Retrieval and assimilation in NWP model. *J. Geophys. Res. Atmos., 121*, 6909-6926. https://doi.org/10.1002/2016JD024752.

Sobrino, J. A. and Jiménez-Muñoz, J. C., 2005. Land surface temperature retrieval from thermal infrared data: An assessment in the context of the Surface Processes and Ecosystem Changes Through Response Analysis (SPECTRA) mission. *J. Geophys. Res. Atmos., 110*. https://doi.org/10.1029/2004JD005588.

Sobrino, J. A., Jiménez-Muñoz, J. C. and Paolini, L., 2004. Land surface temperature retrieval from LANDSAT TM 5. *Remote Sens. Environ., 90*, 434-440. https://doi.org/10.1016/j.rse.2004.02.003.

Trebs, I., Mallick, K., Bhattarai, N., Sulis, M., Cleverly, J., Woodgate, W., Silberstein, R., Hinko-Najera, N., Beringer, J., Meyer, W. S., Su, Z. and Boulet, G., 2021. The role of aerodynamic resistance in thermal remote sensing-based evapotranspiration models. *Remote Sens. Environ., 264*, 112602. https://doi.org/10.1016/j.rse.2021.112602.

Trigo, I. F., Ermida, S. L., Martins, J. P., Gouveia, C. M., Göttsche, F.-M. and Freitas, S. C., 2021. Validation and consistency assessment of land surface temperature from geostationary and polar orbit platforms: SEVIRI/MSG and AVHRR/Metop. *ISPRS J. Photogramm. Remote Sens., 175*, 282-297. https://doi.org/10.1016/j.isprsjprs.2021.03.013.

Uspenskii, A. B., Kukharskii, A. V. and Uspenskii, S. A., 2015. Validation of the results of the satellite monitoring of land surface temperature. *Russ. Meteorol. Hydrol., 40*, 131-140. https://doi.org/10.3103/S1068373915020107.

Van De Kerchove, R., Lhermitte, S., Veraverbeke, S. and Goossens, R., 2013. Spatio-temporal variability in remotely sensed land surface temperature, and its relationship with physiographic variables in the Russian Altay Mountains. *Int. J. Appl. Earth Obs. Geoinf., 20*, 4-19. https://doi.org/10.1016/j.jag.2011.09.007.

Vanos, J. K., Rykaczewski, K., Middel, A., Vecellio, D. J., Brown, R. D. and Gillespie, T. J., 2021. Improved methods for estimating mean radiant temperature in hot and sunny outdoor settings. *Int. J. Biometeorol., 65*, 967-983. https://doi.org/10.1007/s00484-021-02131-y.

Vinnikov, K. Y., Yu, Y., Goldberg, M. D., Tarpley, D., Romanov, P., Laszlo, I. and Chen, M., 2012. Angular anisotropy of satellite observations of land surface temperature. *Geophys. Res. Lett., 39*. https://doi.org/10.1029/2012GL054059.

Vinnikov, K. Y., Yu, Y., Rama Varma Raja, M. K., Tarpley, D. and Goldberg, M. D., 2008. Diurnal-seasonal and weather-related variations of land surface temperature observed from geostationary satellites. *Geophys. Res. Lett., 35*. https://doi.org/10.1029/2008GL035759.

Wan, Z., 2013. *Collection-6 MODIS Land Surface Temperature Products Users' Guide*. NASA LP DAAC. Available at: https://lpdaac.usgs.gov/documents/118/MOD11_User_Guide_V6.pdf [Accessed 08/Oct/2023].

Wan, Z., 2014. New refinements and validation of the collection-6 MODIS land-surface temperature/emissivity product. *Remote Sens. Environ., 140*, 36-45. https://doi.org/10.1016/j.rse.2013.08.027.

Wan, Z. and Dozier, J., 1996. A generalized split-window algorithm for retrieving land-surface temperature from space. *IEEE Trans. Geosci. Remote Sens., 34*, 892-905. https://doi.org/10.1109/36.508406.

Wan, Z. and Li, Z.-L., 1997. A physics-based algorithm for retrieving land-surface emissivity and temperature from EOS/MODIS data. *IEEE Trans. Geosci. Remote Sens., 35*, 980-996. https://doi.org/10.1109/36.602541.

Wang, J., Tang, R., Jiang, Y., Liu, M. and Li, Z.-L., 2023. A practical method for angular normalization of global MODIS land surface temperature over vegetated surfaces. *ISPRS J. Photogramm. Remote Sens., 199*, 289-304. https://doi.org/10.1016/j.isprsjprs.2023.04.015.

Wang, K. and Liang, S., 2009. Evaluation of ASTER and MODIS land surface temperature and emissivity products using long-term surface longwave radiation observations at SURFRAD sites. *Remote Sens. Environ., 113*, 1556-1565. https://doi.org/10.1016/j.rse.2009.03.009.

Wilson, A. M. and Jetz, W., 2016. Remotely Sensed High-Resolution Global Cloud Dynamics for Predicting Ecosystem and Biodiversity Distributions. *PLOS Biol., 14*, e1002415. https://doi.org/10.1371/journal.pbio.1002415.

Wu, A., Xiong, X., Doelling, D. R., Morstad, D., Angal, A. and Bhatt, R., 2013. Characterization of Terra and Aqua MODIS VIS, NIR, and SWIR Spectral Bands' Calibration Stability. *IEEE Trans. Geosci. Remote Sens., 51*, 4330-4338. https://doi.org/10.1109/TGRS.2012.2226588.

Yamamoto, Y., Ichii, K., Ryu, Y., Kang, M. and Murayama, S., 2022. Uncertainty quantification in land surface temperature retrieved from Himawari-8/AHI data by operational algorithms. *ISPRS J. Photogramm. Remote Sens., 191*, 171-187. https://doi.org/10.1016/j.isprsjprs.2022.07.008.

Yamamoto, Y., Ichii, K., Ryu, Y., Kang, M., Murayama, S., Kim, S.-J. and Cleverly, J. R., 2023. Detection of vegetation drying signals using diurnal variation of land surface temperature: Application to the 2018 East Asia heatwave. *Remote Sens. Environ., 291*, 113572. https://doi.org/10.1016/j.rse.2023.113572.

Yamamoto, Y. and Ishikawa, H., 2018. Thermal land surface emissivity for retrieving land surface temperature from Himawari-8. *J. Meteorol. Soc. Jpn. Ser. II, 96B*, 43-58. https://doi.org/10.2151/jmsj.2018-004.

Yamamoto, Y., Ishikawa, H., Oku, Y. and Hu, Z., 2018. An Algorithm for Land Surface Temperature Retrieval Using Three Thermal Infrared Bands of Himawari-8. *J. Meteorol. Soc. Jpn. Ser. II, 96B*, 59-76. https://doi.org/10.2151/jmsj.2018-005.

Yang, J., Zhang, Z., Wei, C., Lu, F. and Guo, Q., 2017. Introducing the new generation of Chinese geostationary weather satellites, Fengyun-4. *Bull. Am. Meteorol. Soc., 98*, 1637-1658. https://doi.org/10.1175/BAMS-D-16-0065.1.

Yeom, J.-M., Han, K.-S. and Kim, J.-J., 2012. Evaluation on penetration rate of cloud for incoming solar radiation using geostationary satellite data. *Asia-Pac. J. Atmospheric Sci., 48*, 115-123. https://doi.org/10.1007/s13143-012-0011-9.

Yu, Y., Privette, J. L. and Pinheiro, A. C., 2007. Evaluation of split-window land surface temperature algorithms for generating climate data records. *IEEE Trans. Geosci. Remote Sens., 46*, 179-192. https://doi.org/10.1109/TGRS.2007.909097.

Yu, Y., Renzullo, L. J., McVicar, T. R., Malone, B. P. and Tian, S., 2023. Generating daily 100 m resolution land surface temperature estimates continentally using an unbiased spatiotemporal fusion approach. *Remote Sens. Environ., 297*, 113784. https://doi.org/10.1016/j.rse.2023.113784.

Yu, Y., Tarpley, D., Privette, J. L., Flynn, L. E., Xu, H., Chen, M., Vinnikov, K. Y., Sun, D. and Tian, Y., 2012. Validation of GOES-R Satellite Land Surface Temperature Algorithm Using SURFRAD Ground Measurements and Statistical Estimates of Error Properties. *IEEE Trans. Geosci. Remote Sens., 50*, 704-713. https://doi.org/10.1109/TGRS.2011.2162338.

Yu, Y., Tarpley, D., Privette, J. L., Goldberg, M. D., Raja, M. K. R. V., Vinnikov, K. Y. and Xu, H., 2009. Developing Algorithm for Operational GOES-R Land Surface Temperature Product. *IEEE Trans. Geosci. Remote Sens., 47*, 936-951. https://doi.org/10.1109/TGRS.2008.2006180.

Zhang, L., Jiao, W., Zhang, H., Huang, C. and Tong, Q., 2017. Studying drought phenomena in the Continental United States in 2011 and 2012 using various drought indices. *Remote Sens. Environ., 190*, 96-106. https://doi.org/10.1016/j.rse.2016.12.010.

Zhao, W., Wu, H., Yin, G. and Duan, S.-B., 2019. Normalization of the temporal effect on the MODIS land surface temperature product using random forest regression. *ISPRS J. Photogramm. Remote Sens., 152*, 109-118. https://doi.org/10.1016/j.isprsjprs.2019.04.008.